UNIVERSITY OF CALIFORNIA
RIVERSIDE

New Strategies for Molecular Organization for Functional Materials

A Dissertation submitted in partial satisfaction
of the requirements for the degree of

Doctor of Philosophy

in

Chemistry

by

Taylor Nicole Lewis

December 2022

Dissertation Committee:
Dr. Christopher Bardeen, Chairperson
Dr. James Davies
Dr. Pingyun Feng

The Dissertation of Taylor Nicole Lewis is approved:

_____

_____

_____

Chairperson

University of California, Riverside

ACKNOWLEDGEMENTS

First, I would like to acknowledge my research advisor, Chris Bardeen, who has provided guidance and insight on my research throughout my journey and taught me how to think physically about every piece of data I have acquired.

Next, I would like to acknowledge my collaborators who contributed to this dissertation work. First, the Hemmerling group at UCR, who did the laser ablation experiments and time-dependent absorption measurements in chapter 3. Second, the Krische group, who synthesized the monomer and cage compounds in chapter 4. And third, the Casanova group, who did the theoretical calculations in chapter 4.

I would also like to acknowledge my parents, Greg and Cheryl, who have continuously supported me in my life journey and have been my biggest fans. Without them, I would not be living out my dream.

And lastly, I would like to thank my boyfriend, Jimbo. First for his continuous personal and academic support, which has encouraged me to stand up for myself and my research. And second, his ability to keep me calm and confident throughout the most stressful part of my PhD.

Portions of this dissertation are adapted with permission from the following references:

Chapter 2 and Chapter 3:
Optimizing pulsed-laser ablation production of AlCl molecules for laser cooling, **Taylor N. Lewis**, Chen Wang, John R. Daniel, Madhav Dhital, Christopher J. Bardeen and Boerge Hemmerling, *Phys. Chem. Chem. Phys.*, 23, 22785-22793, (2021). DOI: 10.1039/d1cp03515k.

Chapter 2 and Chapter 4:
Chemical Tuning of Exciton versus Charge-Transfer Excited States in Conformationally Restricted Arylene Cages, **Taylor N. Lewis**, Claire Tonnelé, William G. Shuler, Zachary A. Kasun, Hiroki Sato, Adam J. Berges, Jacob R. Rodriguez, Michael J. Krische, David Casanova, Christopher J. Bardeen, *J. Am. Chem. Soc.*, 143(44), 18548-18558, (2021). DOI: 10.1021/jacs.1c08176.

ABSTRACT OF THE DISSERTATION

New Strategies for Molecular Organization for Functional Materials

by

Taylor Nicole Lewis

Doctor of Philosophy, Graduate Program in Chemistry
University of California, Riverside, December 2022
Dr. Christopher Bardeen, Chairperson

Functional materials require molecular organization to transport charges. This dissertation goes beyond typical molecular organization and focuses on three types of molecular organization: an optical lattice, covalently bound cages, and disorganized liquid interactions.

Aluminum monochloride (AlCl) has been proposed as a promising candidate for laser cooling for organization in an optical lattice. In chapter 3, we show that pulsed-laser ablation of stable, non-toxic mixtures of Al with alkali or alkaline earth chlorides can provide a reliable source of cold AlCl molecules. We model the AlCl production in the limits of nonequilibrium recombination dominated by first-encounter events and find that AlCl production is limited by the solid-state densities of Al and Cl atoms and the recondensation of Al atoms in the ablation plume. This new source of AlCl molecules will provide the basis for future laser cooling experiments.

Covalent assemblies of conjugated organic chromophores provide the opportunity to engineer new excited states through structural organization. A newly developed triple-

stranded cage architecture, where covalent aromatic caps attach three conjugated walls, can be used to tune the properties of thiophene oligomer assemblies. In chapter 4 a variety of spectroscopic experiments are used to show that excited state properties of a benzene capped cage are dominated by through-space interactions between the chromophore subunits, generating a neutral H-type exciton state. Switching to a triazine cap enables electron transfer from the chromophore-linker after the initial excitation to the exciton state, leading to the formation of a charge-transfer state. The ability to interchange structural components with different electronic properties while maintaining the cage morphology provides a new approach for tuning the properties of chromophore assemblies.

In chapter 5, the ability of disorganized molecular assembly, a liquid, can be used to generate work. A high-energy nanosecond laser pulse is used to impulsively heat an aluminum plate resulting in the rapid heating of an adjacent liquid. The volume expansion from the liquid→gas transition propels the aluminum plate upward with an initial velocity up to 4 m/s. A simple model is developed to quantitatively describe the fluid dependence on the heat of vaporization. Furthermore, this method proves that pulsed later heating for liquid→gas actuation is an efficient way to convert light energy into kinetic energy, with efficiencies approaching 2%.

TABLE OF CONTENTS

LIST OF FIGURES

LIST OF TABLES

Chapter 1: Introduction

1.1 Ordered Molecular Materials to Functioning Electronics

The properties of any solid-state material are determined by its molecular components and geometrical arrangements. Solid-state crystals have long provided a basis for the molecular ordering of a material, as they are naturally abundant on Earth. These molecules align together in a uniform ordering, based on their intermolecular forces, to create a crystal lattice. This provides a pathway for tuning the solid-state properties of a crystal from a chemistry perspective, where a crystal could be synthetically tuned based on known atomic and molecular properties. Therefore, new crystals are synthesized and researched for applications in functioning materials. The link between the nanoscopic properties and macroscopic function is the key to the use of a material. In this dissertation, different strategies will be thoroughly examined for new types of molecular organization of materials. The idea is to go beyond traditional crystalline molecular materials and study the potential of new systems for functional materials.

To provide a basis for understanding the requirements of order, we will analyze molecular systems in two limits, from new types of molecular ordering to fully disorganized molecular interactions. First, we will focus on gas-phase diatomic molecules cooled to quantum degeneracy to generate a new optical lattice. Second, we will look at a new covalently bound molecular structure that supports delocalized excitons and charge

transfer states. And lastly, we will study a novel photomechanical system that uses a liquid→gas phase transition to convert light energy into mechanical energy. The three systems analyzed will provide specific evidence for the link between organization and function and provide a basis for new classes of functional optoelectronic materials.

1.2 Different Types of Organization

Technological advancements stem from research at the fundamental or molecular level. An electronic device typically consists of a uniformly ordered array for charges to easily move throughout.[1] With the search for new materials that can be molecularly organized for a given application, the design and study of novel systems, beyond molecular crystals, is vital. This can be broken down into the three types of matter: gas, solid and liquid phase materials. Gases are freely expanding, with no fixed shape or volume, meaning their molecular components are completely disordered. With the advancement of laser technology, the ability of ordering gaseous atoms and molecules in an optical lattice became possible. Stabilizing and studying new ordered gas-phase materials will allow the ability to unlock new quantum phenomena and the ability to stabilize a new state of matter. This could also lead to a better design and understanding of condensed-phase materials.

Crystalline solids provide ordering through ionic, covalent, metallic, or van der Waals forces to hold together the bulk material.[2] New ways of organizing condensed-phase materials are possible through synthetic routes, in which covalent bonding provides a way for ordering a non-crystalline solid. These types of organized systems aid in understanding time-resolved dynamics and how to most efficiently turn light energy into electrical

potential energy. Lastly, organized molecular crystals are not always necessary to promote mechanical work. With this idea, molecular disorganization based on long-range liquid interactions can be used for mechanical actuation. This idea can be used to assess how organization relates to mechanical actuation. Below, we will discuss the current state of the field and three strategies for organization at the molecular level that will be expanded upon in chapters 3-5.

1.3 Functions of Organization

The ability of a material to change its properties due to external stimuli is the basis of many devices, including those that transform photon energy from light into usable electrical or mechanical energy.[3] These materials are at the forefront of many different types of industries that work on optoelectronic devices, such as quantum computing,[4–7] crystal engineering,[8,9] photomechanical actuators,[10–15] photovoltaic solar cells,[16–19] light emitting diodes (LEDs),[20–23] energy storage,[24–29] and more.

With light being the most abundant resource, photons provide a useful way to supply an external stimulus. Photons can be localized and used having the power to replace chemical fuels and electrons as energy transporters in functional materials. Below, three different functions of molecular organization will be introduced including quantum arrays, energy and charge transfer, and mechanical actuation. All of these functions rely on photons to understand the inherent physical properties of the molecular system.

1.3.1 Quantum Arrays

Quantum arrays of trapped molecules present a basis for quantum computing qubits that can solve the computational requirements of long-range interactions that are highly controllable.[30,31] Molecules have rotational, vibrational, and translational modes that make up their electronic structure and these modes determine the stability of a molecular configuration. The Maxwell-Boltzmann distribution relates the temperature of a gas to the velocity distribution of atoms and molecules within the gas.[32] At high temperatures, in the gaseous state, chemical bonds can be energetically broken to stabilize molecules that are unstable at room temperature. On the other hand, in the regime of cold or ultracold temperatures, translational modes can be energetically frozen from nano-kelvin to milli-kelvin to eliminate translational degrees of freedom. With the advancement of laser technology, laser cooling emerged, where uniform absorption followed by emission in every direction results in momentum transfer, thus slowing the atom or molecule.[33,34] Alkali metals have been studied for laser cooling because of their potential well overlap according to the Franck-Condon principle.[35] In laser cooling, this predicts the probability of excited electrons to quickly return to the ground state without changing vibrational state, which means that the cycling of absorption-emission processes would be high.

When the energetic modes in a molecule are frozen, they reach quantum degeneracy and begin to behave like waves but still have mass and charge. This phenomena has been used to study novel states of matter, like the formation of a Bose-Einstein condensate (BEC), where all particles occupy the same state and have the same quantum wavefunction.[36–38] When molecules are moving this slow, all steps of a complex chemical

reaction could be more easily monitored. This is of interest in the chemistry, physics, and materials science communities to study many different emerging areas like precision measurements, quantum information, and simulated condensed matter systems. Ultracold molecules offer the advantage of having complete control over all degrees of freedom to see very small changes in a measurement. Furthermore, if these molecules can be frozen and trapped for a long period of time, they may have the ability to carry quantum information without loss.[39,40]

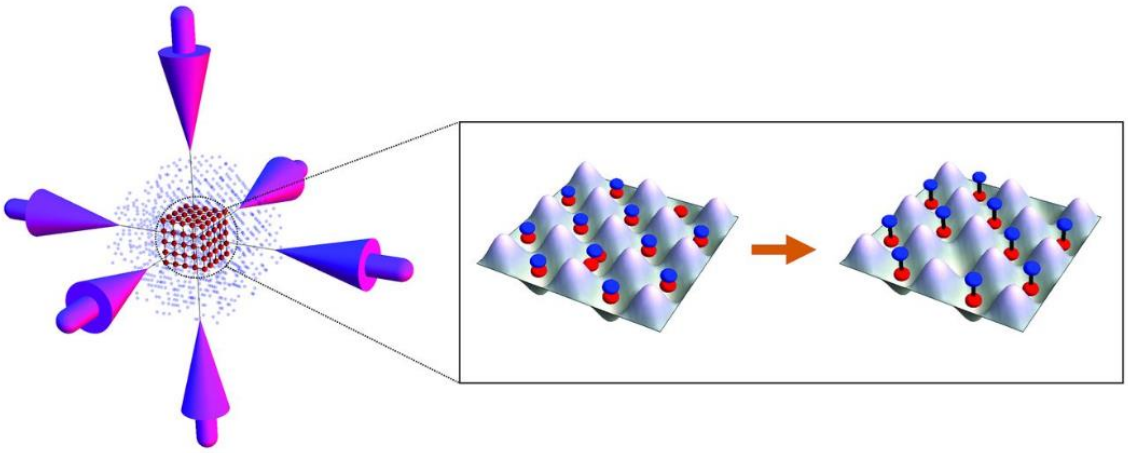

Figure 1.1. (Left) Schematic of a 3D optical lattice created by the laser interference pattern, pink arrows. (Right) Potential wells of optical lattice, where cold molecules are trapped. In this case, the optical lattice is filled with potassium (K) and rubidium (Rb) atoms to form KRb polar molecules. Figure from Steven A. Moses, Jacob P. Covey, Matthew T. Miecnikowski, Bo Yan, Bryce Gadway, Jun Ye, and Deborah S. Jin, Creation of a low-entropy quantum gas of polar molecules in an optical lattice, Science, 2015, 350(6261), 659-662.[41] Reprinted with permission from AAAS.

Laser cooling first emerged with atoms like sodium[42,43] and helium;[44] followed by many nonpolar diatomic molecules, the first of which was Na_2[45] and Rb_2.[46] In more recent years, many polar diatomics, like CaF[47–49] and YO,[50] and even polyatomics are of interest because of their applicability to real-world condensed phase systems. After a particle is cooled to nanokelvin temperatures, it can be loaded into an optical lattice, which is an

optical interference pattern created by intersections of laser beams seen in **Figure 1.1**. This lattice has parallels to a condensed phase crystal lattice where the particles are instead locked into place in the potential wells created by the beam interference. One advantage of cooling and trapping polar molecules is that they can be controlled with external electric and magnetic fields because of their large permanent dipole moment. This offers the ability to have a highly controllable lattice using external fields to study different properties of simulated crystalline materials that could not be synthesized as a crystal lattice in the condensed phase. This means that the simulated crystal can be tuned without applying any physical strain, in which novel quantum mechanics will arise.

While this field encompasses a large framework of complex physics phenomena, it presents a challenge from a chemistry perspective. The development of a new molecular optical lattice is dependent on the formation and yield of cold, unstable molecules. Therefore, new methods must be explored for the production of a high yield of cold molecules.

1.3.1.1 Using Laser Ablation to Create Unstable Gas-Phase Diatomics

As previously stated, there is a search for polar diatomic molecules that can be frozen and loaded into an optical lattice. AlCl is a candidate of interest for laser cooling because it has favorable predicted Franck Condon factors,[51–55] meaning it has a low probability of vibrational relaxation after absorption. This would allow for more molecules to be laser cooled, resulting in a higher concentration of AlCl. Since AlCl is a highly reactive open-shell molecule, it is unstable at room temperature, typically requiring high temperature

methods to produce through the pyrolysis of $AlCl_3$, >1000 K.[56–63] Since the objective is to have cold molecules, laser ablation can be used to trap a high concentration of the molecule of interest in a pre-cooled environment of buffer-gas helium ≈ 4 K.[64] This has previously been done to produce AlCl from $AlCl_3$.[65] Laser ablation is the process of vaporizing a solid with a high energy laser pulse in which random distributions of gaseous fragments will form, as seen in **Figure 1.2**.

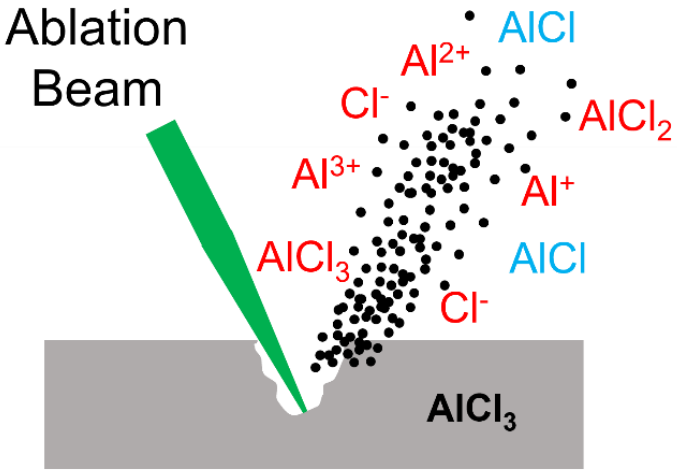

Figure 1.2. Schematic of laser ablation of solid sample. The ablation laser beam is focused with a high energy density onto a sample in which gaseous fragments of different chemical species will expel into a plume (black dots). If the solid sample was $AlCl_3$, a distribution of ions, as well as AlCl species would be expected in the gaseous plume.

This technique offers the advantage of having a high density of pre-existing molecules (typically $>10^8$ molecules) before laser cooling so other forms of synthesis are not necessary, like photoassociation or Feshbach resonances which typically result in a total number of molecules around 10^5.[9] Instead, ablation offers a robust way to generate a molecular distribution, based on the precursor used, after multiple laser pulses. The disadvantage of this method is that a random distribution of molecular species will be generated from ablation and there must be a stable, consistent precursor available that can

be used. There are many different precursors to form AlCl; virtually any aluminum source can be mixed with any chloride source. In efforts to produce the highest concentration of AlCl from laser ablation, an extensive study of the chemical precursors is necessary.

1.3.2 Energy Transfer and Charge Transfer

To make any electrical material "work," energy must be supplied to the system. In traditional devices, electricity is supplied from a power plant that relies on burning coal to produce energy. The amount of electricity consumed globally increases every year and is expected to reach $4.5 \cdot 10^8$ TJ by the end of 2022.[66] As the global climate continues to suffer from the burning of fossil fuels to supply electricity and power to the world, we must turn to renewable energy sources. Sunlight provides the most abundant form of natural energy in the form of wave-like packets called photons. In one hour, $1.0 \cdot 10^7$ TJ of sunlight hits the Earth,[67] meaning we could power the entire globe for more than one year with just two days of sunlight if this energy could be efficiently extracted. Although technology is continuously advancing, there still exist many challenges in effectively converting sunlight into usable energy. With an understanding between the order and function of molecular systems and the scalability into a functioning material, the possibility of replacing current electrically powered devices with photon-powered systems becomes possible.

An emerging area in light harvesting materials is organic-based devices for the electronics and photonics industries.[16,68] Currently the inorganic semiconductor, silicon, is leading this industry, commonly seen in photovoltaic solar cells and other electronics. But organics, usually in the form of plastic, offer ideal properties like low cost, flexibility, and

versatility.[69] Furthermore, these structures are easily chemically synthesized and processed. A system of focus is π-conjugated oligomers and polymers because of their nonlinear optical properties and semiconducting properties.[16,69] Currently, much work is put into the synthesis of new conjugated organic chromophores that interact to occupy new electronic states that have trapped excitons or separated charges for energy conversion processes.[17] The efficiency of the chromophore's charge separation is dominated by the supramolecular packing of the structure.

These designs often utilize an electron-rich donor linked to an electron-deficient acceptor in a π-conjugated assembly to facilitate energy and electron transfer. Through the absorption of light, the electrons are excited to a new state where they can an electron can separate into and electron-hole pair because of the separation between the donor and acceptor. The electron-hole pair stills feel coulombic attraction but can become delocalized across a conjugated network, in an excitonic state.[70] Many systems focus on tuning this network to create delocalization for a longer period across a larger distance, limiting recombination. In practice, these charges could then be extracted in a device, like a photovoltaic cell or LED. A focus here is that the design of conjugated organic chromophore assemblies will lead to the tuning of the excited state for the desired application.

1.3.2.1 Photophysics

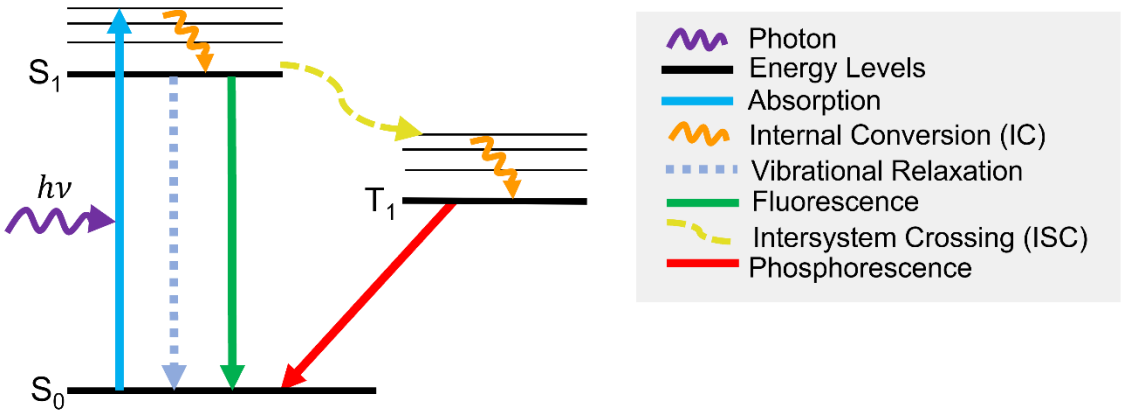

Figure 1.3. Jablonski diagram of common excited state relaxation pathways. Photon energy is absorbed to promote electrons from the singlet ground state (S_0) to some singlet excited state, and then internally converts to the lowest energy excited state (S_1). Then the electron can vibrationally relax, fluoresce, or intersystem cross into the triplet manifold (T_1) with the potential to phosphoresce back to the ground state.

The systems discussed in this work can be explained energetically with the Jablonski diagram in **Figure 1.3**. Photoreactive materials absorb photons within their band gap, promoting their electrons to a singlet excited state (S_n) within 10 fs. This electron will undergo rapid internal conversion (IC) to the lowest energy singlet state (S_1) on the order of ps. From here, the electrons can non-radiatively decay through vibrational relaxation back to the ground state, in which heat is released. Or the electron can radiatively relax through the emission of a photon through fluorescence, on the order of ps to hundreds of ns. If the electronic structure of a molecular system has sufficient singlet-triplet overlap, the electrons can spin flip into a triplet state (T_n) through intersystem crossing (ISC). This process must dynamically outcompete other non-radiative or radiative processes. From here, the electron will internally convert to the lowest energy triplet state (T_1) before it can

non-radiatively relax or emit a photon through phosphorescence, which occurs from μs to ms.

Molecular organization can change the electronic properties of a given material, as charges are easier to move through an ordered array. The electronic structure of a molecular system is determined by its atomic components, geometry based on steric interactions, and chemical environment. The complexity of these energetics from system to system demands photophysical characterization and understanding as new molecular materials are discovered. Coupled with current technological advancements in synthesis and instrumentation results in a pathway to better understand how to tune the properties of a photoreactive material to the desired application.

1.3.2.2 Tuning the Electronic Properties of Bithiophene Chromophores

Historically, many conjugated molecules have been studied in dilute solution to gain insight into intermolecular energy transfer between two molecules close to one another.[71–73] The drawback of this is the lack of control between the donor and acceptor in terms of geometrical arrangement. For this reason, covalently tethered bichromophores have attracted much interest due to the ability of electron-donors to be bonded to the electron-accepting linking group or "bridge" to promote intramolecular charge transfer.[74–77] Specifically, thiophenes are the basis of a lot of conjugated polymers in organic solar cells because of their synthetic understanding and structural versatility coupled with their electron donor behavior.[75,78–96] Sulfur atoms have high polarizability that makes a prominent contribution to the electron-donating and charge-transport properties. When a

π-conjugated bridge links with a thiophene acceptor, electron transfer can be facilitated across the network. The electron transfer rate is determined by the length of the conjugated chain, the functional groups used as the electron acceptors, and the stereochemistry.[97] Therefore, the molecular structure has the potential to be tuned synthetically based on the desired properties. The donors and acceptors are chosen based on the compatibility of energetics, solubility, and crystallinity. In the past two decades, by tuning the structures of oligothiophenes, the power conversion efficiency has increased by 20%.[98]

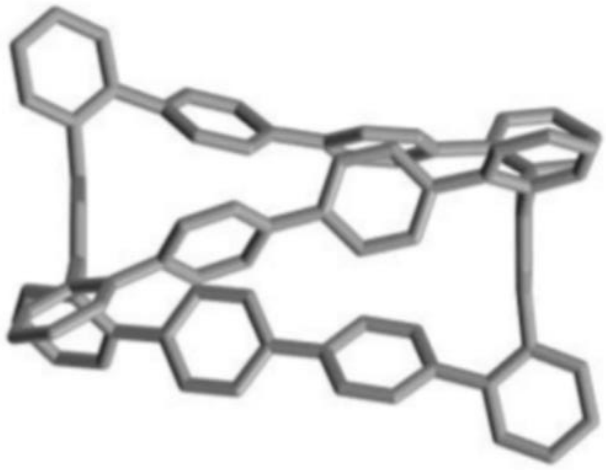

Figure 1.4. Triple-stranded phenylene cage synthesized by the Krische Lab at the University of Texas at Austin.[99] Reprinted with permission from Hiroki Sato, Jon A. Bender, Sean T. Roberts, and Michael J. Krische, Helical Rod-like Phenylene Cages via Ruthenium Catalyzed Diol-Diene Benzannulation: A Cord of Three Strands, J. Am. Chem. Soc., 2018, 140(7), 2455-2459. Copyright 2018 American Chemical Society.

Many of the studied compounds consist of multiple straight-chained chromophores that facilitate electron transfer across a bridging group or a network of dendrimers.[78,80,82,86,89,100,101] Furthermore, the typical excited state population in bithiophene chromophores intersystem crosses within 200-300 ps[95,101,102] resulting in a weak fluorescent yield. These types of structures are conformationally flexible in nature,

in which multiple conformations can exist at once, leading to very different energetics and dynamics. This complicates the link between structure and performance that would be essential for use in electronic devices. This led to the synthesis of a new triple-stranded phenylene structure held together by two capping groups on each end, as seen in **Figure 1.4**.

This geometry forms a covalently bound rigid cage where the conjugated chains are now structurally constrained, not allowing for much conformational freedom. The structure of this phenylene cage provides a link between nanoscopic molecular organization and controlled properties of the system. Although this geometry is still far from crystalline order, it presents a large leap toward ordering energy transfer networks for functional materials. These new synthetic methods provide the basis for different cage compounds where bithiophenes could be incorporated to facilitate donor-acceptor properties. This would directly impact the electronic structure that determines the dynamics. The ability to unlock new excited state geometries correlated to the structure of functional groups will allow for the use of these chromophores macroscopically in devices.

1.3.3 Photomechanical Actuation

To assess the photophysical properties of a molecular system, it must be spectroscopically explored. The use of the laser to supply photons is important in understanding of the kinetics and dynamics of nature at the atomic level as it provides a way to precisely tune the wavelength, duration, and phase of light. A laser source can be localized to one area, unlike an incoherent light source that rapidly expands in all

directions. Lasers have the ability to gently probe electrons internal to a molecule or completely ablate the surface of a material, depending on the energy regime. Furthermore, a laser can be used in a continuous wave of photons or be compressed into a short pulse, dependent on the desired energy density. This allows for a larger dose of energy into a system to manipulate the excited states and therefore the performance of a material. The following sections will use these basic principles, changing a laser's wavelength, duration, and intensity of light to understand the fundamentals of molecular systems that transduce light into mechanical motion.

1.3.3.1 Organized Crystals

A commonly studied class of crystalline materials are photoreactive, resulting in a mechanical change through isomerization, dimerization, cyclization, or dissociation.[103] These photoswitches have long been used in the solid-state because the chemical reaction results in a structural rearrangement through a change in crystal packing. Diverse materials from single molecular crystals to composite materials filled with a crystal array can be used to convert photons into mechanical work;[13,14,104–108] but knowledge of maximizing the efficiency of these systems in a macroscopic device is still being expanded upon.

The ordering of these materials from the microscopic to macroscopic regime has shown they can do meaningful work. In **Figure 1.5**, a diarylethene (DAE) derivative is shown (top) to undergo a ring-open to ring-close isomerization upon UV irradiation and then reacts back to the ring open form upon visible irradiation.[109] The corresponding crystal

(bottom) results in bending from expansion of the molecular structure putting strain on the crystal lattice. This occurs on the order of 300 μm, but the extension of this to centimeters has now been done to produce macroscopic motion.

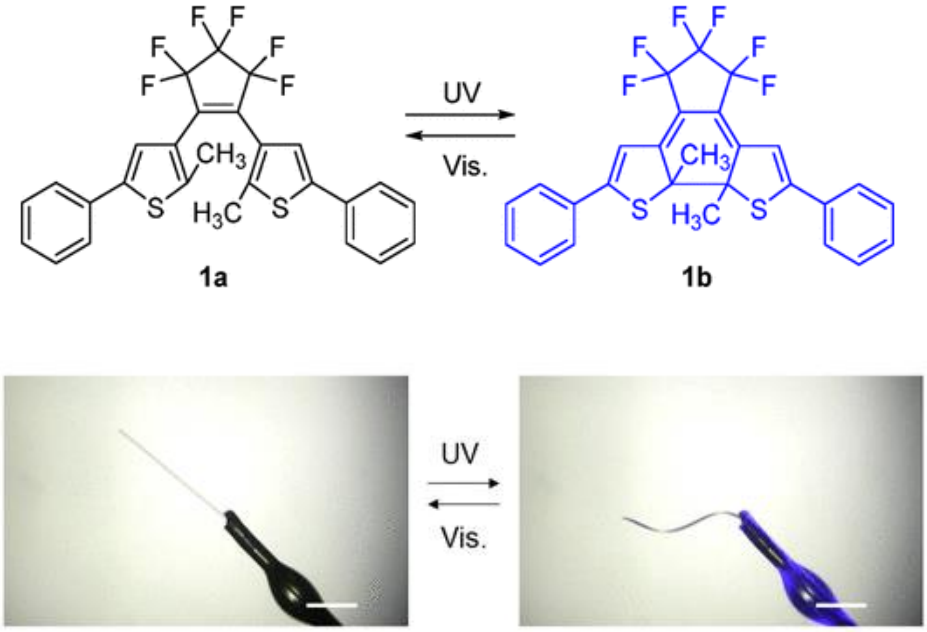

Figure 1.5. (Top) Molecular structure of the diarylethene (DAE) derivative 1,2-bis (2-methyl-5-phenyl-3-thienyl)perfluorocyclopenten that undergoes a ring-open to ring-closed cyclization when irradiated with UV light. Upon visible light irradiation, it photoconverts back to the ring-open form. (Bottom) When crystallized in ribbons, reversible crystal twisting can be seen between ring-open and ring-closed forms due to the change in crystal packing.[109] Reprinted with permission from Daichi Kitagawa, Hajime Tsujioka, Fei Tong, Xinning Dong, Christopher J. Bardeen, and Seiya Kobatake, Control of Photomechanical Crystal Twisting by Illumination Direction, J. Am. Chem. Soc., 2018, 140(12), 4208-4212. Copyright 2018 American Chemical Society.

In **Figure 1.6**, the same DAE derivative was grown in a porous template to produce uniform expansion upon irradiation that resulted in mechanical work, lifting a mirror 12,000x its mass.[107] Although this is a leap forward in usable photoreactive materials, these systems still suffer from low optical penetration and poor kinetic energy conversion

efficiencies ($\eta \approx 10^{-5}$ %).[107,110] A basic limitation in efficiently scaling molecular materials into usable photo-actuators is the timescale of irradiation and effectively converting energy into mechanical motion.

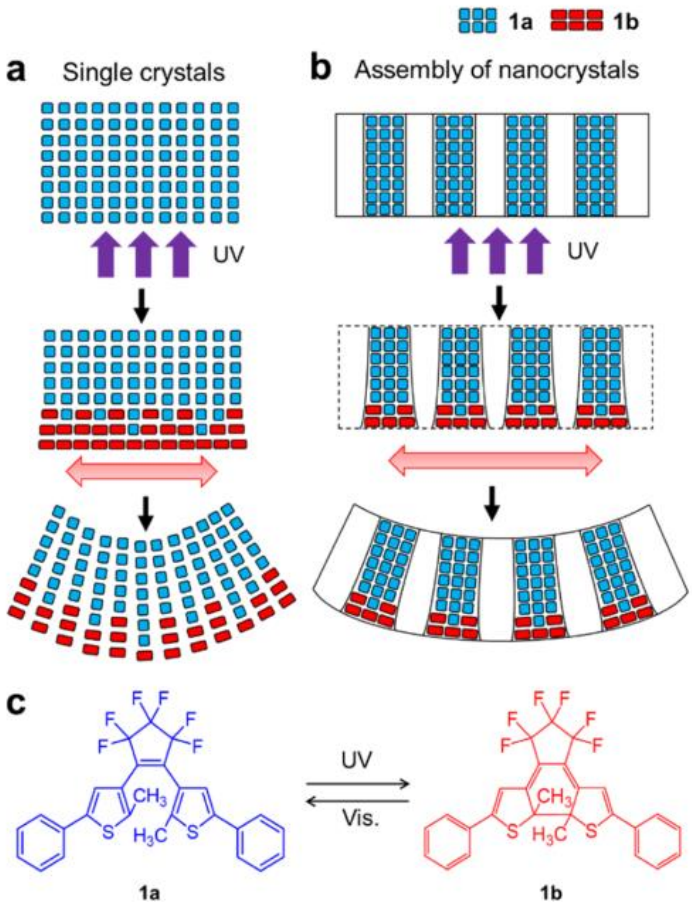

Figure 1.6. Schematic of DAE derivative that photoconverts from ring-open (blue) to ring-closed (red) form to bend single crystals (a) or ordered template (b). Without the composite template, the single crystals undergo asymmetric expansion. With the composite template, the ordering of the crystal nanowires allows for uniform bending of the structure.[107] Reprinted with permission from Xinning Dong, Fei Tong, Kerry M. Hanson, Rabih O. Al-Kaysi, Daichi Kitagawa, Seiya Kobatake, and Christopher J. Bardeen, Hybrid Organic-Inorganic Photon-Powered Actuators Based on Aligned Diarylethene Nanocrystals, Chem. Mater., 2019, 31, 1016-1022. Copyright 2019 American Chemical Society.

Another factor to take into consideration when trying to increase the efficiencies of mechanical materials is to understand the thermal energy put into the system through laser heating. To further analyze systems that convert light into mechanical work, we will transition from photochemical actuation to photothermal actuation in the next section.

1.3.3.2 Disorganized Thermal Expansion

In photomechanical materials, the absorption of photons can also drive a thermal reaction that can move the material through a volume increase. In a phase change material (PCM), thermal heating can be used to induce a solid→liquid or liquid→gas phase change which results in a mechanical actuation, generating a work output of the bulk.[25,29] A solid→liquid phase transition results in a relatively small volume expansion on the order of 10-15%, causing a physical mechanical motion to power an actuator.[111–114] To harness an even larger motion, a liquid→gas phase transition can be contained to have a larger mechanical motion due to the larger volume expansion. This phenomenon has long been used in steam engines and is more recently used in the robotics industry to move liquid-filled polymer materials when heated.[115–120]

Wang and co-workers developed a light-driven liquid-vapor soft actuator out of a polymer and carbon nanotube sandwich structure as seen in **Figure 1.7**.[121] They encapsulated different organic solvents as the working fluid that would volatilize and expand upon light irradiation and recondense to recover to the original position. The significance of this study is shown in **Figure 1.7C**, in which it has the fastest actuation time, on the order of tens of milliseconds, of all other liquid-vapor actuators to date.

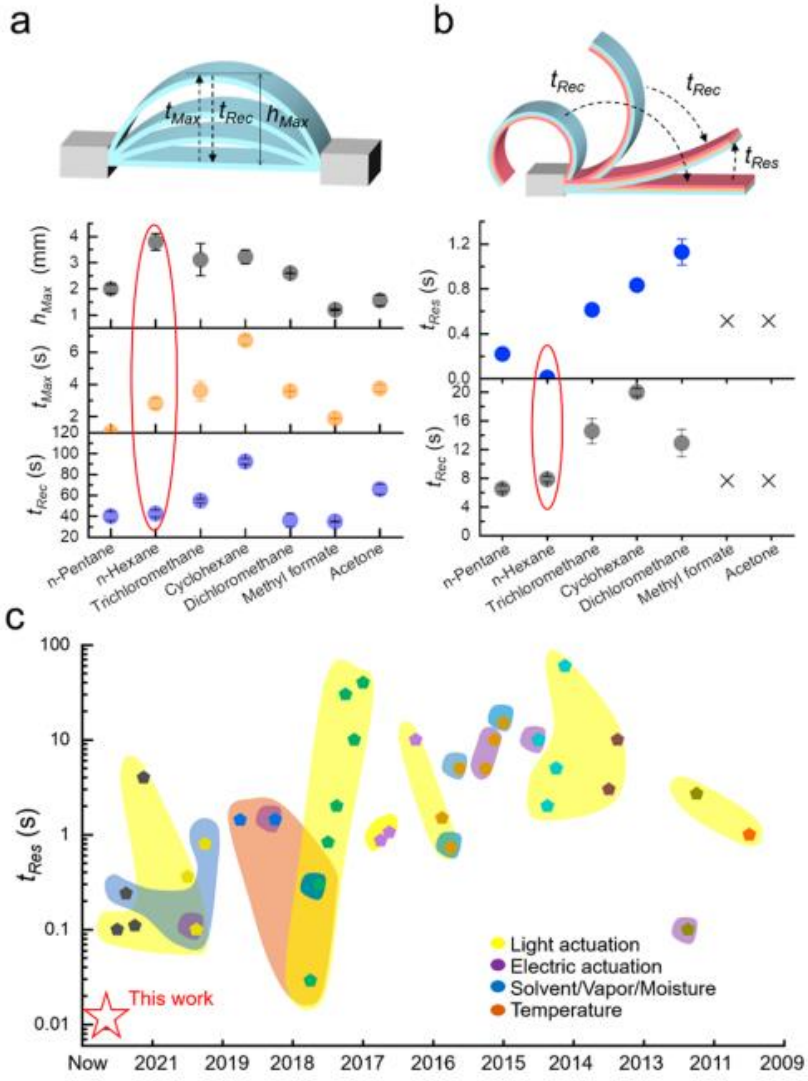

Figure 1.7. Schematic[121] of two different soft actuators developed and their performance with different embedded solvents, analyzed based on max height (h_{max}), time to max height (t_{max}), and recovery time (t_{rec}). (a) Actuator is made of a polydimethylsiloxane (PDMS)/carbon nanotube (CNT) active layer. (b) Actuator is made of a PDMS/CNT active layer sandwiched with a polyvinylidene fluoride passive layer. (c) Response time is plotted with all other literature soft actuators that are driven by light,[121–145] electric stimuli,[143,146–150] solvent/vapor/moisture,[133,139,140,151–156] and temperature.[133,140,141,157] Reprinted with permission from Miao Wang, Lei Zhou, Wenyan Deng, Yaqi Hou, Wen He, Lejian Yu, Hao Sun, Lei Ren, and Xu Hou, Ultrafast Response and Programmable Locomotion of Liquid/Vapor/Light-Driven Soft Multifunctional Actuators, ACS Nano, 2022, 16, 2672-2681. Copyright 2022 American Chemical Society.

Furthermore, they point to alkane solvents having the best combinations of speed and performance of the actuator. Some of this work uses a light source but much of this research has relied on supplying the energy through resistive heating.

In any device that relies on thermal heating, the material absorbs heat and quickly diffuses through or into the surroundings. The rate at which diffusion takes place is determined by the thermal diffusion coefficient of the specific material. In continuous heating of a mechanical material, the energy input is in a constant battle with the rate of diffusion. For this reason, resistive heated materials have begun using pulses to improve the kinetic energy conversion efficiencies.[116,158–160] The idea here is to maximize the work output by supplying energy at a faster rate than it can diffuse. The disadvantage of this technique is that the timescale of a resistive pulse is long, on the order of microseconds. On the other hand, the thermal barrier can be overcome by using a laser source to locally heat through absorption, but efficiencies using a CW laser source are still low. Based on Carnot's theory, the maximum efficiency increases as the difference between the initial temperature and final temperature of the working fluid increases.[161] Therefore, in the efficiency of heat engines, the temperature gradient is linearly proportional to the efficiency. A pulsed laser has the advantage of supplying energy at a faster rate than thermal diffusion through a material. If a liquid can absorb enough laser energy instantaneously, a very large temperature gradient within the liquid could be achieved.

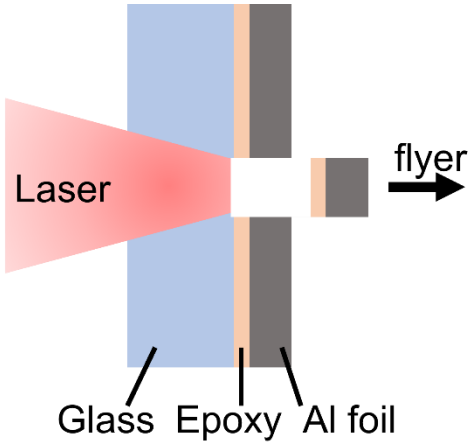

Figure 1.8. Schematic of simple laser flyer design where aluminum (Al) foil, typically 25-100 μm thick, is epoxied to a glass substrate and the flyer is ejected after a single laser pulse.

Another field that is interested in turning light energy into mechanical energy, for shock compression materials, works with laser fliers.[162–175] This type of system utilizes the rapid vaporization of a solid metal film with a strong laser pulse to move a material as shown in **Figure 1.8**. Basically, a single laser pulse induces a shock wave through the material and generates enough momentum to project the material at a high velocity. From there, the velocity can be converted into mechanical energy to measure the kinetic energy conversion efficiency of the system. The efficiencies of these laser fliers are approaching 50% by tuning the absorption properties at the surface of the thin metal films.[164,168] Much of the research in this field is focused on materials science and increasing the kinetic energy conversion efficiency by adding a monolayered material to the surface of the flier. The goal is to increase the percentage of laser pulse absorbed by adding a less reflective layer to the surface of the flier.[164,166,168–170,173] The disadvantage of these systems is that they are

microscopic, on the order of microns, and typically degrade after a single laser pulse under vacuum. To date, there has not been a macroscopic laser flier based on these principles.

Furthermore, there has not been any laser flier research that relies on a different mechanism, other than a solid→gas transition, to cause motion. Therefore, it would be beneficial to see whether a different phase surrounding the material would enhance the motion. Based on this idea, combining the laser flier technique with photothermal actuation discussed in the previous sections; a new photothermal actuator using a high-energy pulse to launch a flyer could provide new fundamental characterizations to both fields. If the absorptive material was surrounded by a liquid that is easily volatilized, the heat diffusion into this liquid could result in a very large gas expansion. This idea will be discussed more in chapter 5.

1.4 Preview of This Work

This work will present novel pathways to bridge the gap between molecular organization of assemblies and functional materials. The findings in chapters 3-5 aim to provide a pathway to develop the next generation of materials with improved function. Three specific photophysical questions will be answered:

(1) Can we optimize the production of cold AlCl molecules for laser cooling and optical lattice formation?

First, chapter 3 will focus on the formation of gas-phase AlCl in a helium buffer gas environment. Pulsed laser ablation is used to produce AlCl from mixtures of different alkaline earth chlorides with aluminum powder. The yield of AlCl is monitored with

absorption spectroscopy as a function of Al:Cl molar ratio to determine the optimal conditions for the highest yield. Most interestingly, a simple non-equilibrium model can quantitatively describe experimental data to prove that AlCl production is dominated by first-encounter events. This work provides the first insight into the chemistry that is occurring in an ablation plume and shows that the production of cold AlCl molecules is directly dependent on the solid-state chloride density. The optimized parameters found in this work provide a generalized method for the production of unstable laser coolable molecules after laser ablation. The experimental details will be outlined in chapter 2.

(2) Can we control the electronic properties of a covalent bithiophene cage by changing the capping unit?

Second, chapter 4 presents new conjugated organic chromophores in a triple-stranded cage architecture. These covalently bound thiophene oligomer assemblies present a new way to limit conformational freedom while tuning the dominant electronic properties. The excited state properties will be analyzed through time-resolved spectroscopic methods, discussed in chapter 2, and computation. This work shows that a benzene cap holding the bithiophene arms together on each end results in neutral Frenkel H-type exciton formation generated by through-space interchromophore interactions that lead to intersystem crossing. By switching to triazine capping units, a charge-transfer state forms that can outcompete the intersystem crossing dynamics and enhance the fluorescence quantum yield. This work provides the first example of tuning the properties of chromophore assemblies while retaining the morphology of the system. Furthermore, this architecture

can be generalized and used for future studies in controlled excited state dynamics for material applications.

(3) Can disordered materials undergo a photoinduced phase transition to increase the efficiency of photomechanical actuation?

Third, chapter 5 will discuss a new type of photomechanical actuation that relies on rapid thermal heating that can outcompete heat diffusion. Instead of an ordered molecular structure, this system relies on long-range molecular interactions in a liquid and its characteristic volume expansion. This work proves that a high-energy laser pulse is an efficient way to convert light energy to mechanical energy, in which the basic principles could be applied to a functional actuator. It further proves that solid-state molecular ordering is not always required for functional materials.

While the three systems that have been studied here are different in chemical nature, they provide a link between molecular properties and material functionality. The necessity of order for functionality will be assessed and understood from a chemical and thermodynamic standpoint. Furthermore, their function is dependent on light irradiation and will further pave the path toward sustainable materials.

Chapter 2: Experimental

In this chapter experimental details are provided for the three systems studied, whose results will be described in chapters 3-5. First, the preparation of solid-state Al:Cl samples will be described, including attachment to copper target. Then the spectroscopic measurements of AlCl will be explained, with brief details on the laser setup and an image of a typical sample and its signal. Second, the synthesis and computational details of bithiophene monomers and cages will only be briefly mentioned, as they were done by our collaborators.(CITE) Then the spectroscopic measurements will be thoroughly explained, including steady-state absorption and fluorescence, quantum yield (QY) measurements, time-resolved photoluminescence, and femtosecond transient absorption (fs-TA). Furthermore, the alignment from the titanium sapphire (Ti:Sapph) femtosecond laser to the fs-TA spectrometer will be outlined and optimization using a laser dye will be explained. Lastly, the development of a liquid holding launch pad for aluminum plate propulsion will be explained with images of a typical setup. Then the operation of the neodymium-doped yttrium aluminum garnet (Nd:YAG) laser will be outlined, with the specific laser line used to propel the aluminum.

2.1 AlCl Target Study

2.1.1 Target prep

XCl_n chloride powders and aluminum powder were homogenously mixed to form pellets for the target study. A variety of increasing Al:Cl molar ratios of 1:25 to 10:1 were made for Al:KCl by mixing 99.95% aluminum powder <75 um (Sigma-Aldrich) 99% with

BioXtra potassium chloride (KCl, Sigma-Aldrich). Only a 1:4 molar ratio of Al:Cl was made for the rest of the chloride sources consisting of, crystalline sodium chloride (NaCl, Fisher Scientific), 98% anhydrous magnesium chloride ($MgCl_2$, Sigma-Aldrich), and anhydrous calcium chloride ($CaCl_2$, Fisher Scientific). Pure 98% sublimed, anhydrous aluminum trichloride ($AlCl_3$, Sigma-Aldrich) was pelletized for the $AlCl_3$ sample.

Each mixture was stirred until homogenous and pelletized between two anvils in a 12 mm pellet die. They were pressed at 6000 psi for 1 minute using a hydraulic press. After removing from the pellet die, they were glued to a copper target using epoxy (Stycast 2850FT). All samples were allowed 24 hours in air for the glue to cure before loading into the experimental chamber, except $AlCl_3$ that was wrapped in parafilm for 4-5 hours of curing. The copper cell with the sample glued to it was then loaded into the ablation vacuum chamber.

2.1.2 Spectroscopy

The spectroscopic measurements were performed by our collaborators[65,176] and the experimental schematic can be seen in Figure 2.1. In summary, the sample pellet was loaded into a cryogenic buffer gas cell with flowing liquid helium to reach 4.2 K. The sample target is then laser ablated by a 80 um focused beam with 14 mJ of 532 nm at 1 Hz. The ablation plume then passes through a spectroscopic window where a CW 261.5 nm laser is selectively absorbing AlCl to monitor the production concentration. Absorption measurements are also performed on K at 767 nm and Al at 395 nm to monitor the production of the dominant species in the cell after laser ablation. As the ablation beam

scans the sample as the absorption is monitored using an amplified photodiode to generate an image of the target, as seen in Figure 2.2.

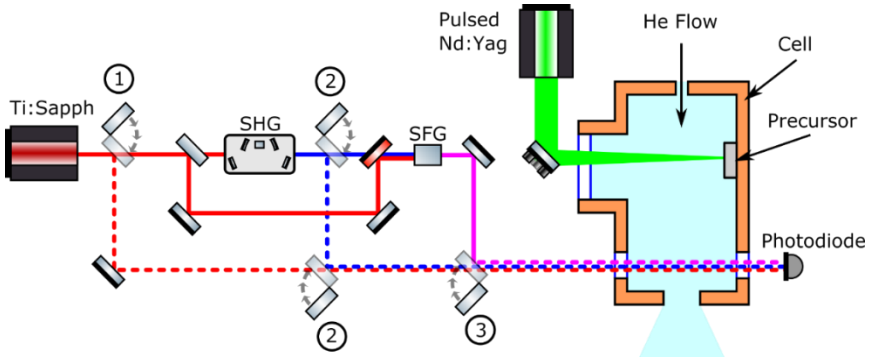

Figure 2.1. Schematic of the experimental apparatus. The flip mirrors (1, 2 and 3) allow for the frequency range selection. Configuration (1) uses the Ti:Sapph output at 766 nm (red) directly for measuring K. Configuration (2) uses the SHG output (bow-tie cavity with LBO crystal) at 395 nm (blue) to measure Al and (3) uses the THG output from a BBO crystal at 261.5 nm (violet) to measure AlCl absorption.

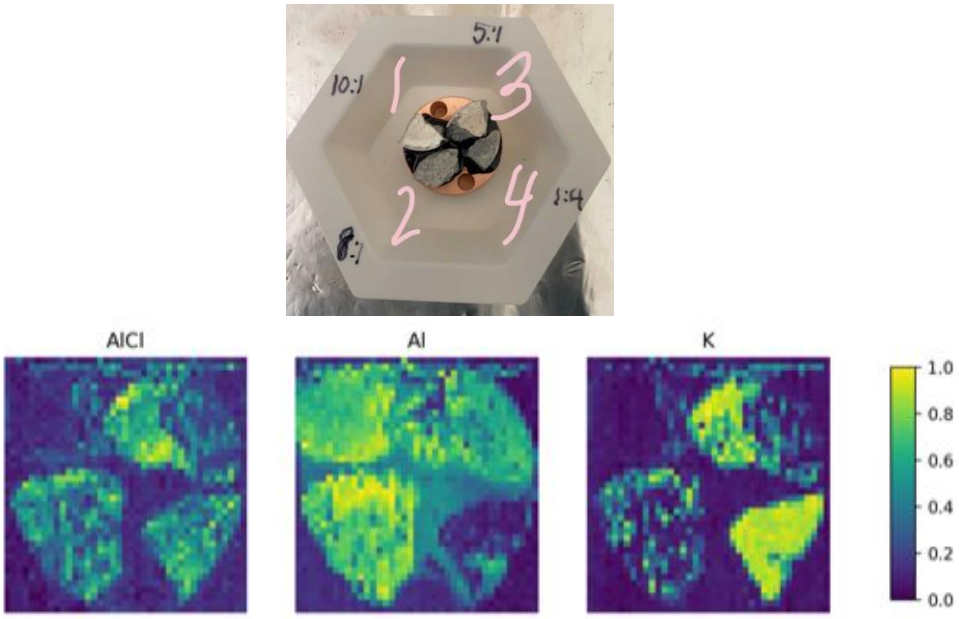

Figure 2.2. (A) Sample target with various Al:KCl molar ratios, as labelled in pink (1) 10:1, (2) 8:1, (3) 5:1, and (4) 1:4. (B) Target mappings for absorption of AlCl, Al, and K. The color map on the right shows the variation in AlCl absorption from 0 (dark blue) to 1 (yellow).

Each transmitted data point is measured and the optical density is quantified by $-\log_{10}\left(\frac{I_0}{I}\right)$, where I_0 is the transmitted signal before the ablation plume is present. The signal is averaged over at least 50 spots on the target from 1-3 ms after the ablation laser pulse for each spot to generate a time-dependent absorption trace.

2.2 Cages

2.2.1 Synthesis

Synthesis and synthetic characterization of all thiophene monomer and cage compounds were done by our collaborators.[79] The novel synthesis procedures are described in chapter 4. Characterization included proton nuclear magnetic resonance (^{1}H NMR), carbon nuclear magnetic resonance (^{13}C NMR), electrospray ionization time-of-flight mass spectrometry (ESI-ToF-MS), infrared spectroscopy, and X-ray crystallography.

2.2.2 Computational Details

All computation was done by our collaborators.[79] Briefly, the equilibrium geometries of all compounds were defined at the ωB97X-D/6-31+G(d) level in the gas phase, cyclohexane, and acetonitrile. From the optimized structures, vertical transitions were computed to further analyze the excitation energies by thermal activation of low-frequency modes.

2.2.3 Steady-State Absorption and Fluorescence

An Agilent Cary 60 UV-Vis spectrophotometer and a Horiba PTI QM-400 fluorescence spectrophotometer were used to collect absorption and emission spectra, respectively. All solid samples were made into dilute solutions ($\approx 2 \cdot 10^{-5}\ M$) using chloroform, toluene, and cyclohexane. For emission spectra, a 350 nm excitation wavelength was used with a 2 nm bandpass. All solutions were purged with argon for 15 minutes and sealed prior to collection to remove oxygen from the sample.

The emission spectra of **4a** and **6a** are compared by using a gaussian peak fitting function, described by Equation 2.1, to show the diminished 0-0 vibrational peak. The parameters of the peaks are shown in Table 2.1, where the peak width (w) and full width half max (FWHM) were fixed in each spectrum. This allowed the peak center (xc), area, and amplitude (A) to vary. Then peak 1 for **4a** could be quantitatively compared to peak 1 of **6a** to prove the decrease in the 0-0 vibrational peak.

$$y = Ae^{-0.5(\frac{x-xc}{w})^2}$$

Equation 2.1. The equation for each gaussian peak fit with the fitting parameters in Table 2.1.

		xc	w	A	FWHM	Area
4a	Peak 1	22700	700	97202	1648	1.706
	Peak 2	21350	700	123245	1648	2.163
	Peak 3	20000	700	70354	1648	1.234
6a	Peak 1	22900	600	201858	1412	3.036
	Peak 2	21550	600	205078	1412	3.084
	Peak 3	20200	600	104429	1412	1.571

Table 2.1. Parameters used to fit the three gaussians in Figure 4.11 are shown. The equation of each gaussian is shown in equation 2.1, where A is the peak amplitude, xc is the peak center, and w is the width of the peak. Each peak was fit with equal spacing of 1350 cm^{-1}.

2.2.4 Quantum Yield Measurements

Horiba's fluorescent quantum yield instructions provided a basis for these experiments.[177] The absorption and emission spectra were collected with an Agilent Cary-60 UV-Vis spectrophotometer and a Horiba PTI QM-400 fluorescence spectrophotometer, respectively. For the emission collection, a 1 nm bandpass and 350 nm excitation wavelength was used for each sample. Prior to absorption and emission measurements, each sample was purged with argon for 15 minutes to remove oxygen. The relative fluorescent quantum yields were determined by making 5 dilute solutions of increasing concentration, for each sample and comparing to a standard with a well-known fluorescent quantum yield. 9, 10-diphenyl anthracene (DPA) in cyclohexane was used as the standard because of its similar absorption and emission wavelength range to the cages and monomers being measured. In these experiments, the UV-Vis spectrometer and fluorometer must be kept turned on for the entirety of the experiment without zeroing or restarting the software between samples. This is to avoid any lamp drift or differences in zeroing the background. Further, if different samples are going to be run on different days, the standard must be remade and tested on the same day and in parallel to the unknown sample.

After the spectra were collected, the absorbance was plotted against the integrated fluorescence intensity for the solvent and five different concentration samples. The data points were then fit with a linear line to quantify the slope (m). The phenyl-compounds **4a** and **6a** and the triazine cage **4b** are plotted in Figures 2.3 and 2.4, respectively. Using the slope from the linear fit, the fluorescent quantum yield (Φ_{flx}) can be calculated,

$$\Phi_{flx} = \Phi_{ST}(\frac{m_x}{m_{ST}})(\frac{\eta_x^2}{\eta_{ST}^2})$$

where quantum yield of DPA (Φ_{ST}) is 0.90, and the slopes (m) were experimentally determined for each sample using the linear fits with an $R^2 > 0.9$. The refractive index (η) of the solvents used in each sample are also considered to correct for any differences due to a different solvent used in the sample versus the standard.

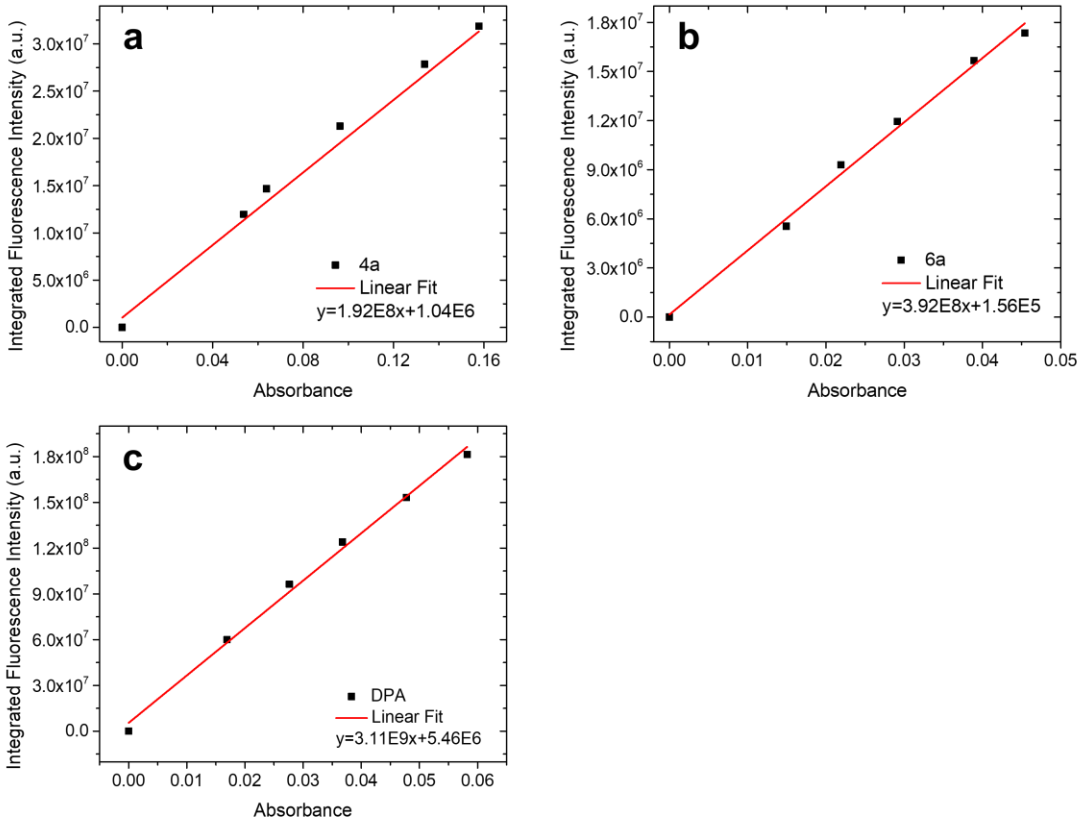

Figure 2.3. The absorbance was plotted against the integrated fluorescence intensity for the solvent and five different concentration samples for **4a** (a), **6a** (b), and DPA (c). The data points were fit with a linear line to obtain the slope (m) for the calculation of the fluorescent quantum yield.

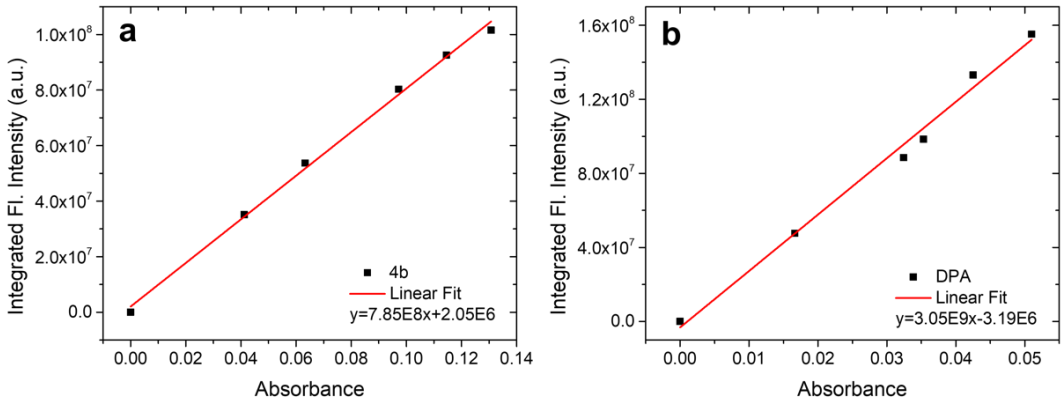

Figure 2.4. The absorbance was plotted against the integrated fluorescence intensity for the solvent and five different concentration samples for **4b** (a) and DPA (b). The data points were fit with a linear line to obtain the slope (m) for the calculation of the fluorescent quantum yield.

Once the quantum yield of the sample (Φ_{flx}) is calculated, it can be used to calculate the radiative lifetime (τ_{rad}),

$$\tau_{rad} = \frac{\tau_{fl}}{\Phi_{fl}}$$

using the experimentally determined fluorescence lifetime, τ_{fl} (section 2.2.5 below). Finally, using this result, the radiative rate can be calculated,

$$k_{rad} = \frac{1}{\tau_{rad}}$$

and then used for analysis of excited state dynamics.

2.2.5 Time-Resolved Photoluminescence (TRPL)

Time-resolved spectra and decays were recorded using a Hamamatsu C4334 Streakscope that provides spectral and temporal resolution to 2.5 nm and 15 ps. The sample was excited with 400 nm from a frequency doubled 800 nm output from a 1 kHz Coherent

Libra femtosecond Ti:sapphire laser. The emission was then collected by the streak camera in a front face configuration. All dilute solutions ($\approx 2 \cdot 10^{-5}\ M$) in chloroform, unless different solvent is specified, were purged with argon for 15 minutes.

Decays were plotted on a log scale for the phenyl compounds (**4a** and **6a**) in Figure 2.5, and the cage compounds (**4b** and **6b**) in Figure 2.6. A monoexponential fit (equation 2.2) was used to fit the decays in Figure 2.5 to analyze the radiative lifetime. For the cage compounds, there are two components in the decays, as seen in Figure 2.6. Therefore, a biexponential fit (equation 2.3) was used to analyze the two major lifetimes in each decay.

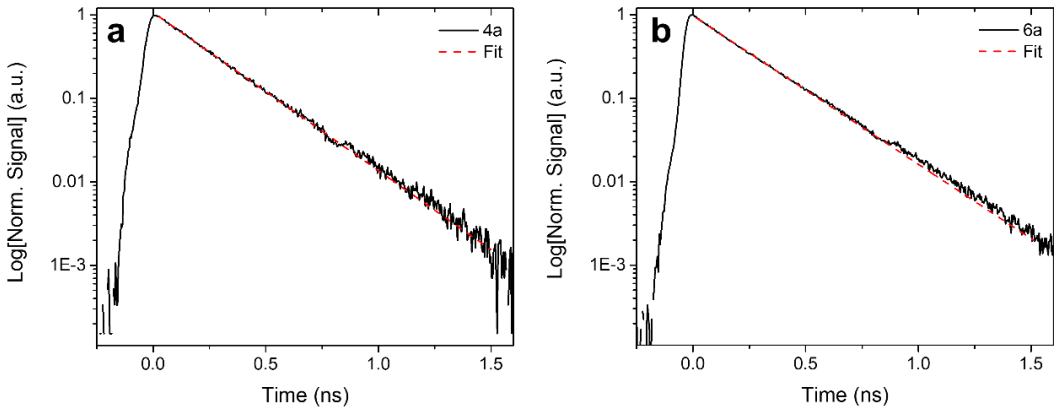

Figure 2.5. (a) Fluorescence decay over time of **4a** (black) with a monoexponential fit (red) fit to the decay to give a lifetime of 229 ps. (b) Fluorescence decay of **6a** (black) with a monoexponential fit (red) fit to the decay to give a lifetime of 244 ps. Both fluorescent decays were collected in a 2 ns window from 448-653 nm (**4a**) and 415-568 nm (**6a**).

$$y = A_1 e^{-\frac{x}{\tau_1}}$$

Equation 2.2. Monoexponential fitting function to obtain τ_1 modelled in fit (red) in figure 2.5.

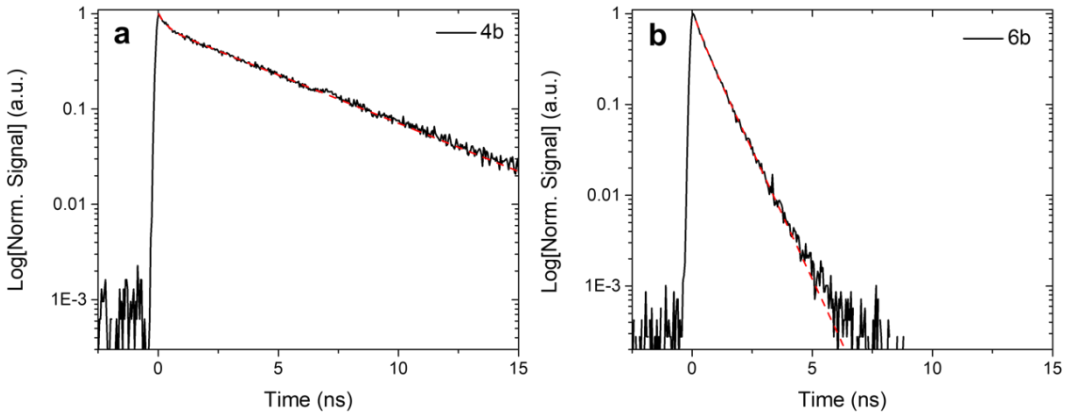

Figure 2.6. (a) Fluorescence decay over time of **4b** (black) with a biexponential fit (red) fit to the decay to give a lifetimes of 298 ps and 4.3 ns. (b) Fluorescence decay of **6b** (black) with a biexponential fit (red) fit to the decay to give lifetimes of 277 ps and 765 ps. Both fluorescent decays were collected in a 20 ns window from 476-510 nm.

$$y = A_1 e^{-\frac{x}{\tau_1}} + A_2 e^{-\frac{x}{\tau_2}}$$

Equation 2.3. Biexponential fitting function to obtain τ_1 and τ_2 modelled in fit (red) in Figure 2.5. The prefactors A_1 and A_2 are used to calculate the weight of each component ($\%\tau$).

2.2.6 Femtosecond Transient Absorption (fs-TA)

Fs-TA experiments were carried out using a 1 kHz Coherent Libra femtosecond Ti:sapphire laser. The 800 nm fundamental output beam of ≈ 2 W was first split with a beamsplitter so 70% of the power went to the TA line and 30% of the power went to a Quantronix OPA (not used in these experiments). The TA line was then split into the pump and the probe line at a second beamsplitter. About 90% was sent through a BBO crystal for frequency doubling, that resulted in a 400 nm pump line. The other 10% was used to make the white-light continuum probe. The path length of the pump and probe were routed to be equivalent, to ensure that time zero (temporal overlap of each beam) occurred on the

length of the delay stage. The pump and probe were then focused spatially and temporally through a 1 mm flow cell. After the sample cell, the probe beam was focused into an optical fiber coupled to an Ultrafast Systems UV-Vis CMOS spectrometer.

Pump Alignment: After the BBO crystal, the 400 nm pump is aligned through a chopper that is controlled with the UltrafastSystems software. Be sure that the entire pump beam fits through the open area and is not cut off by the chopper. Next, align the beam through a double-pass box mirror on the 1600 ps delay line. To do this, first take off the box mirror and align perfectly between the two iris's (one in front of and one behind delay stage). Put the box mirror back on the delay stage and align to the sample. Next, the pump should be aligned to the wall (≈ 3 meters away) to check for "walk off" of the beam. This ensures that the pump beam is not moving spatially during the entirety of the delay stage. Open the ΔA Spectrum on the UltrafastSystems software and see the position of the delay line on the right side of the screen. Scan from the front to the back of the stage a few times while closely watching the beam on the wall to ensure that it does not move from its original position. If it does not move, then pump alignment is done. If it does move, then the pump needs to be realigned through the box mirror to make sure that it is going straight through, and repeat checking for walk off on the wall. Repeat until the beam does not have any "walk off". This step is critical in receiving correct TA signal, as walk off of the pump beam can result in an apparent decay of the absorption signal.

Probe Alignment: The probe line is telescoped through a 3 mm sapphire plate to generate a white light continuum. The probe should be first optimized by finding the brightest output when finely adjusting the compression grating in the Ti:Sapph with the grating controller. Next, the probe should be optimized by eye by adjusting the power with the iris before the sapphire plate in combination with the angle of the sapphire crystal. A filamented rainbow should appear after the sapphire plate and then focus to a white beam. Next, the UltrafastSystems software is used to check the quality of the probe by clicking the probe spectrum icon. When optimized it should be from ≈450-750 nm, as seen in **Figure 2.7**. Note that some 800 nm fundamental will leak through the sapphire plate so be sure to reduce this with a hot mirror before the sapphire plate or neutral density filters after the sapphire plate.

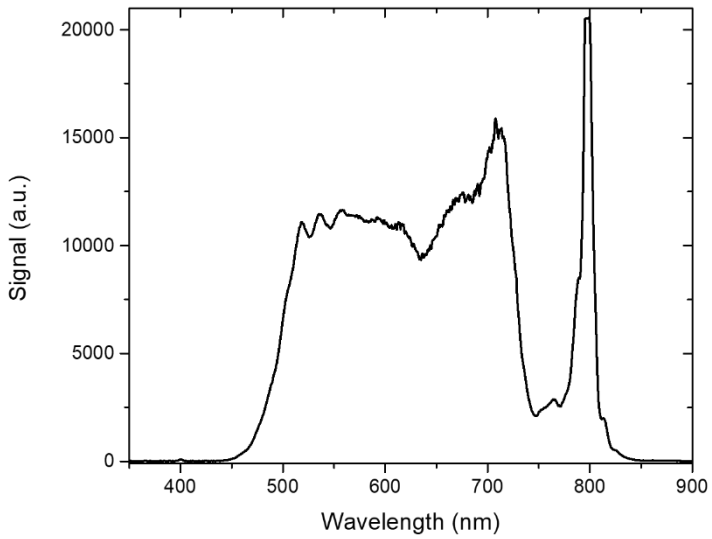

Figure 2.7. White light continuum probe spectrum generated from a sapphire plate.

If the spectrum is not present, then the beam is not likely coupled into the optical fiber. In this case, finely adjust the 3D stage where the probe is focused into the optical fiber until maximum signal is seen. Use neutral density filters to move the maximum signal between 10,000 and 20,000 counts. The probe spectrum will appear to be "jumpy," meaning the continuum is not very stable. To fix this, adjust the iris letting light into the telescope to the sapphire plate to optimize for a combination of the most stable signal and best square spectrum. These should all be very fine adjustments.

2.2.7 Optimization of fs-TA

Once the pump and probe are aligned, a laser dye should be used to maximize the overlap between the pump and probe at the sample. When using a 400 nm pump, Coumarin 540a can be used for optimization of signal before running any samples. Use Coumarin 540a mixed in methanol at a concentration that roughly results in 30-60% transmittance in a 1 mm path length cell. Then flow through the cell, with the solution flowing through at a constant rate, first making sure that the polymer tubes are compatible with the solvent used. Open the ultrafast systems software and look at the ΔA spectrum. The integration time should be set based on the level of noise in the spectrum. Move the stage back and forth to make sure that time zero occurs on the stage. At the front of the stage, the spectrum should be at the baseline and after time zero, there should be a large induced absorption, as seen in **Figure 2.8**. Zoom in time to find time zero and set it at the point just before the delta function grows into the spectrum. Now the fs-TA measurement will be temporally overlapped. To spatially overlap the pump and probe beams, look at the maximum signal

in time on the ΔA spectrum and finely tune the position of the pump in the x and y directions with the last oval mirror that directs the pump to the sample. Be sure not to touch any mirrors before the last one, or time zero will also change.

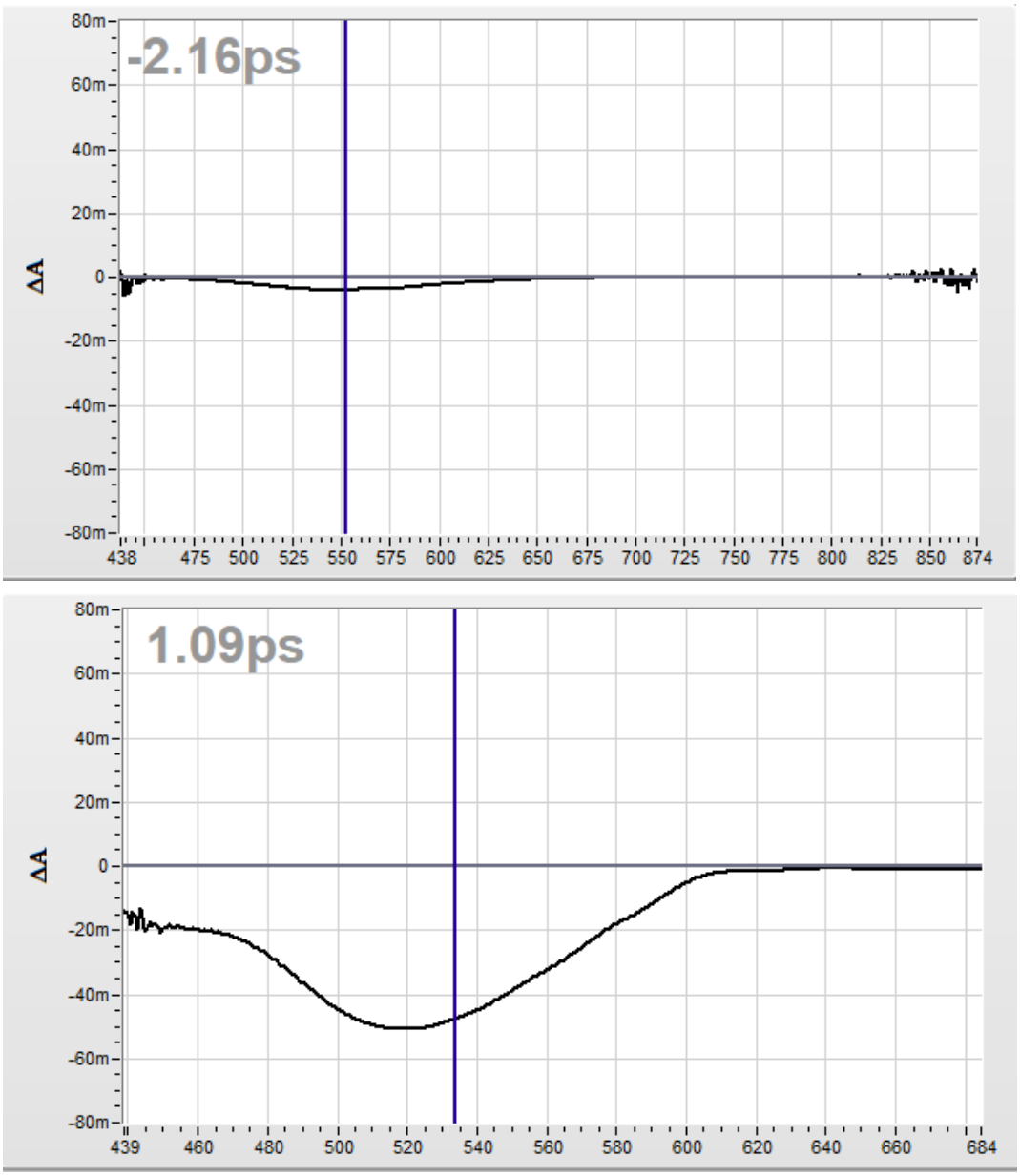

Figure 2.8. ΔA spectra (top) 2 ps before time 0 and (bottom) 1 ps after time 0 for Courmarin 540a in methanol.

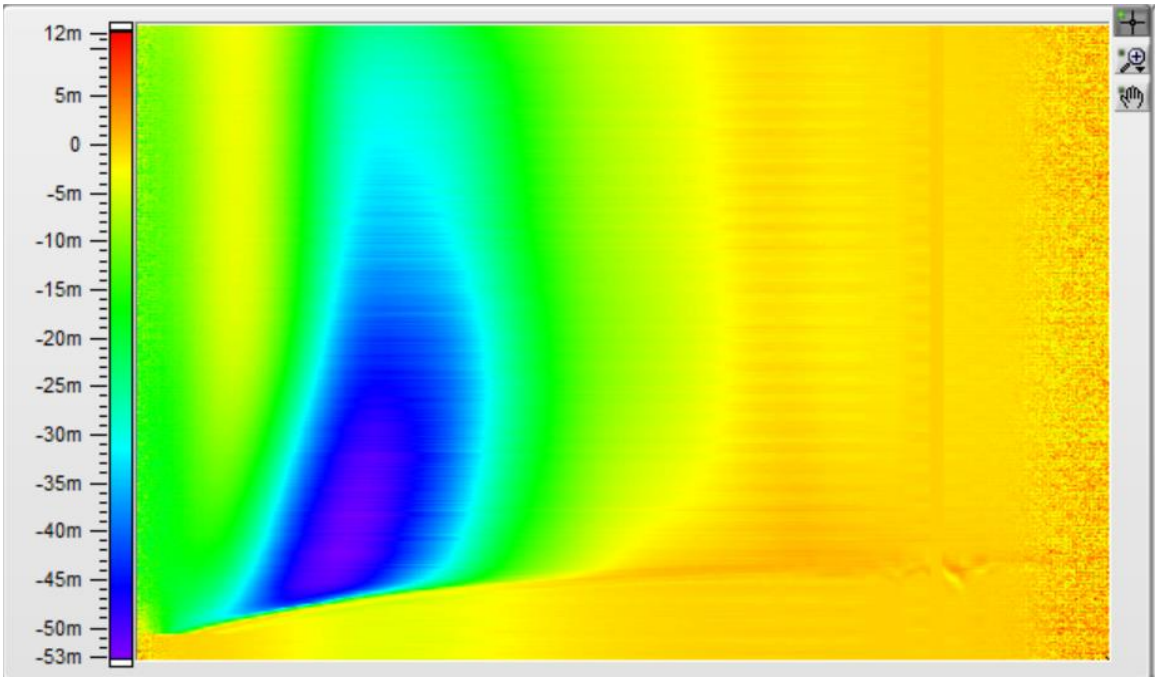

Figure 2.9. 3D surface for Courmarin 540a in methanol. The y-axis is in time from -200 – 1400 ps, the x-axis is wavelength from 450-850 nm, and the heat map shows intensity according to the legend. The uncorrected surface plot should appear similar to this after running the dye.

Data Collection: Next, set parameters for data collection and run a scan on Coumarin 540a. After collecting the dye data, run a solvent response scan using the same collection parameters. This must be done with all samples run on TA to ensure there are no solvent effects changing the kinetics. The 3D matrix should look like **Figure 2.9** for Coumarin 540a.

Data Workup: Surface Xplorer software can be used to analyze the data. First, do a background subtraction to delete all spectral noise before time 0. Then, do a chirp correction using the solvent response by applying the solvent response fit to the chirp

correction in the data set. Next, zoom into the 3D spectra in time to find time 0 and correct to the nearest femtosecond when the delta function first appears. After this, the time associated spectra and wavelength dependent kinetics can be analyzed and plotted.

Global Fitting: Finally, global fitting analysis can be done in Surface Xplorer to determine the major time components present in the spectra. Briefly, global fitting analysis uses a singular value decomposition (SVD) procedure in which a weighted least-squares fit provides the best estimate of the 3D TA matrix. The principle components in the TA matrix are reconstructed by generating the highest significant linearly independent set of eigenvectors. Each individual eigenvector has a reduced noise associated principle spectra with corresponding kinetics. After the SVD is performed, a global fit is used to fit the principle components with a sum of convoluted exponentials that results in spectral and kinetic traces at single wavelengths,

$$S(t) = e^{-(\frac{t-t_0}{t_p})^2} * \sum_i A_i e^{-(\frac{t-t_0}{t_i})}$$

Where an exponential prefactor (A_i) contains all of the lifetimes present in the global analysis and represents the significance of each time constant at each wavelength. The main spectral associated species are then represented with correlated kinetic lifetimes.[178]

2.3 Liquid-Vapor Actuation

2.3.1 Sample Preparation

The actuator design consists of an optically clear substrate connected to a cylinder that contains the working fluid. An image of this setup is seen in **Figure 2.10**. The Al plate (flyer) sits on top of the cylinder in contact with the liquid. The Al plate completely covers the liquid filled hole, creating a seal. The cylinder consists of 25 mm diameter cylindrical stainless steel (316L) with a 9 mm diameter hole through its center to contain liquid. The depth (D) of the cylinder could be varied from 0.5 mm to 20 mm. The transparent substrate was a 25 mm diameter, 3.2 mm thick disk of scratch- and UV-resistant cast acrylic polymethyl methacrylate (PMMA, Mcmaster Carr part #8528K34) were cut 3.2 mm thick. The stainless steel cylinder was affixed to the acrylic substrate with cyanoacrylate superglue (3M Scotch-Weld Instant Adhesive CA8) to create leak-proof seal. The Al flyer was a rectangular block with dimensions length=13 mm, width= 9 mm and height=1 mm with a mass of 0.94 g. For the metal dependence, the length and width of the stainless steel and copper were the same as Al (13 mm x 9 mm), but the height was changed so the flyer had equal mass to the aluminum plate. For the Al flyer mass dependence, the length and width of the flyer were held constant, and only the height was altered to change the mass of the plate.

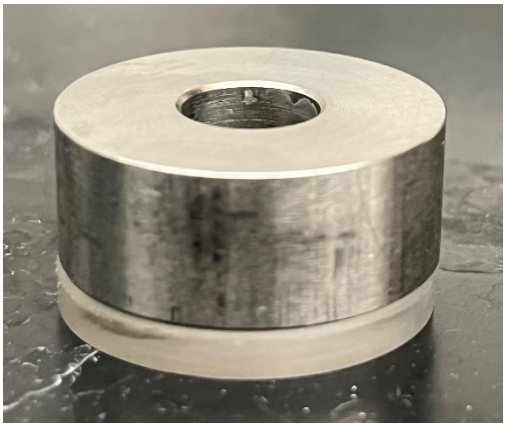

Figure 2.10. Image of a stainless-steel spacer (10 mm height) with a 9 mm hole through the center is glues to an acrylic substrate.

To fill the cylinder, liquid was slowly injected into the cylinder to avoid any bubbles. The Al piece was carefully positioned on top of the 9 mm hole through the center of the spacer making sure that the liquid underneath was in contact with the Al. The presence of an air pocket could be detected in the course of an experiment by the distinctive hollow popping sound that it made upon laser impact. For the alkane solvent dependence, four straight chain alkanes and one cycloalkane were used. 99+% n-pentane (C_5H_{12}, Thermo Scientific), ≥98% n-hexane for GCMS SupraSolv (C_6H_{14}, Millipore Sigma), 99% ACS grade cyclohexane (C_6H_{12}, Fisher Scientific), >97% n-octane (C_8H_{18}, TCI Chemical), and >99% n-decane ($C_{10}H_{22}$, TCI Chemical) were used as received. Deionized water was used for all of the H_2O trials. Since alcohols can dissolve the acrylic substrate, a mixture of 10% methanol (0.2 micron filtered Optima, Fisher Scientific) and 90% deionized water (H_2O/MeOH) was used to compare with pure H_2O. Ethylene glycol ($C_2H_6O_2$, Fisher Scientific >99% ACS grade) and glycerol ($C_3H_8O_3$, Fisher Scientific, >99% ACS grade) were also tested.

2.3.2 Single-Shot Laser Irradiation

A neodymium-doped yttrium aluminum garnet laser (Nd:YAG, Amplitude Surelite II-10) with single shot capability was aligned to fire single pulses upward through the optically clear acrylic substrate and liquid-filled cylinder where it hit the Al piece resting on top. This laser source generated 5 ns pulses at 1064 nm and 532 nm. The laser energy was recorded at the position of the Al plate on top of the cylinder before all experiments. The pulse energy was varied from 0.01 J to 0.45 J by adjusting the delay time of the laser Q-switch. With a measured laser spot diameter of 5.5 mm in a Gaussian profile, the energy fluences at the Al surface ranged from 0.1 J/cm^2 to 0.6 J/cm^2, all below the threshold for Al ablation.

After firing the laser, the Al plate trajectory was recorded using a Sony ZV-1 slow motion camera set to record at 760 frames per second. The trajectories were analyzed using ActionCam Movie Creator software from Sony. The height of the plate was quantified by referencing the plate position with respect to a ruler placed next to the setup. The plate consistently travelled in the vertical (y) direction with very little horizontal component, so we used a vertical trajectory model to solve for initial velocity of the aluminum plate, where height (y) with respect to time (t) is

$$y(t) = v_i t - \frac{1}{2} g t^2 \quad (1)$$

where v_i is the initial velocity and g is the acceleration of gravity due to Earth (9.8 m/s^2). The maximum height (y_{max}) occurs when velocity=0 and $t = {}^{v_i}/_{g}$, leading to

$$y_{max} = \frac{v_i^2}{2g} \quad (2)$$

or

$$v_i = \sqrt{2gy_{max}} \quad (3)$$

where y_{max} is the maximum height of the plate extracted from the slow-motion videos.

Chapter 3: Optimizing Pulsed-Laser Ablation Production of AlCl Molecules for Laser Cooling

3.1 Introduction

Laser cooling of atoms[179–183] has led to significant advances in fundamental physics, including the creation of Bose–Einstein condensates[36,37] and the demonstration of quantum phase transitions.[184] It also provides the basis for many precision tests of fundamental theories[185,186] and atomic clocks.[187] Extending laser cooling techniques to molecules could open up completely new directions of research, such as controlled chemical reactions,[39,188–192] quantum simulation of strongly interacting systems,[40,193] searches for physics beyond the Standard Model, and precision tests of fundamental theories.[194–206] The large electric dipole moments of polar molecules also make possible the creation of arrays of entangled molecular qubits that have been proposed as a novel platform for quantum computing.[31,207,208]

Given these potential applications, tremendous experimental effort has been put into the field in recent years, resulting in successful laser cooling and magneto-optical trapping of several diatomic species such as CaF,[47–49] SrF,[209] and YO.[50] Computational results and experimental studies suggest there exist other molecules with excellent properties for laser cooling and trapping,[51] including BaH,[210] CaOH,[211,212] YbF,[213] $CaOCH_3$,[214] YbOH,[199,215] and SrOH,[216] which have been laser cooled. Other proposed

diatomics for laser cooling are AlF,[217,218] BaF,[219,220] Cs_2,[221] MgF,[222] RaF,[223] TiO,[138] TlF,[224] and CH.[225] AlCl has been predicted to have excellent properties for laser cooling and trapping, including a large Franck–Condon factor of 99.88% and strong cycling.[52–54] High resolution spectroscopy experiments have recently confirmed these theoretical predictions, providing additional motivation to study this molecule.[65] One prerequisite for the study of AlCl is to have a general and versatile technique to produce a large number of molecules in the gas phase, especially for experiments that aim to create quantum degenerate molecular gases.

AlCl is an unstable molecule that must be created in situ. The production of gas phase AlCl for spectroscopic measurements has most commonly been accomplished by heating or putting a discharge through $AlCl_3$.[56–63] High temperature ovens have also been used to react Al vapor with separate sources of Cl atoms, including gases like Cl_2 and HCl,[62,226,227] as well as vaporized solids like $MgCl_2$, AgCl, and $AlCl_3$.[228–231] These high temperature sources produce translationally hot molecules and generate a heavy thermal load. In molecular laser cooling experiments that operate on a cryogenic buffer-gas cell, typically laser ablation is used to minimize the heat load. This approach was used to generate AlCl for the recent spectroscopy studies,[65] but there has been no systematic exploration of different conditions and precursors for optimal AlCl production. In optimizing the production of AlCl by laser ablation, several factors need to be taken into consideration for the solid target, including ease of preparation, safety, and the yield of gas phase AlCl. From previous work on thermal sources, the most obvious choice for a target would be neat $AlCl_3$, but this material presents several practical difficulties. It rapidly

decomposes in the presence of water vapor, producing toxic HCl gas and inert Al_2O_3. The rate of this decomposition depends on how the $AlCl_3$ is stored, and the details of sample loading (time of air exposure, relative humidity). Although it is straightforward to press $AlCl_3$ into a pellet, we found that these chemically unstable targets provided highly variable AlCl signals from run to run.

In an effort to generate more reproducible results, we explored mixtures of Al with a stable ionic compound source of chloride, denoted XCl_n, where X is the cation and n is the number of associated Cl anions. The laser ablation process involves several chemical steps, including rapid nonequilibrium heating of the solid target, volatilization of the precursors by breaking Al–Al and X–Cl bonds, diffusion, and finally Al–Cl bond formation. Any one of these steps could act as a bottleneck for AlCl production. In this work, our goal is to gain a better understanding of how this process works in order to optimize AlCl production for future laser cooling experiments. Both the chemical identity of XCl_n and the Al:XCl_n molar ratio are varied, and the yield of AlCl is monitored using absorption spectroscopy in a cryogenic buffer-gas beam cell.[64] The production of Al and K atoms was also monitored for Al:KCl mixtures.

We develop a simple framework to describe AlCl production in the limit of nonequilibrium reaction dynamics dominated by first-encounter events. With the additional assumption that Al atom production is partially suppressed by recondensation under the cryogenic conditions, this model provides a quantitative description of the data and reproduces the observed trend with different XCln precursors. The general conclusion is that using Al:XCl_n mixtures as ablation targets provides a robust and general strategy for

AlCl production. This preliminary investigation of AlCl formation in ablation plumes should help provide a guide for the development of new ablation precursors and their optimization. The ultimate goal is to develop convenient, high efficiency sources of metastable diatomic molecules that are amenable to cooling to nano-Kelvin temperatures.

3.2 Results

3.2.1 Experimental Measurements of AlCl, Al, and K

The ablation target consists of a pressed pellet of powdered Al and XCln precursors. For all cases, a robust, stable pellet was formed that could be cut and glued to the target plate. Several Cl sources were tested in addition to $AlCl_3$, including NaCl, KCl, $CaCl_2$ and $MgCl_2$. These chlorides are non-toxic and relatively stable. $MgCl_2$ and $CaCl_2$ can absorb water to make a hydrate, but this process is very slow when the $MgCl_2$ or $CaCl_2$ is pelletized with Al, with less than a 0.03% mass increase after 24 hours of exposure to ambient air. Of the other low molecular weight chlorides, LiCl is very hygroscopic and visibly changes appearance after less than 1 minute of air exposure, so it was not tested. $BeCl_2$ is toxic and was also omitted. The properties of the alkali and alkaline earth chlorides are summarized in **Table 3.1**. The variation in X–Cl ionic bond strengths provides a way to assess whether the initial dissociation of this bond is a limiting factor in AlCl production.

	MW (g/mol)	ρ (g/cm^3)	ρ (mol/cm^3)	D^0 (kJ/mol)
Al	26.982	2.70	-	-
KCl	74.551	1.988	0.0267	433.0
NaCl	58.443	2.17	0.0371	412.1
$CaCl_2$	110.984	2.15	0.0387	409 (Ca-Cl)
$MgCl_2$	95.211	2.325	0.0488	312 (Mg-Cl)
$AlCl_3$	133.34	2.48	0.0558	502 (Al-Cl)

Table 3.1. Aluminum and XCl_n sources in order of increasing chloride molar density. The molecular weights (MW), solid-state densities (ρ), and bond dissociation energies (D^0) are also shown. D^0 values are shown for the diatomic bonds as denoted (X–Cl).[232]

The apparatus for the production and measurement of the AlCl has been described in detail in a previous paper.[65] Briefly, a high-energy 14 mJ, 5 ns at 532 nm laser pulse is focused on the target in a vacuum chamber. The resulting ablation plume is swept through the absorption cell by a 4 K stream of He gas. The absorption at the $v = 0, J = 1 \longrightarrow v' = 0, J' = 1$ transition located at 1146 THz (261.5 nm) gives rise to the most intense absorption and is monitored by an ultraviolet probe laser.

The absorption is time-dependent, as shown in **Figure 3.1**, peaking shortly after the ablation laser shot at 10 ms and then decaying away on a timescale of ≈5 ms. **Figure 3.2** shows images of a Al:KCl target before and after an absorption run. The grey color of the target in Figure 3.3 can be attributed to the Al powder with its oxide coating. The KCl does not absorb in the visible region and makes a transparent glassy solid when compressed.

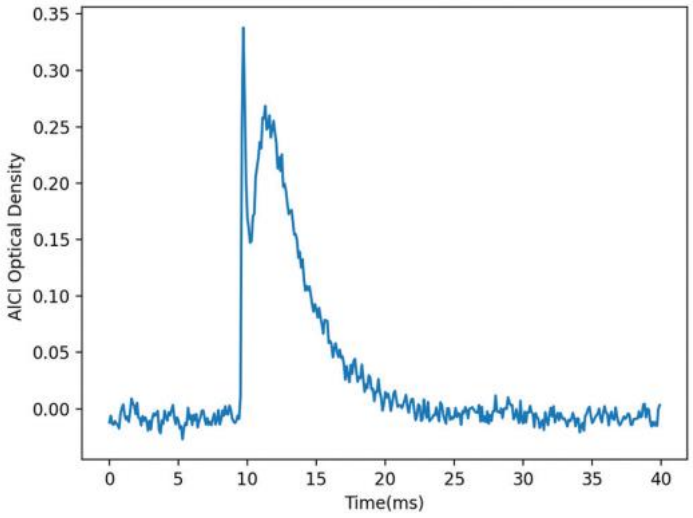

Figure 3.1. Sample absorption time trace at the peak of the $Al^{35}Cl$ Q branch. We note that the initial spike at t = 10 ms is an artifact from the ablation laser scatter on the absorption photodiode.

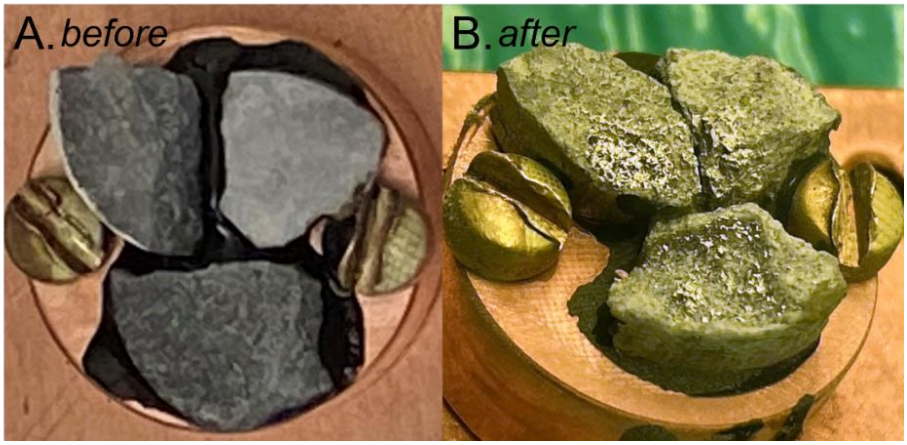

Figure 3.2. (A) Typical sample targets of Al:KCl mixtures before ablation. Targets vary in shade of grey due to the amount of aluminum in Al:KCl molar ratio, consisting of pure KCl (top right), 1:3 (top left), and 1:10 (bottom). (B) Typical target appearance after ablation to show the shiny aluminum coating on the sample after ablation. The Al:KCl ratios are 3:1 (top right), 1:1 (top left), and 1:3 (bottom).

After ablation, the target in **Figure 3.2B** shows the expected loss of mass, but this loss is not uniform across the pellet. This corrugated landscape is probably due to local concentration inhomogeneities in the pellet, as well as morphology changes that occur due

to fracture during the ablation process. The most notable change is the appearance of a bright, reflective layer of Al metal in the ablated regions. The presence of this coating suggests Al atoms are being efficiently ablated and recondensing onto the target surface as a metallic layer. The effect of ablation on the KCl is less obvious, but it is also ablated as deduced from the large loss of material from the pellet. From **Figure 3.2**, one potential concern is that debris from one target could contaminate a neighboring target. However, this contamination would only affect the surface, while the majority of ablated material originates from the interior of the pellet. Extra contributions by K atoms in the absorption signal of neighboring low KCl pellets were not detected, further indicating that cross-contamination is negligible.

To determine how the AlCl production depends on the composition of the ablation target, the Al:KCl combination was used with varying amounts of KCl and Al powders. The amounts of AlCl, K and Al produced from different mixing ratios were monitored in the absorption chamber. The experimental results are shown in **Figure 3.3** as a function of the Al:Cl molar ratio, R_{mol}. Also shown in **Figure 3.3** are simulated data generated by two chemical models that are described in the next section.

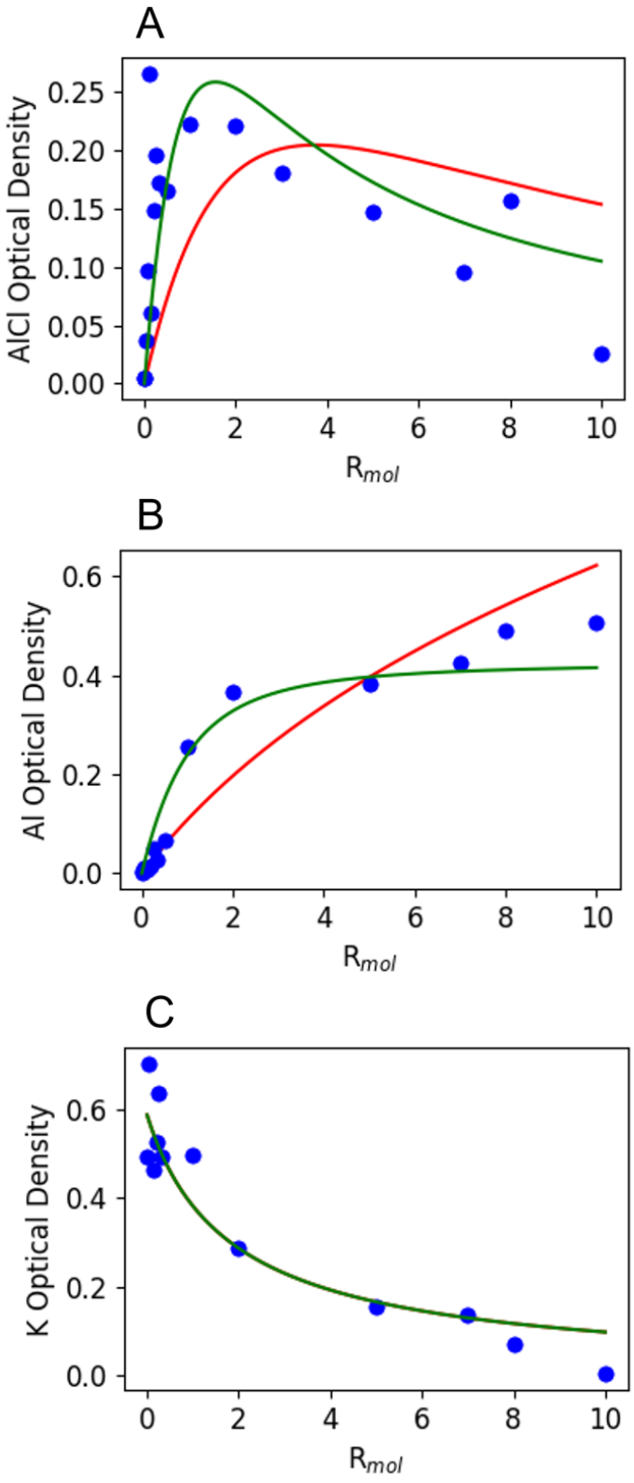

Figure 3.3. Model A (red line) and Model A' (green line) are overlaid with experimental data (blue dots) AlCl (A), Al (B), and K (C) showing a qualitatively better fit from Model A' . Model A and A' predict the same fit for K optical density in C.

3.2.2 Modelling AlCl Formation

Given the highly dynamic nature of the ablation process followed by rapid cooling in the He gas, it is doubtful that the system ever reaches chemical equilibrium. The reaction

$$Al + Cl \longrightarrow AlCl \quad (1)$$

is thermodynamically favored with $\Delta G = -75\ kJ\ mol^{-1}$,[233] but at low temperatures the reaction

$$3AlCl \rightarrow 2Al + AlCl_3 \quad (2)$$

is even more favored.[234–236] Extrapolating from previous high temperature results,[235] we can estimate $K_{eq} = 10^{1000}$ for reaction (2) at 10 K, which implies that no AlCl should be present at this temperature if the system is at equilibrium. But the disproportionation reaction (2) has an activation barrier and can be suppressed for temperatures below about 150 K, as shown in earlier work on cryogenic solids.[237] So the rapid cooling of the ablation plume should be able to quench reaction (2) and preserve the thermodynamically unstable AlCl. Given that reaction (1) will be occurring under conditions of rapid cooling, AlCl formation will be determined by first-encounter collisions of Al and Cl atoms early in the process, followed by an extended period during which the excess collision energy present in the AlCl molecule is carried away by collisions with the He atoms. Thus a reasonably high He gas density is expected to be necessary for preserving the newly formed AlCl.[64,238]

To model the R_{mol} data, we take as the starting point the assumption that the AlCl concentration [AlCl] is proportional to the product of the initial gas phase concentrations of Al and Cl atoms produced by the ablation pulse, $[Al]_0$ and $[Cl]_0$ respectively,

$$[AlCl] = K[Al]_0[Cl]_0 \quad (3)$$

Note that the form of eqn (3) resembles that expected for a system at equilibrium, where $K = K_{eq}$, the equilibrium constant. But here eqn (3) is justified by different physical considerations. From a probabilistic standpoint, the collision probability is just proportional to the Al and Cl densities. Alternatively, if we consider the bimolecular kinetic equation,

$$\frac{\partial[AlCl]}{\partial t} = k[Al][Cl] \quad (4)$$

where lower-case k is the rate constant, for small time intervals dt we also obtain eqn (3) with K = kdt. These arguments justify the use of eqn (3) as the starting point for our calculations.

3.2.3 Model A: free atom production.

We assume that the ablation laser vaporizes a volume V_0, which puts a limit on the amount of Al and Cl that can be vaporized because

$$\frac{m_{Al}}{\rho_{Al}} + \frac{m_{XCl_n}}{\rho_{XCl_n}} = \frac{MW_{Al}}{\rho_{Al}} N_{Al} + \frac{MW_{XCl_n}}{\rho_{XCl_n}} N_{XCl_n} = V_0 \quad (5)$$

where m_{Al} and m_{XCln} are the masses of Al and XCl_n in the ablation volume V_0. The molecular weights of the compounds are MW_{Al} and MW_{XCln}; ρ_{Al}, ρ_{XCln} are the solid-state densities of Al and XCl_n and N_{Al} and N_{XCln} are the number of moles of atomic Al, and molecular XCl_n in V_0. Eqn (5) places a constraint on the number of moles of Cl available

to bond with a given number of moles of Al. We define the molar ratio of Al:Cl atoms (R_{mol}) in the solid to be

$$R_{mol} = \frac{1}{n}\frac{N_{Al}}{N_{XCl_n}}. \tag{6}$$

If we assume that the moles of atoms in the gas phase are directly proportional to the number of moles in the solid, i.e. $N_{Al}^{gas} = \alpha N_{Al}$ and $N_{Cl}^{gas} = \beta n N_{XCl_n}$ where α and β are the ablation efficiencies and the n factor takes into account that we get n Cl atoms per molecule of XCl_n. Eqn (3) then becomes

$$[AlCl] = K[Al]_0[Cl]_0 = K\left(\frac{N_{Al}^{gas}}{V_{gas}}\right)\left(\frac{N_{Cl}^{gas}}{V_{gas}}\right) = K\alpha\beta\left(\frac{N_{Al}}{V_{gas}}\right)\left(\frac{nN_{XCl_n}}{V_{gas}}\right) \tag{7}$$

Using eqn (5) and (6), we obtain an expression for [AlCl], N_{Al}^{gas} and N_{Cl}^{gas} in terms of R_{mol} and V_0 with only α, β, and K as adjustable parameters:

$$N_{Al}^{gas} = nV_0\left(\frac{\alpha}{\frac{MW_{XCl_n}}{\rho_{XCl_n}} + \frac{MW_{Al}}{\rho_{Al}} nR_{mol}}\right)R_{mol} \tag{8}$$

$$N_{Cl}^{gas} = nV_0\left(\frac{\beta}{\frac{MW_{XCl_n}}{\rho_{XCl_n}} + \frac{MW_{Al}}{\rho_{Al}} nR_{mol}}\right) \tag{9}$$

$$[AlCl] = \gamma\left(\frac{n}{\frac{MW_{XCl_n}}{\rho_{XCl_n}} + \frac{MW_{Al}}{\rho_{Al}} nR_{mol}}\right)^2 R_{mol} \tag{10}$$

Where $\gamma = K\alpha\beta\left(\frac{V_0}{V_{gas}}\right)^2$. Eqn (10) gives the full dependence of the AlCl concentration on R_{mol}. We can take the derivative of eqn (10) to find the R_{mol} value that gives the maximum [AlCl],

$$R_{mol}^{max} = \frac{\frac{MW_{XCl_n}}{\rho_{XCl_n}}}{n\frac{MW_{Al}}{\rho_{Al}}} \tag{11}$$

The maximum [AlCl] is found to be

$$[AlCl]_{max} = \frac{\gamma}{4}\frac{n\rho_{Al}\cdot\rho_{XCl_n}}{MW_{Al}\cdot MW_{XCl_n}} \tag{12}$$

Eqn (11) shows that R_{mol}^{max} depends only on the relative molar densities of Al and Cl atoms in the laser focal volume. Eqn (8)–(10) can be independently scaled to obtain agreement with the experimental data. Since the scaling factors may be different, this fitting does not permit the absolute determination of the efficiencies α and β.

3.2.4 Model A': Al recondensation.

The observation in **Figure 3.2** that metallic Al is plating out on the target suggests that the concentration of Al atoms above the target may be limited by recombination. The relatively high boiling point of Al (2519°C)[232] versus KCl (1407°C)[239] suggests that the recondensation of Al into its liquid form will occur preferentially. If Al atoms recondense before they can react with the Cl atoms, this will limit the Al concentration in the gas phase.

We can take this possibility into account by limiting the amount of Al in the gas phase using the equation

$$N_{gas}^{Al} = \frac{V_0 \alpha}{\kappa}\left(1 - e^{-\kappa N_{Al}/V_0}\right), \tag{13}$$

κ is a free parameter that limits the amount of Al that can react with Cl atoms. Eqn (13) assumes that the local density of Al in the solid, $\frac{N_{Al}}{V_0}$, promotes recondensation of the Al from the gas phase. This expression reduces to $N_{gas}^{Al} = \alpha N_{Al}$ in the limit of small κ or N_{Al}, but predicts that N_{gas}^{Al} saturates at a value of $\frac{V_0 \alpha}{\kappa}$ as N_{Al} increases. This expression leads to a new equation for the concentration of AlCl

$$[AlCl] = \gamma \frac{n}{\kappa} \frac{1}{\frac{MW_{XCl_n}}{\rho_{XCl_n}} + \frac{MW_{Al}}{\rho_{Al}} n R_{mol}} \times \left[1 - exp\left[\frac{-\kappa n R_{mol}}{\frac{MW_{XCl_n}}{\rho_{XCl_n}} + \frac{MW_{Al}}{\rho_{Al}} n R_{mol}}\right]\right] \tag{14}$$

To compare this result to eqn (11), the maximum of eqn (14) can only be determined numerically. Physically, we expect the maximum of the [AlCl] curve to shift to lower R_{mol} values, since increasing N_{Al} only limits the available Cl atoms after saturation. This is exactly what is observed in numerical calculations (**Figure 3.4**).

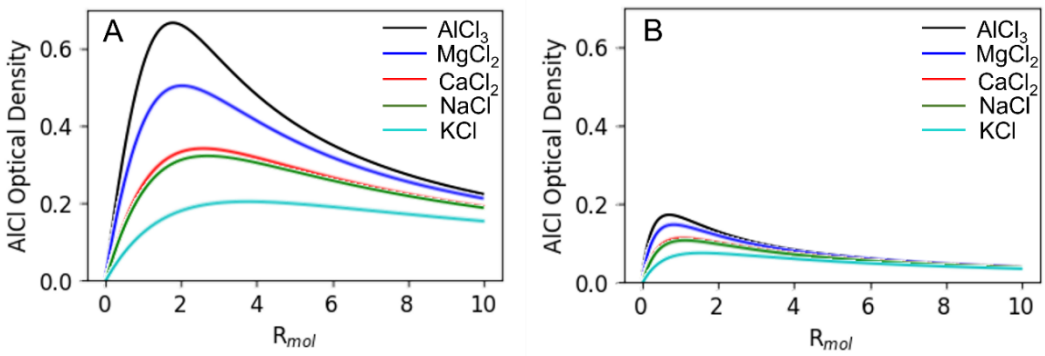

Figure 3.4. Simulated R_{mol} curves for different XCl_n sources from Model A (A) and Model A' (B). With a fixed scaling factor (γ), the optical density of each source in Model A is roughly 3 times larger than Model A' due to the aluminum recondensation.

3.3 Comparison of model to results

In **Figure 3.3**, we overlay the results of Models A and A' with the Al:KCl data. The prefactors in eqn (10) and eqn (14) are scaled to match the experimental data. Model A' does a better job of reproducing the data than Model A, which assumes no aluminum saturation after gas-phase collisions in the ablation plume. Model A predicts a maximum signal for R_{mol} = 3.75, while Model A' predicts a maximum [AlCl] at R_{mol} = 1.55, with κ = 53.2 $cm^3\ mol^{-1}$. Both Model A and Model A' predict the same trend in K signal, as shown in **Figure 3.3C**; while Model A' better predicts the trend in aluminum signal due to recondensation of aluminum after ablation, as shown in **Figure 3.3B**. Another advantage of Model A' is that it predicts a sharper drop off in the AlCl concentration for larger R_{mol} values. The γ prefactor required to match the [AlCl] data in **Figure 3.3A** is 2.8 times larger in Model A' than Model A. This corresponds to roughly three times lower [AlCl] in Model A' than Model A for a fixed γ prefactor. Based on this trend, we estimate that the AlCl

concentration is reduced by a factor of three due to recondensation of aluminum onto the surface of the target.

We next turn to the comparative study of different Cl atom sources. **Figure 3.5** compares the raw AlCl signals obtained for pure $AlCl_3$ and mixtures with NaCl, KCl, $MgCl_2$, and $CaCl_2$ with $R_{mol} = 0.25$. For this comparison, we used the best signal obtained after testing multiple $AlCl_3$ pellets, some of which produced no signal at all. The Al:XCl_n mixtures, on the other hand, provided much more reproducible signal levels. We observed only about a factor of two variation in the yield for these very different chemical mixtures. This result was robust with respect to the method used to extract the average absorption from the time-dependent traces in **Figure 3.5**, as seen in **Figure 3.6**.

Figure 3.6 provides a relative comparison of the experimental and calculated signals using models A and A'. The XCl_n species are ordered from low to high Cl molar density, as given in Table 3.1. The general trends for all three models are very similar. Both models predict a relatively weak dependence on the identity of X, as observed. The AlCl yield is not correlated with variations in the X–Cl bond strength (**Table 3.1**), suggesting that the details of the chemical bonding in the XCl_n precursor are not vital. Instead, the critical quantity for AlCl production appears to be the molar density of Cl atoms in the solid, ρ_{Cl}. This can be seen most clearly when the calculated [AlCl] signal is plotted for each XCl_n precursor at a fixed R_{mol} value. This plot, shown in **Figure 3.7A** for models A and A', is linear and has the same slope for both models. It should be noted that each XCl_n source can have a different R_{mol}^{max}, so we also evaluated the maximum [AlCl] signal for each individual XCl_n source. The trend with ρ_{Cl} is the same as in **Figure 3.7A**, although

not quite as linear as for the fixed R_{mol} plot. In fact, this variation can be predicted from eqn (12) and the deviations from linearity are due to changes in the MW_{XCln} denominator. The most important conclusion is that variations between the different chlorides are almost entirely due to differences in Cl density in the solid.

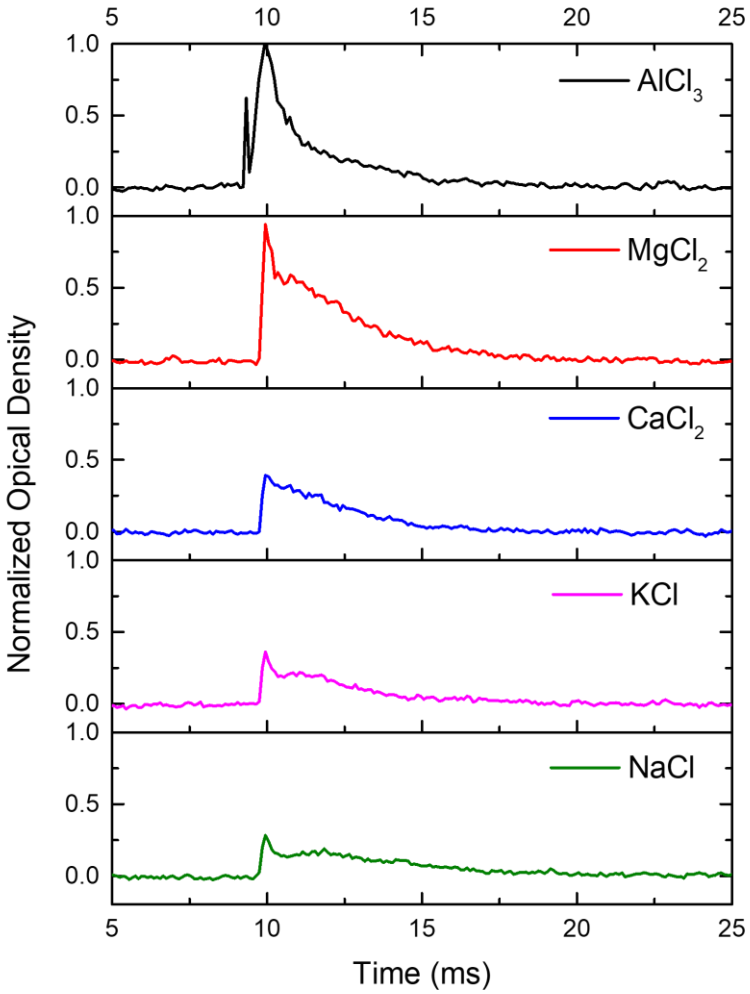

Figure 3.5. AlCl absorption after ablation of each chloride precursor at R_{mol} = 0.25. Each spectra is normalized to the $AlCl_3$ optical density to show the decrease in signal in each chloride source from top to bottom.

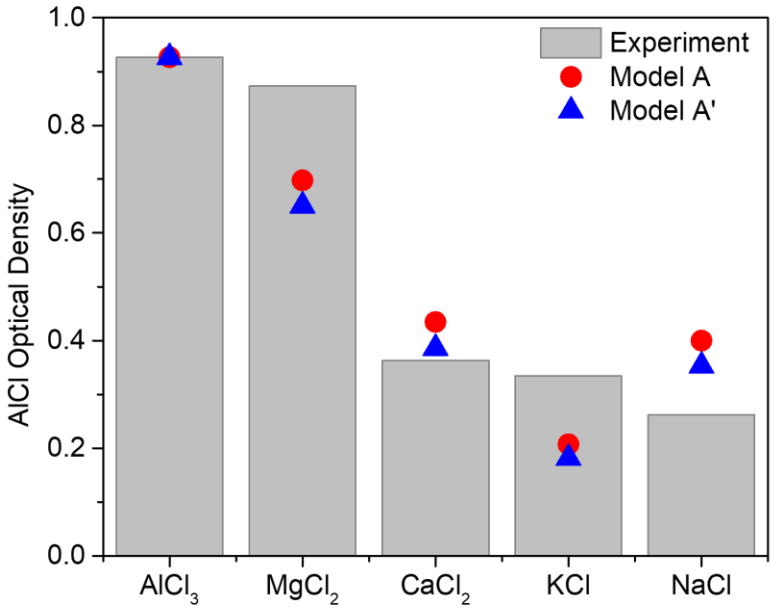

Figure 3.6. Theory is compared to the experimental optical density signal from each chloride source at $R_{mol} = 0.25$. Models A and A' are normalized to the $AlCl_3$ optical density.

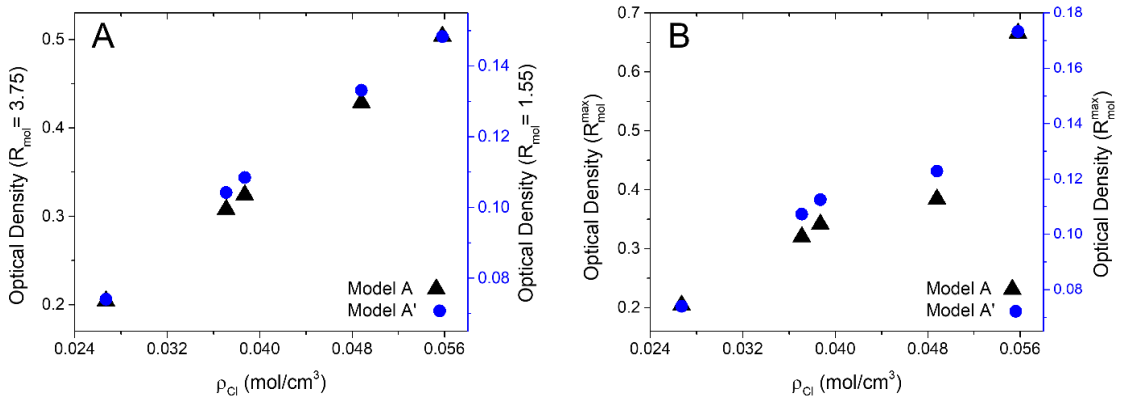

Figure 3.7. The chlorine molar density (ρ_{Cl}) for each XCl_n source from Table 3.1 is plotted against the optical density of that XCl_n source from Model A and Model A'. (A) The optical density for each XCl_n source is taken at the R_{mol}^{max} of KCl from each Model that is reported in Table 3.2. (B) The optical density for each XCl_n source is taken at its individual R_{mol}^{max}, from Figure 3.5. Both A and B show a linear dependence of AlCl concentration on ρ_{Cl}.

	Model A	Model A'
	R_{mol}^{max}	R_{mol}^{max}
KCl	3.75	1.55
NaCl	2.69	1.11
$CaCl_2$	2.58	1.07
$MgCl_2$	2.39	0.99
$AlCl_3$	1.79	0.74

Table 3.2. The R_{mol}^{max} found for each XCl_n source from Model A and Model A'. These values are used to plot against the ρ_{Cl} in Figure 3.8B.

3.4 Discussion

Laser ablation of solid targets is an extremely complicated process, involving multiple processes like thermal melting, phase explosion, and ionization.[240] The laser fluences used in this experiment are well above the phase explosion[241–243] and plasma thresholds[244] for Al, suggesting that many different chemical species can be generated in the plume above the target. Once the precursors are in the gas phase, modeling the detailed chemistry would require measuring densities, diffusion coefficients, and reaction rate constants for these species, a daunting task. An important result of this paper is that relatively simple models can capture the main features of the AlCl production by considering only the dynamics of the Al and Cl atoms after they are placed into the gas phase. The details of how they got there do not affect the model, as long as the ablation efficiencies are independent of R_{mol}. This can be rationalized by assuming that the ablation conditions result in such high temperatures that essentially all solid-state bonding is lost, leading to free atoms whose reaction to form AlCl is entirely determined by the initial concentrations and collision rate.

The fact that the first-encounter models do a good job of reproducing the [AlCl] curves is not surprising because the atoms are rapidly cooled as they react to form AlCl. If the cooling process freezes out the initially formed AlCl and prevents subsequent high energy collisions that allow the molecules to react further, for example dissociating back into Al + Cl or by adding another Cl to make $AlCl_2$, then the mixture will not reach equilibrium. At the measured temperature of 8.5 K, the formation of $AlCl_3$ is overwhelmingly favored, so the fact that AlCl is observed at all is further evidence that the cryogenic buffer gas beam source does not allow the gas mixture to reach equilibrium. In other words, AlCl production is kinetically controlled under these rapid cooling conditions.

Having developed a physical model that does a reasonable job of quantitatively reproducing the AlCl production data, we are now in a position to draw some conclusions about the production of cold AlCl by laser ablation. The first conclusion, that Cl atom density in the XCl_n precursor is a critical parameter in determining AlCl yield, provides practical guidance for the choice of precursor. In principle, $AlCl_3$ provides the highest yield, but as discussed above its toxicity and instability make it challenging to work with. Given that Al:$MgCl_2$ provides a similar signal level, and since there is only a modest (roughly a factor of 2) variation between the different chlorides we explored, it is not clear that the added inconvenience and hazard of $AlCl_3$ are worth the small signal gains. On the other hand, it may be that molecules with additional bonded Cls could drive the yield even higher. For example, hexachloroethane is a solid at room temperature, although it is much more difficult to handle than the salts used in this work. Finally, we should emphasize that the physical basis of our model is very general and should be applicable to other halides.

We suspect that identifying precursors with high solid-state halide densities will be an important consideration for the production of metal halide diatomics using laser ablation from mixtures.

In addition to the choice of Cl source, other experimental parameters can be tuned to improve AlCl production. One obvious step would be to increase the spot size and thus V_0, while keeping the heat load on the cryogenic system manageable. Since [AlCl] will scale as V_0^2 (eqn (10)), this provides a straightforward path to more signal per shot, albeit at the expense of using up the pellet more quickly and increasing the heat load on the cryogenic cell. Similarly, increasing the ablation efficiencies α and β (which were not directly measured in this paper) would also increase the production of AlCl. To compare the measured Al density (1.2×10^9 atoms per cm^3) and the maximum Al density based on the estimated ablation volume, we assume our ablation crater to be cone-shaped, and calculate the volume of the ablation cone estimating a crater depth of 6 μm[245] and our known ablation laser spot size of 80 μm.

$$V = \frac{1}{3}\left[\frac{1}{2}\pi r^2\right]h$$

The resulting volume of sample ablated is $5.03 \cdot 10^{-9}$ cm^3. Then we can use this volume and stoichiometrically convert aluminum density to moles of aluminum in the gas phase after ablation,

$$2.70\ {}^{g}/_{cm^3} \times 5.03 \cdot 10^{-9}\ cm^3 \div 26.98\ {}^{g}/_{mol} \times 6.022 \cdot 10^{23}\ {}^{}/_{mol}$$

to get $3.03 \cdot 10^{14}$ atoms. We can then use our known volume of our cell (28 cm^3) to calculate the maximum Al density after ablation,

$$\frac{3.03 \cdot 10^{14}\ atoms}{28\ cm^3}$$

resulting in the maximum Al density in the ablation volume to be 1.1×10^{13} atoms per cm^3. This allows a rough estimate of α to be on the order of 10^{-4}. Modifying the ablation conditions might enhance efficiencies. For example, most researchers use ultraviolet excimer laser sources to ablate alkali halides,[246–249] although infrared lasers have also been used,[250] so it is possible that shifting to shorter wavelengths would produce more Cl atoms. Alternatively, if we assume that the Al component is responsible for most of the laser absorption, then smaller Al and XCl_n particles in combination with more uniform mixing might also improve heat transfer to the XCl_n and accelerate its solid-to-gas transition. We could also consider ways to avoid the Al saturation behavior that is described by Model A'. Changes in the rate of cooling gas flow or surface geometry might inhibit Al atom recombination, although this is somewhat speculative.

Finally, it is important to point out that ablation of an Al:XCl_n mixture will always be limited by the constraint of eqn (5). Because all the Al and Cl atoms must be packed into a fixed volume V_0, increasing N_{Al} requires decreasing N_{Cl} and vice versa. To decouple these quantities requires separate Al and Cl sources. Recent work has shown that using a gas source for the halide, for example SF_6, can successfully generate metal halides like AlF.[251] To produce a source of Cl atoms, Cl_2, HCl or possibly methanochlorides like CCl_4, $CHCl_3$ and CH_2Cl_2 would be reasonable candidates. There is a previous report of AlCl

being produced by ablation of an Al rod exposed to Cl_2 gas,[252] but its characteristics were not described in detail. These potential Cl sources are corrosive and/or toxic, so the introduction of these gases into a vacuum chamber would add experimental challenges. But they are also chemically stable and easy to put in the gas phase, so they could result in much higher AlCl production if all the solid Al could be vaporized and reacted.

3.5 Conclusions

This work has demonstrated that pulsed laser ablation of Al:XCln mixtures provides a robust and reliable source of cold AlCl molecules. Stable, non-toxic precursors can be used instead of $AlCl_3$, the most commonly used precursor in previous studies. The reason that the alkali halide mixtures are relatively insensitive to the chemical nature of the precursor is that high intensity laser ablation provides enough excess energy to efficiently dissociate the Cl salt into its atomic constituents. A simple model that assumes AlCl formation is mainly determined by the initial Al + Cl → AlCl encounters can quantitatively capture trends in the AlCl production as a function of precursor composition and Al:XCl_n mixing ratio. The most important attribute of the solid XCl_n source is a high Cl atom density, a conclusion that may be generalizable to the production of other heteronuclear diatomics as well. More powerful lasers, improved ablation of the Al component, and decoupling the Al and Cl sources are all promising future directions for producing a large numbers of cold AlCl molecules. The work in this paper represents a first step in understanding the chemical mechanisms of laser ablation sources for producing AlCl and will hopefully provide guidance for their future development and optimization.

Chapter 4: Chemical Tuning of Exciton versus Charge-Transfer Excited States in Conformationally Restricted Arylene Cages

4.1. Introduction

The properties of organic electronic materials are determined by interactions between their conjugated subunits, for example, molecules in a crystal or polymer repeat units in an amorphous film.[253] One major challenge in this field lies in understanding and controlling these interactions, which can give rise to new emergent properties of the assembly. For example, when multiple organic chromophores interact, new electronic states that support delocalized excitons or separated electron−hole pairs can arise due to dipole−dipole and electron transfer interactions. In bulk solid-state samples, disorder and the large number of interacting molecules make it challenging to achieve a first-principles understanding of these new states. The complexity of the solid-state has motivated the study of smaller systems that can be purified and studied in isolation, for example, in dilute solution. Examples of such conjugated assemblies include donor-bridge-acceptor molecules and covalent chromophore assemblies like bichromophores and dendrimers.[77,254–264] In these supermolecules, covalent linker groups define both the number and connectivity of the interacting conjugated subunits.

The ability to synthesize discrete multiunit assemblies of conjugated molecules unlocks the ability to study complicated multibody phenomena like singlet fission[74,76,265–

[270] with a high level of experimental and computational sophistication. However, conformational flexibility in these covalent assemblies can lead to multiple configurations that have different subunit interactions and thus different electronic states and dynamics. In many cases, the conformational freedom of these covalent assemblies complicates their interpretation as structurally well-defined model systems.[100,271–274] A second problem concerns the role played by the covalent linker group in the electronic structure and dynamics. Although it is most convenient to assume that the linker is inert, there now exists a large body of work showing that it can play an important role in facilitating charge and energy transfer.[275–284] Given these complications, it is desirable to design a covalent multichromophore architecture that (1) provides additional limits on the conformational freedom of the constituent chromophores and (2) allows a modular approach to vary the chemical structure of the linker group and systematically explore its role in determining the electronic properties of the assembly.

In this work, we utilize a novel cage architecture for creating assemblies of conjugated organic chromophores. Meta-substituted aromatic caps serve as the covalent linking groups that attach to both top and bottom of the conjugated subunit. This strategy enables improved control of both molecular spacing and orientation because it provides two points of attachment for each conjugated subunit, bringing the assembly closer to crystalline order. Furthermore, the capping group acts as a constant structural element while providing chemical tunability that can be used to actively modify the electronic

structure of the assembly. To illustrate this strategy, **Figure 4.1** presents two possible implementations of the cage structures with capping units that can support either neutral exciton or CT states.

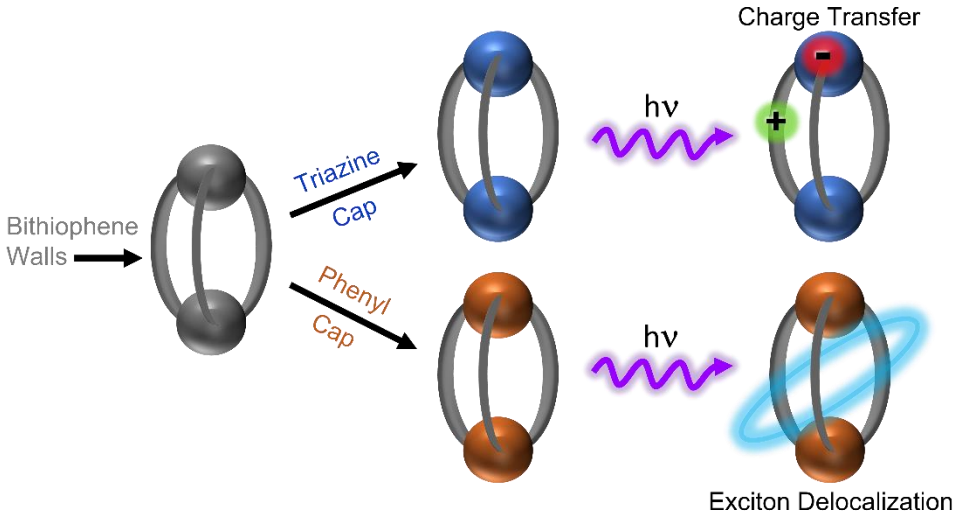

Figure 4.1. Schematic of capped bithiophene cage. Dependent on the capping unit used to lock the bithiophenes into the cage conformation, it can undergo charge transfer or exciton delocalization.

To demonstrate the capabilities of the architecture shown in **Figure 4.1**, in this paper, we study the properties of a bithiophene trimer built as a cage with two different aromatic capping units. The use of a simple phenyl cap leads to the generation of a Frenkel H-type exciton excited state with a reduced radiative rate and lowered fluorescence yield. This is an example of a passive capping group whose electronic states do not mix with those of the chromophore walls. The excited state properties are dominated by through-space interactions between the chromophore subunits themselves. Switching to a triazine cap provides the opportunity for chromophore-linker electron transfer and leads to the

formation of new CT states with enhanced fluorescence. The ability to create different nanoscale heterostructures while retaining the overall morphology provides an unprecedented opportunity to tune the properties of these discrete assemblies. This architecture is in principle scalable and may provide a path to systematically bridge the gap between molecular properties and solid-state material performance.

*4.2 Synthesis of Arylene Cages **4a** and **4b** and Model Compounds **6a** and **6b***

Using a ruthenium-catalyzed diol-diene [4+2] cycloaddition,[285] a protocol for benzannulation was developed in the laboratory of one of the present authors.[286] This method opened novel synthetic routes to diverse polycyclic aromatic hydrocarbons: acenes and fluoranthenes,[286] oligo(o,p-phenylenes) and, therefrom, nano-graphenes,[287] diindenoperylenes (periflanthenes),[288] rubicenes,[289] and a novel class of triple helical phenylene cages,[99] including an all-aryl caged fac-Ir(ppy)3 analog.[290] The relatively rigid topology of the arylene cages and the roughly orthogonal orientation of their walls vs caps inspired the design of the cages **4a** (Z = CH) and **4b** (Z = N), which have 5,5-(2,2-bithiophene) walls terminated by 1,3,5-benzene or s-triazine caps, respectively. The choice of thiophene walls was inspired by the fact that thiophene oligomers and polymers comprise an important family of organic semiconductors that have seen wide application in devices like photovoltaic cells and transistors. There has been extensive previous work on covalent thiophene assemblies, like dendrimers, that support energy migration[75,96] and

charge separation[81,89,94] and they have even been used in bulk heterojunction photovoltaics.[82,86] But so far, there has been no effort to create a single structural motif that can be engineered to serve either purpose.

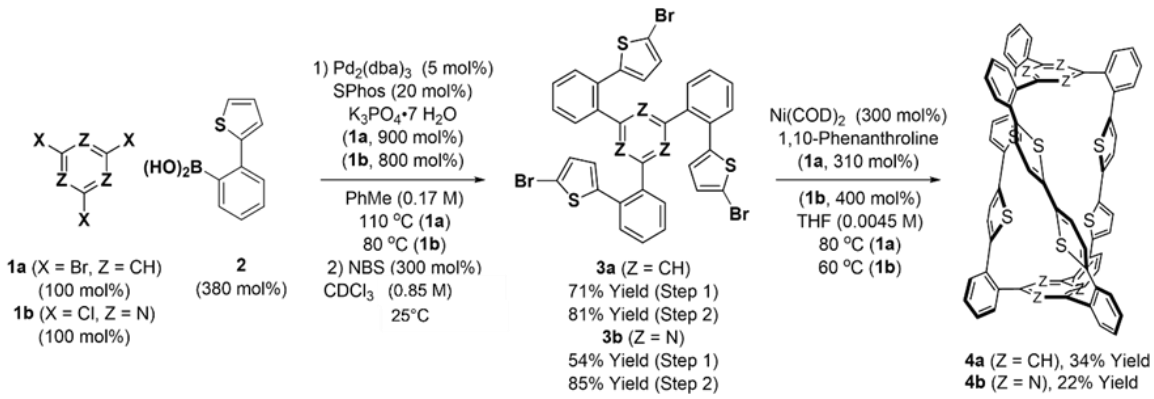

Figure 4.2. Synthesis of triazine-capped and benzene-capped 5,5′-(2,2-bithiophene)-containing arylene cages **4a** and **4b**. Yields of material isolated by silica gel chromatography. See Supporting Information for further experimental details.

The procedure for synthesizing the thiophene cage compounds is summarized in **Figure 4.2**. The all-benzene cages were prepared via dimerization of a tris-bromide,[99,290] requiring use of the ruthenium-catalyzed diol-diene benzannulation protocol due to its compatibility with aryl bromide functional groups. As thiophenes undergo efficient bromination at the 2-position,[78] the preparation of the benzene-capped 2,2-bithiophene cage **4a** was more directly achieved via 3-fold Suzuki coupling of 1,3,5-tribromobenzene 1a[291] and 2- thienylboronic acid 2 followed by 3-fold N-bromosuccinimide (NBS)-mediated bromination to form the tris-bromide 3a.[292] The latter reaction was conducted in $CDCl_3$ to enable monitoring of the reaction by ^1H NMR, as the tris-bromide 3a is not separable from the corresponding mono- and dibrominated compounds. The 3-fold reductive dimerization of tris-bromide 3a to form the benzene-capped cage **4a** via the

Lipshutz cuprate, $[Ar_2Cu(CN)Li_2]$[292] (as described by Iyoda),[90,293–296] and related methods involving direct 3-fold lithiation of the thiophene C−H bond adjacent to sulfur followed by $CuCl_2$ or $FeCl_3$-mediated dimerization,[80,84] were complicated by the formation of inseparable impurities. In contrast, 3-fold nickel(0)-mediated reductive dimerization[88,297–299] delivered the benzene-capped cage **4a** in 37% yield. In similar manner, 3-fold Suzuki coupling of cyanuric chloride 1b[291,300,301] and 2-thienylboronic acid 2 followed by 3-fold bromination mediated by N-bromosuccinimide (NBS) delivered tris-bromide 3b, which upon nickel(0)-mediated 3-fold reductive dimerization delivered the triazine-capped donor-acceptor cage **4b** in 22% yield (Scheme 1). Cages **4a** and **4b** could be crystallized via vapor diffusion of hexanes into dichloromethane and pentane into chloroform, respectively, allowing their structures to be corroborated by single crystal X-ray diffraction analysis (**Figure 4.3**).

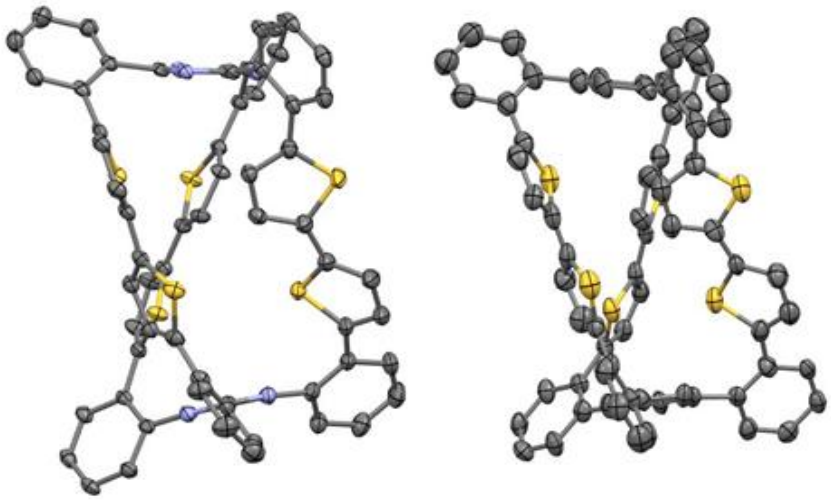

Figure 4.3. Single-crystal X-ray diffraction data of arylene cages **4b** (Left) and **4a** (Right). Displacement ellipsoids are scaled to the 50% probability level. Hydrogen atoms and solvent have been omitted for clarity.

The cage structures are chiral, but at room temperature, they appear to interconvert too rapidly to be resolved as separate species in NMR experiments or by chromatography.43 Finally, 2,2′-bithiophene model compounds **6a** and **6b**, which are terminated by phenyl and diphenyltriazine moieties, respectively, were prepared via direct 2-lithiation of the monothiophene precursors 5a and 5b followed by FeCl3-mediated dimerization (**Figure 4.4).**[80]

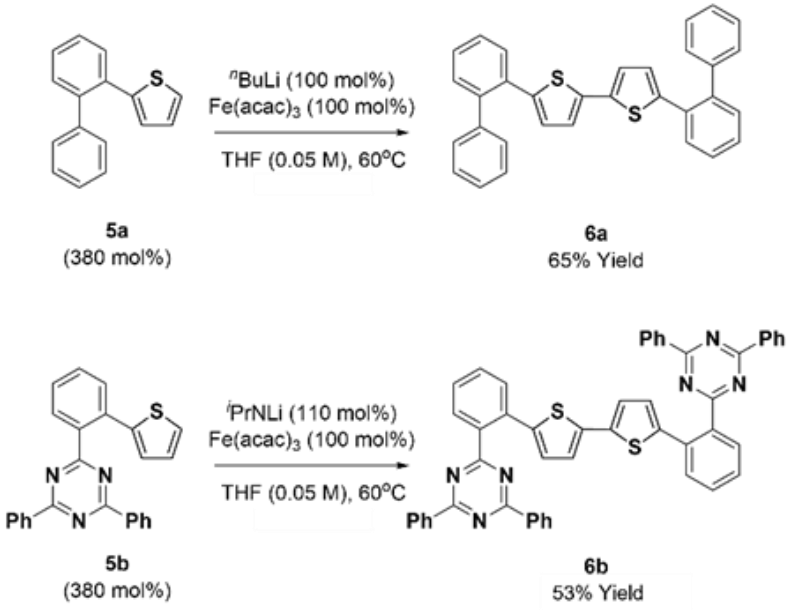

Figure 4.4. Synthesis of triazine-terminated and benzene- terminated model compounds **6a** and **6b** corresponding to dithiophene-containing arylene cages **4a** and **4b**.

*4.3 Photophysical Properties of Arylene Cages **4a** and **4b** and Related Computational Studies*

4.3.1 Evaluation of Conformational Disorder

It was posited that the geometric and conformational constraints of the present triple helical cage architectures would restrict the composite chromophores in a roughly orthogonal arrangement. Computational geometry optimization was used to compare the

geometries for the studied monomers and cages. We found several different minima on their respective ground state potential energy surfaces. Due to the absence of the cage structure, 8 different conformations of monomer **6a** are accessible at room temperature, as a low rotational barrier is associated with the biaryl linkage between benzene and thiophene moieties (**Figure 4.5** and **Table 4.1**).

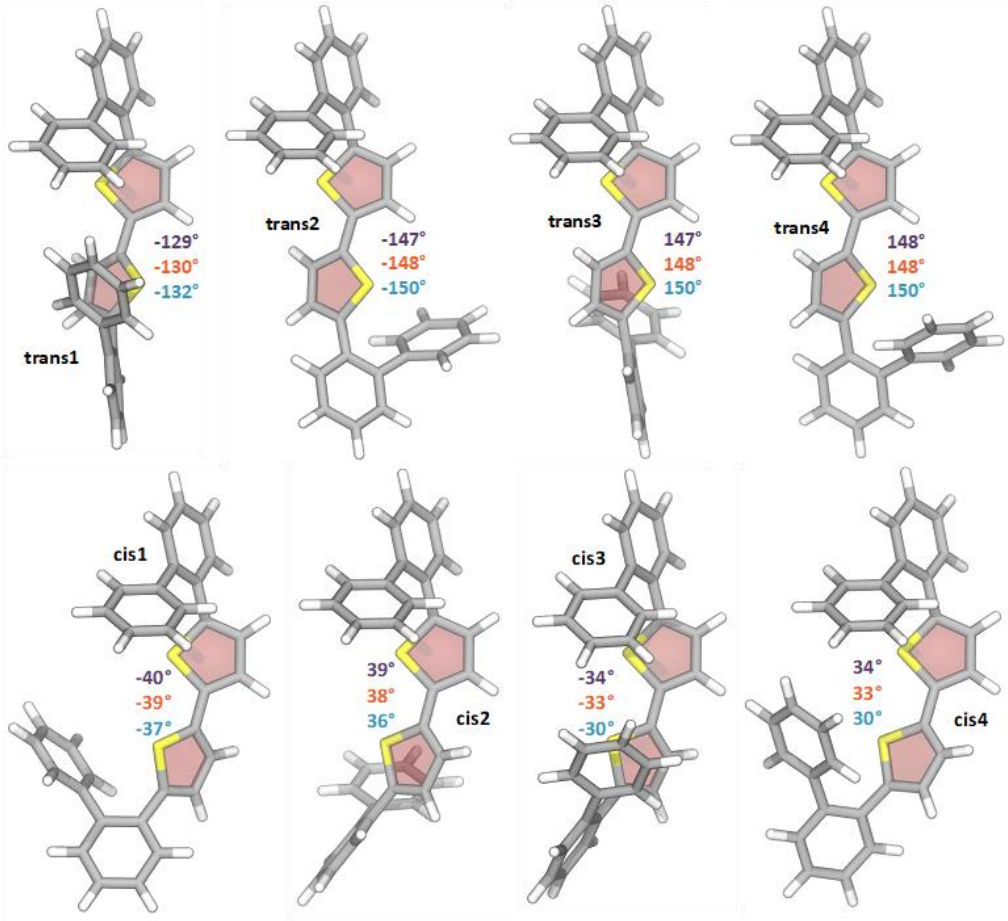

Figure 4.5. Equilibrium geometries and associated value of the SCCS dihedral angle for all geometries of **6a** obtained in gas phase (purple), cyclohexane (orange) and acetonitrile (blue).

	gas phase	cyclohexane	acetonitrile
trans1	0.00	0.07	0.06
trans2	0.28	0.27	0.40
trans3	0.28	0.27	0.40
trans4	0.02	0.00	0.22
cis1	0.57	0.53	0.46
cis2	1.16	1.09	0.96
cis3	0.36	0.34	0.00
cis4	0.36	0.34	0.00

Table 4.1. Relative energies (in kcal/mol) of the equilibrium geometries of the phenyl monomer **6a** in gas phase, cyclohexane and acetonitrile.

The steric hindrance associated with the larger triazine moiety reduces the configuration space energetically accessible in monomer **6b**, for which two quasi-isoenergetic conformers (ΔE = 0.7 kcal/mol) are found (**Figure 4.6** and **Table 4.2**).

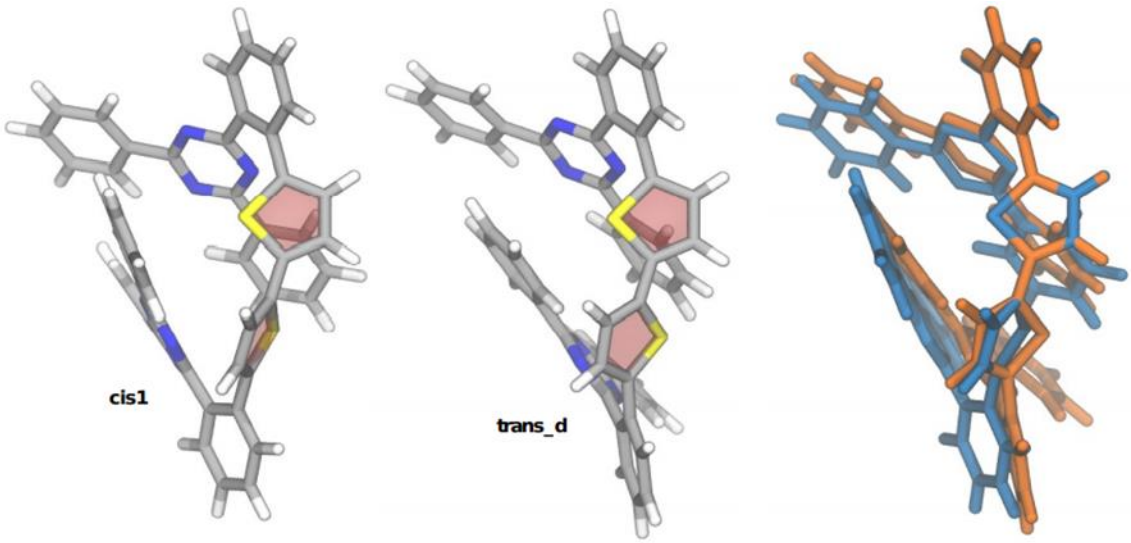

Figure 4.6. Equilibrium geometries of the lowest energy conformers of **6b**, *cis1* (in blue) and *trans_d* (in orange) as obtained from gas phase optimization.

	Gas Phase	Dihedral	Acetonitrile
trans1	0.00	106	
trans_d	0.66	133	0.73
trans_e_min	3.49	-151	
trans_e	4.30	164	4.50
trans_a	5.25	-54	
trans_b	5.25	54	
trans3	5.62	127	
trans_c	9.12	-135	
cis1	0.00	106	0.00
cis2	4.07	12	3.64
cis 3	10.24	-84	

Table 4.2. Relative energies (in kcal·mol^{-1}) of the equilibrium geometries of the triazine monomer **6b** in gas phase and acetonitrile.

The cage architecture provides different steric constraints, and two quasi-isoenergetic (ΔE = 0.8 kcal/mol) conformations were found for compounds **4a** (**Figure 4.7**) and **4b** (**Figure 4.7** and **Table 4.3**). To put these results in perspective, if we considered three chromophores, each able to freely adopt two conformations, we would naively expect to have $2^3 = 8$ local energy minima for the assemblies. In our computational search, we were only able to find two low-energy minima for **4a** and **4b** (within a given enantiomer of the triple helix), a remarkable reduction in the available phase space for these chromophores.

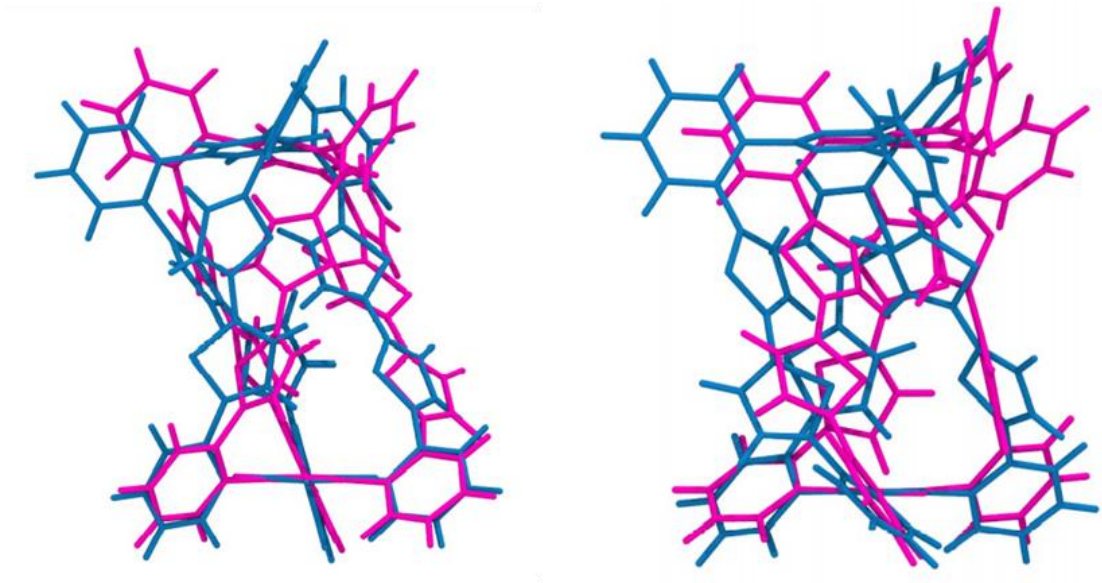

Figure 4.7. Left) Equilibrium geometries of the lowest energy conformers of **4a**, *cis1outside* (in blue) and *trans* (in magenta) as obtained from gas phase optimization. **Right)** Equilibrium geometries of the lowest energy conformers of **4b**, *trans* (in blue) and *cis1inside* (in magenta) as obtained from gas phase optimization.

	Gas Phase	**dih1**	**dih2**	**dih3**
trans	0.00	179	152	-145
1cis	4.68	-165	144	-138
1cis_inside	0.77	59	147	-136
2cis	3.01	-48	142	-166
2cis_2	10.78	142	155	122

Table 4.3. Relative energies (in kcal·mol^{-1}) of the equilibrium geometries of the triazine-capped cage **4b** in gas phase and SCCS dihedral value for the thiophene moiety of each individual branch.

The cage structure has the most pronounced effect on the conformational dynamics and electronic heterogeneity of the chromophores. Compounds **6a** and **6b** are structurally flexible with numerous quite flat vibrational modes involving different rotational motions and the relative torsion of conjugated rings. These molecular motions are notably restricted by the cage structure in **4a** and **4b**. The suppression of the low-frequency modes in **4a** and **4b** with respect to the monomeric compounds becomes evident when exploring the variation of vertical excitation energies at the Franck−Condon geometry triggered by molecular vibrations (**Figure 4.8**). The results clearly show that thermal activation of the low-frequency modes induces a much larger variation of the S_0-S_1 gap in **6a** than in cage **4a**. Again, theory confirms the general trend of reduced conformational freedom and narrower energy distributions for the cage structures, despite the presence of three chromophores instead of one.

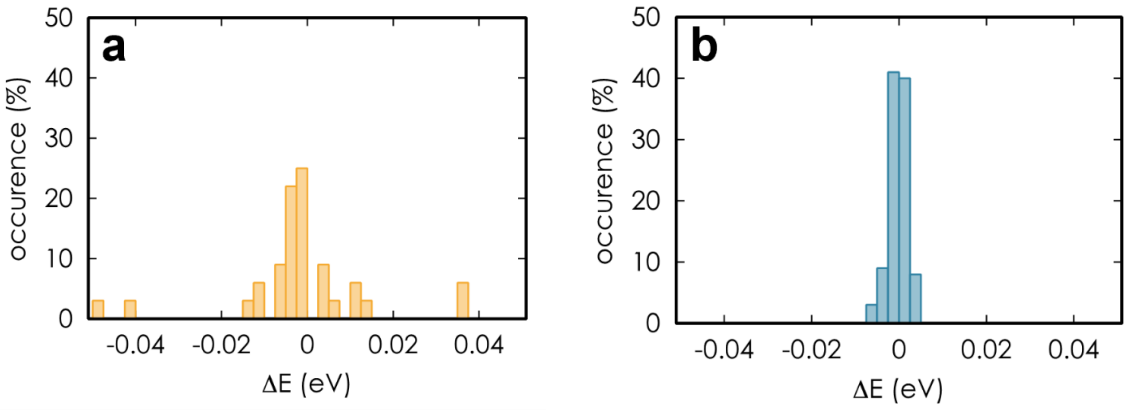

Figure 4.8. Histogram of the distribution of the changes in excitation energy to the S1 state of compound **6a** (a) and cage **4a** (b) upon thermal activation of the low-frequency modes.

*4.3.2 Inert Phenyl Linkers and Frenkel Exciton Formation in Compounds **4a** and **6a***

Due to the substantial vibronic coupling in the thiophenes, the reduced conformational freedom did not lead to an observable narrowing of the absorption spectrum, as shown in **Figure 4.9a**. In a comparison of the cage compound **4a** to the monomer **6a**, both spectra are featureless Gaussian-type peaks with a full-width-half-maximum of about 70 nm. The cage exhibits a slight blueshift of the main peak, along with the appearance of a red-shifted shoulder past 400 nm. This change in absorption line shape is a classic sign of H-type aggregation. In the standard Kasha model, side-by-side transition dipole moments (TDMs) interact to split the original monomer excited state into a strongly allowed exciton state at higher energy and a weaker state at lower energy.[302] This side-by-side geometry is created by the bithiophene cage walls. The absorption and fluorescence spectra of **4a** and **6a** are insensitive to solvent polarity (**Figure 4.10**), consistent with little or no CT character.

Additional experimental evidence for neutral, H-type excitons is provided by examination of the fluorescence spectrum. The 0−0 vibronic peak, which is clearly visible in **6a**'s fluorescence spectrum as a peak at 430 nm, is diminished in the spectrum of **4a**, where it now appears as a shoulder. By fitting each of the emission spectra to a set of three Gaussians with an equal spacing of 1350 cm−1 (**Figure 4.11**), we find that the amplitude of **4a**'s 0−0 peak decreases by ∼20% relative to that of **6a**. This loss of intensity in the 0−0 peak is another sign of H-type Frenkel exciton formation.[303]

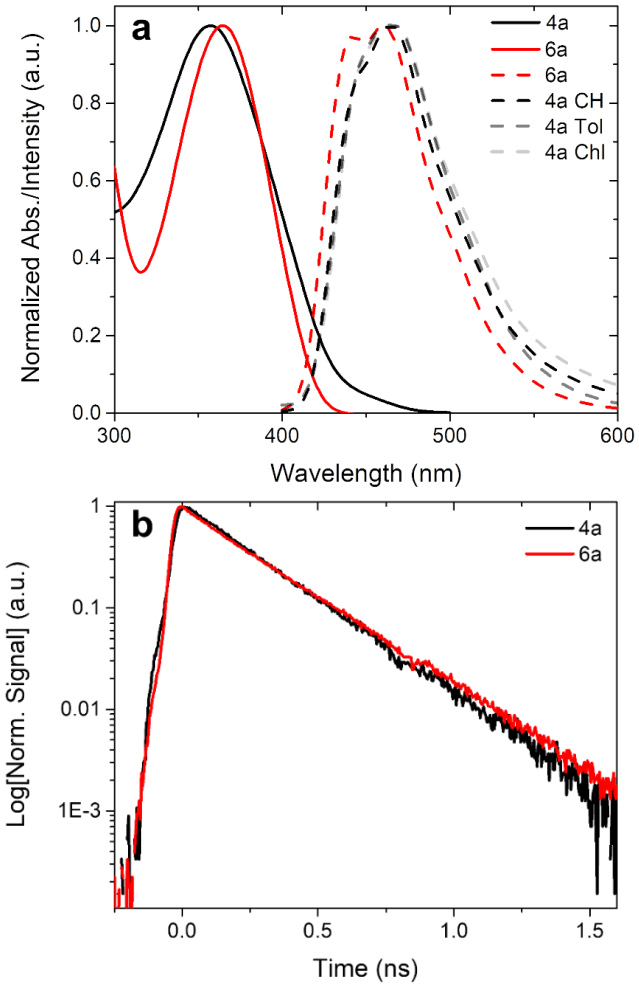

Figure 4.9. (a) UV-vis absorption (solid) and emission (dashed) spectra of phenyl-capped bithiophene cage (**4a**, black) and phenyl-capped monomer (**6a**, red). The emission of **4a** is shown in three solvents, cyclohexane (CH), toluene (Tol), and chloroform (Chl), to show no shift in the emission as solvent polarity increases. For the emission spectra, a 350 nm excitation wavelength was used. (b) Fluorescence decays of cage **4a** (black) and monomer **6a** (red) are almost identical.

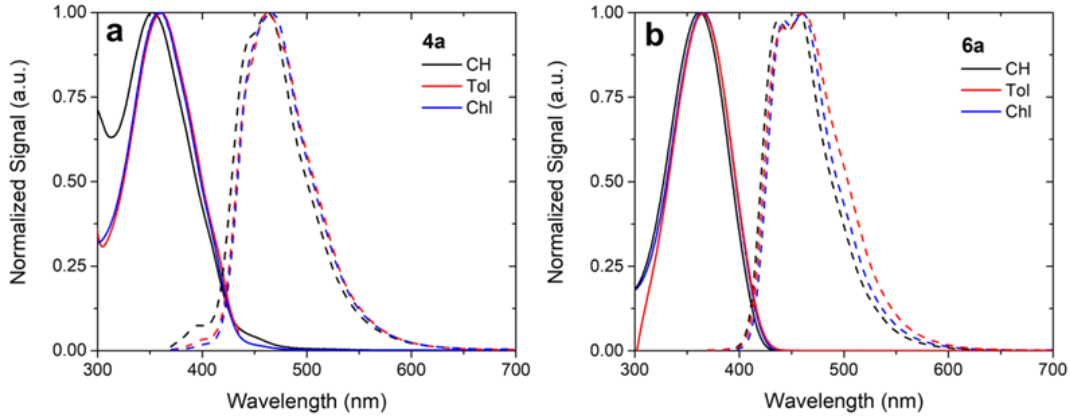

Figure 4.10. (a) Absorbance (solid) and emission (dashed) of cage **4a** in cyclohexane (CH), toluene (Tol), and chloroform (Chl) showing no solvent dependence. (b) Absorbance (solid) and emission (dashed) of monomer **6a** also showing no solvent dependence.

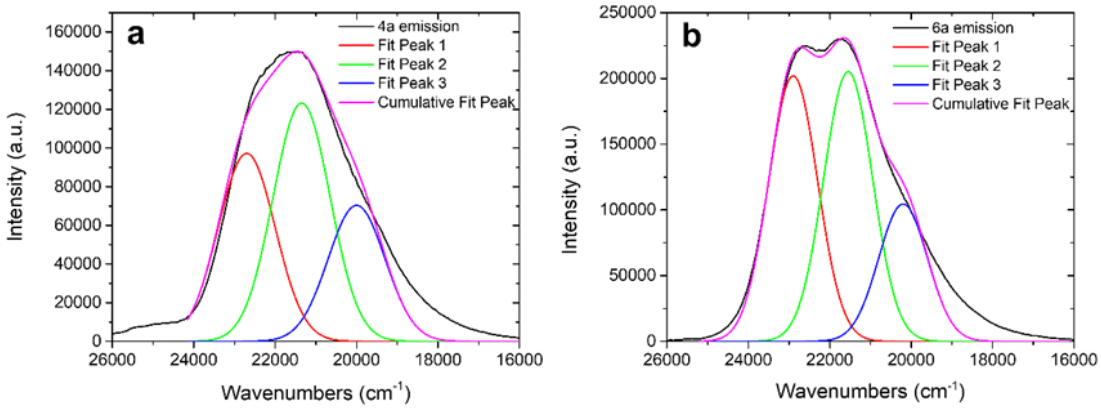

Figure 4.11. Emission spectra of **4a** (a) and **6a** (b) are shown in solid black. Three gaussians are fit to each emission spectrum to give the overall fit in pink. Peak 1 and peak 2 are fit to the 0-0 and 0-1 vibrational modes, respectively. Cage **4a** shows a 22% decrease of the 0-0 vibrational mode with respect to the 0-1 vibrational mode.

A final piece of evidence can be obtained by comparing the radiative rates (k_{rad}) of **4a** and **6a**. These two molecules have similar fluorescence lifetimes of 235 ± 10 ps as shown in **Figure 4.9b**, but the quantum yield of **4a** (0.06) is half that of **6a** (0.12), so we find k_{rad} =

0.25 ns^{-1} for **4a** and k_{rad} = 0.48 ns^{-1} for **6a**. The decreased k_{rad} value for **4a** is consistent with the low-lying emitting state having a weaker TDM, exactly as expected for an H-type aggregate. All three measurements (absorption line shape, fluorescence line shape, and radiative rate) are consistent with the idea that the cage structure supports the formation of neutral H-type excitons.

The last question is whether the modified cage excited state undergoes significantly different dynamics. To investigate the excited state relaxation dynamics, we utilized femtosecond transient absorption (fs-TA) experiments. **Figure 4.12a** shows the evolution of the TA spectrum of cage **4a** after 400 nm excitation. An initial excited state absorption (ESA) peaked at ∼710 nm, along with a negative signal at 480 nm, appears immediately after excitation. The ESA decays and is replaced by a weaker absorbance with a double peak at 520 and 600 nm that remains constant over the 1.1 ns time range of the experiment, which we assign to the $T_1 \rightarrow T_n$ absorption.

Global analysis shows only a single relaxation time of 203 ps required to adequately describe the time-dependent TA dynamics across multiple wavelengths (**Figure 4.12b**). The ESA decay is slightly faster than the measured fluorescence decay time, but their similar dynamics suggest that both observables correspond to the initially excited singlet state, which undergoes ISC to the triplet manifold. The fs-TA data for monomer **6a** are very similar to those in **Figure 4.12** (**Figure 4.13**), but with a slightly shorter singlet decay time of 190 ps. For both **4a** and **6a**, the rapid ∼200 ps ISC time (summarized in **Table 4.4**)

and blue-shifted $T_1 \rightarrow T_n$ ESA are consistent with the fs-TA behavior of other oligothiophene compounds, where ISC is the dominant nonradiative decay pathway.[95,101,102]

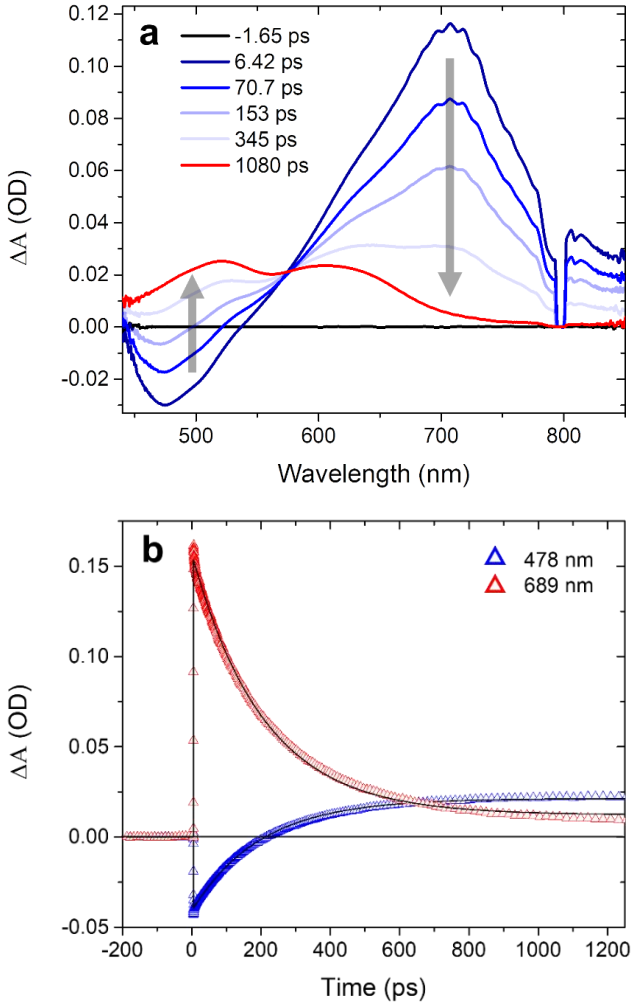

Figure 4.12. (a) TA spectra over time of phenyl-capped cage **4a** in chloroform. Arrows indicate spectral decline and growth over time. (b) Corresponding kinetic decays at selected wavelengths of initial negative signal (480 nm) and ESA (710 nm).

	Parameter	4a	6a
TRPL	τ_{PL} (ps)	229	244
TA	τ_{PL} (ps)	203	190
	Φ_{PL}	0.057	0.116
	k_{rad} (ns^{-1})	0.249	0.475

Table 4.4. Time-resolved photoluminescence (TRPL) and TA lifetimes of compounds **4a** and **6a**. The quantum yields (Φ_{PL}) and radiative rates (k_{rad}) are compared showing **4a**'s decreased radiative rate. Radiative rates are calculated using TRPL photoluminescence lifetimes, $k_{rad} = {}^{\Phi_{PL}}/_{\tau_{PL}}$.

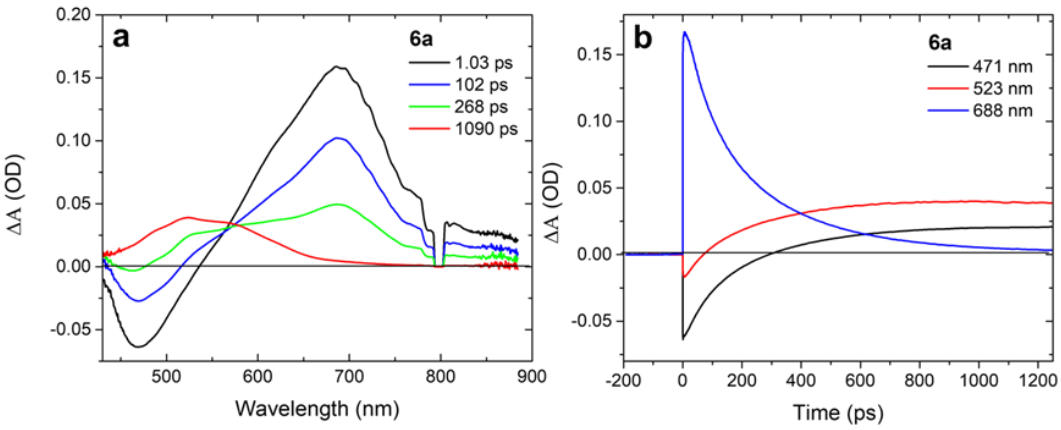

Figure 4.13. (a) Spectrum over time of **6a** in chloroform. (b) Associated kinetic traces at single wavelengths.

*4.3.3 Active Triazine Linker and CT States in Compounds **4b** and **6b**.*

The substitution of a triazine cap for the phenyl group has only a modest effect on the absorption spectrum of cage **4b** as compared to that of **4a**. Both cage compounds exhibit similar blue-shifted absorptions dominated by the bithiophene chromophore. Interestingly, the absorption of the corresponding monomer **6b** is broader and even exhibits a weak CT band at around 500 nm. As discussed above, we attribute the broadening to conformational disorder that is partially removed by the cage structure, and the CT feature probably

originates from one of these monomer conformations. When compared to **4a**, the main difference is seen in the fluorescence spectrum, which shifts from 450 to 550 nm and loses all vibronic structure. **4b**'s fluorescence peak position is also sensitive to solvent polarity, suggesting that the emitting state has CT character (**Figure 4.14**). The total fluorescence quantum yield for **4b** is 0.24, significantly greater than that of **4a**.

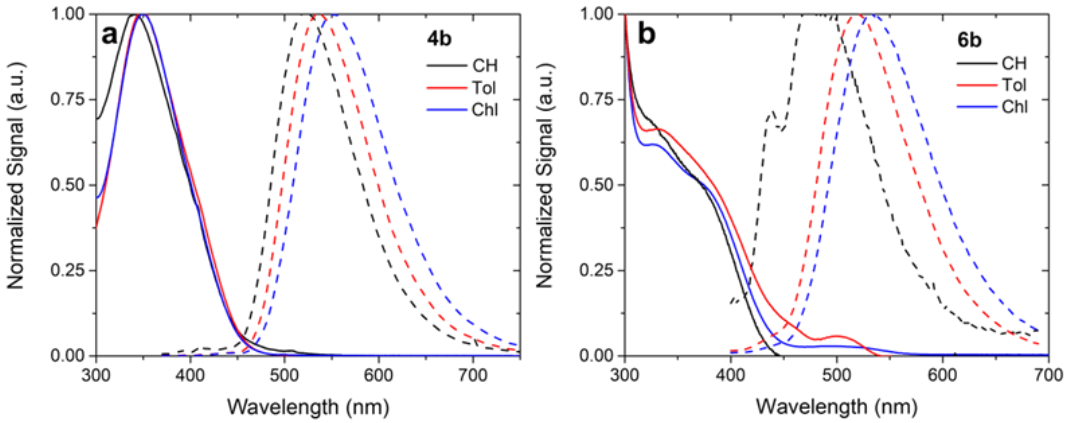

Figure 4.14. (a) Absorbance (solid) and emission (dashed) of cage **4b** in cyclohexane (CH), toluene (Tol), and chloroform (Chl) showing a stokes shift as polarity increases. (b) Absorbance (solid) and emission (dashed) of monomer **6b** also showing a stokes shift with increased polarity.

Finally, when the fluorescence decays are examined, **4b** is found to undergo a biexponential decay (**Figure 4.15b**). Its emission has a short component similar to those of the monomers (298 ps), but the majority of the fluorescence is emitted with a much longer lifetime of 4.3 ns (**Table 4.5**). The decay time of the long-lived component (4.3 ns) is about 6× greater than that of the analogous triazine-capped monomer **6b** (0.77 ns). The fluorescence spectrum redshifts slightly over the course of the decay (**Figure 4.16**), suggesting that the two lifetimes reflect two different CT states. Examining the solvent dependence of the decay, the relative amplitude of the long component increases in more

polar solvents, as does its lifetime (**Figure 4.17** and **Table 4.6**). This is again consistent with the long-lived state having CT character, since more polar solvents tend to favor charge separation and slow down recombination.

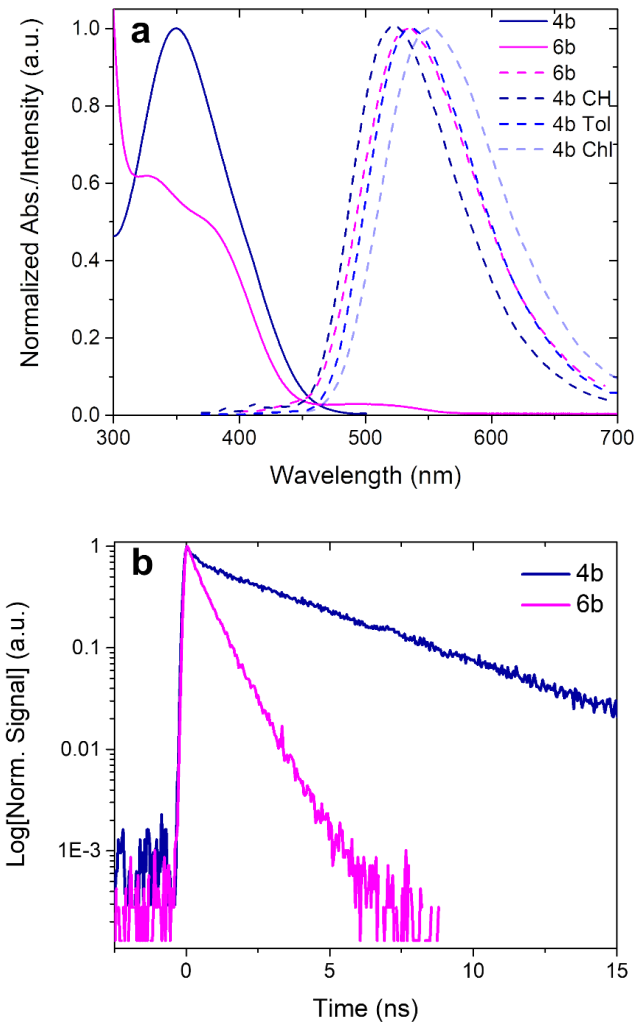

Figure 4.15. (a) UV-vis spectra (solid) and emission spectra (dashed) of triazine-capped bithiophene cage (**4b**, blue) and triazine-capped monomer (**6b**, pink). The emission of **4b** is shown in three solvents, cyclohexane (CH), toluene (Tol), and chloroform (Chl), to show the red-shifted emission peak as solvent polarity increases. For the emission spectra, a 350 nm excitation wavelength was used. (b) Fluorescence decays of cage **4b** (blue) and monomer **6b** (pink).

	Parameter	4b	6b
TRPL	τ_1 (ps)	298	277
	τ_2 (ns)	4.30	0.765
TA	τ_1 (ps)	6.64	6.72
	τ_2 (ps)	298	349
	Φ_{PL}	0.238	-
	k_{rad} (ns^{-1})	0.0758	-

Table 4.5. TRPL and TA photoluminescent lifetimes of compounds **4b** and **6b**. Note that the 6 ps decay time in the TA cannot be resolved by the TRPL measurement. The quantum yield (Φ_{PL}) and radiative rate ($\boldsymbol{k_{rad}}$) of **4b** are shown. The radiative lifetime is calculated using the weighted average of the two components from TRPL (0.298 ns (29%) and 4.30 ns (71%)). Therefore, $\tau_{PL} = (0.298 \cdot 0.29) + (4.30 \cdot 0.71) = 3.14\ ns$. Then the radiative rate can be calculated, $k_{rad} = {}^{0.238}/_{3.14} = 0.0758\ \text{ns}^{-1}$.

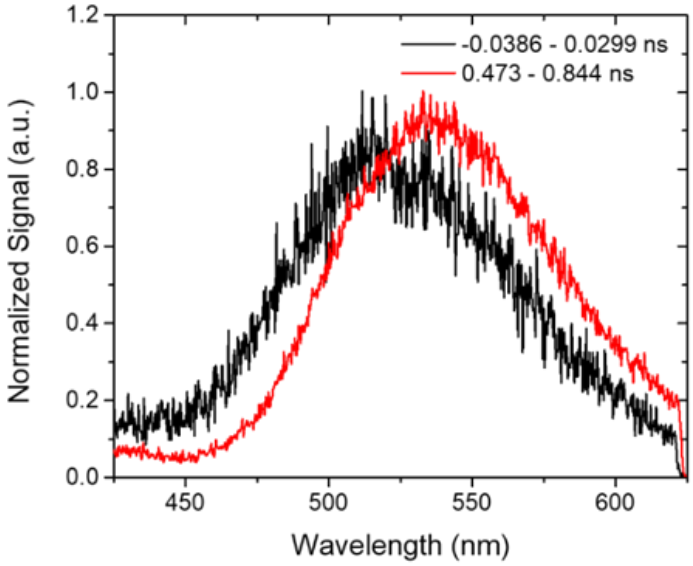

Figure 4.16. Spectrum of **4b** changing over time shows a redshifted emission at later times.

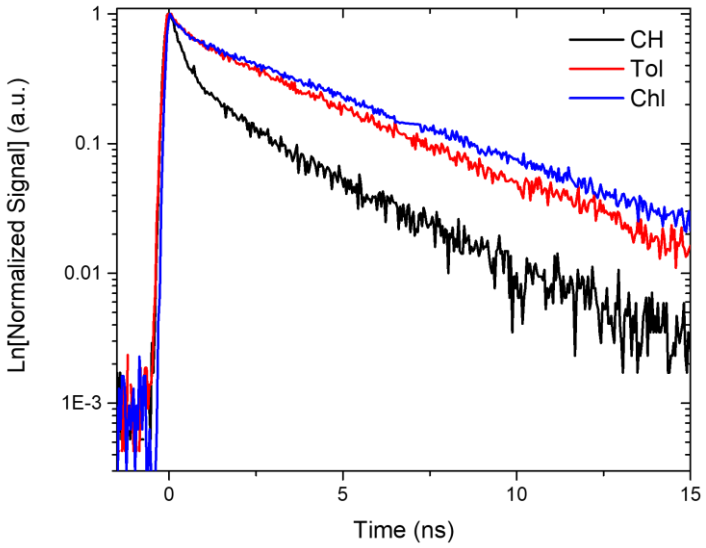

Figure 4.17. Solvent dependence of **4b** fluorescence decays shows a decrease in the short component and an increase in the long component and polarity of the solvent increases. The lifetimes and weighted components are shown in Table 4.6.

	t_1 (ns)	**%t_1**	**t_2 (ns)**	**%t_2**
CH	0.608	74	3.43	26
Tol	0.429	30	3.76	70
Chl	0.298	29	4.30	71

Table 4.6. Lifetimes of decays from Figure 4.17 using biexponential fits from the equation in section 2.3.6. As polarity increases from cyclohexane (CH) to toluene (Tol) to chloroform (Chl), the short component lifetime (t_1) and amount (%t_1) decreases and the long component lifetime (t_2) and amount (%t_2) increases. Percent components are determined from the A values in the biexponential fitting equation. All fluorescent decays were collected in a 20 ns window from 476-510 nm.

There is no sign of a CT absorption feature in **Figure 4.15a**, so the emissive CT state must form via relaxation from the neutral ~7 ps component that mainly reflects the loss of the stimulated emission feature and growth of an induced absorption around 500 nm, accompanied by a slight shifting of the main ESA feature at 650 nm. This rapid

relaxation was not observed in **4a** and can be assigned to the formation of a CT state from the initially excited Frenkel exciton. This initial decay is followed by a 300 ps process that mainly affects the large ESA peak at 650 nm, causing it to lose intensity and shift out to 700 nm. The long-lived ESA has different spectral features from the triplet ESA of **4a**, with a major peak at 700 nm instead of two weaker peaks centered around 500 and 600 nm. Since the 650 nm ESA peak decay is not accompanied by the growth of any other feature, including in the region expected for the $T_1 \rightarrow T_n$ ESA, we think it represents a subpopulation of CT states (possibly due to a different cage conformation) that undergo rapid internal conversion back to the ground state.

The behavior of **4b** can be compared to that of the corresponding monomer **6b** (bithiophene with triazine termination), which undergoes a similar 7 ps relaxation to the CT state, followed by a 350 ps decay that likely reflects rapid internal conversion and possibly some ISC to form a long-lived triplet with ESA features at 500 and 600 nm (SI, **Figures 4.19** and **4.20**. However, both the long-lived ESA at 700 nm and the long-lived CT emission are absent in **6b**, suggesting that the cage constraints allow **4b**'s CT state to avoid the rapid nonradiative relaxation processes found in **6b**.

Calculations showed that molecular torsions for the monomer **6b** can take place with almost no energetic cost (0.5 kcal/mol or less), confirming its high flexibility. To experimentally mimic the cage constraints, we measured the PL lifetime of **6b** in a rigid polymethylmethacrylate polymer matrix. We found a longer lifetime component of 2.4 ns

in the polymer (**Figure 4.21**), consistent with the idea that increased steric hindrance slows down the nonradiative decay. It is interesting that the solid-state matrix is less effective at preventing this relaxation than the cage in liquid solution.

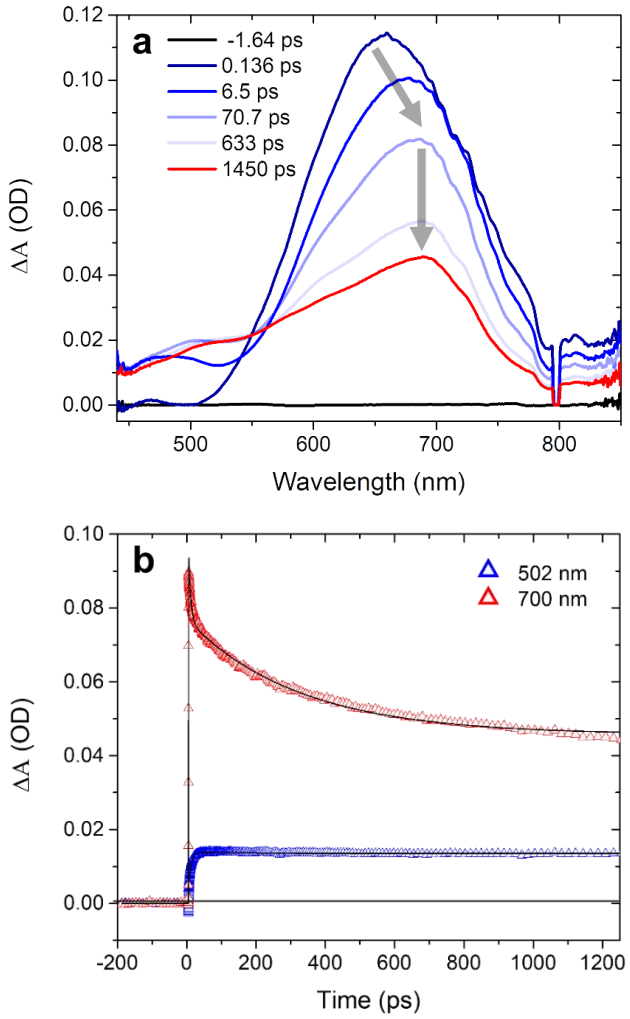

Figure 4.18. (a) TA spectra over time of triazine-capped cage (**4b**) in chloroform. Arrows indicate shift to longer wavelengths, followed by decay over time. (b) Corresponding kinetic decays at selected wavelengths of induced absorption (500 nm) and long-lived state (700 nm).

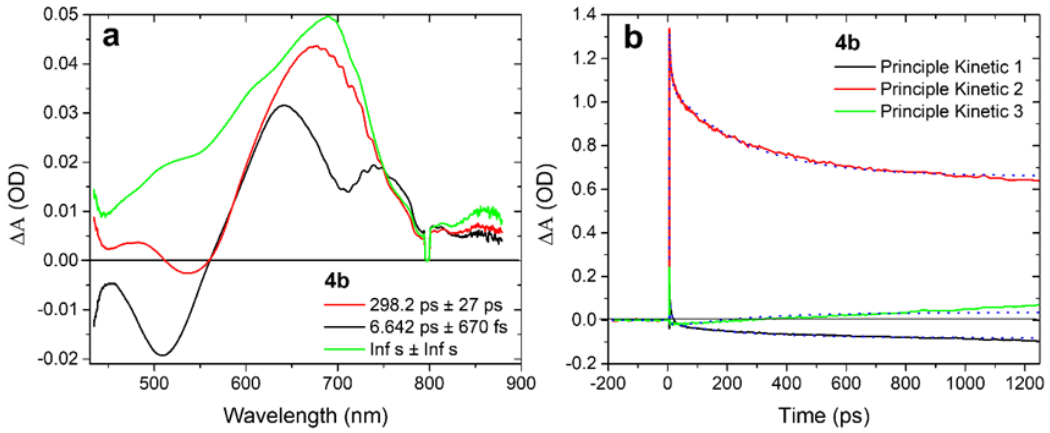

Figure 4.19. Global fitting analysis of **4b** in chloroform. (a) The spectra associated with the two principle components determined via SVD. (b) The kinetic traces of the principle components with overlaid fits (dotted lines).

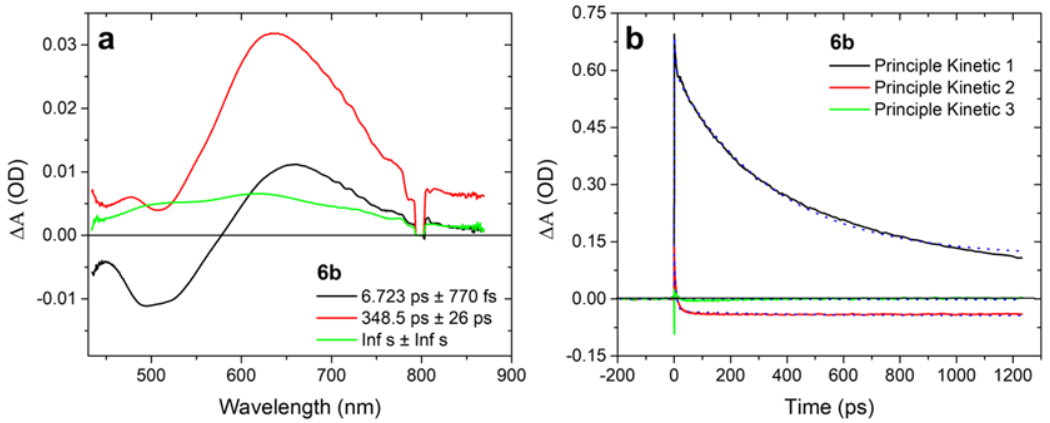

Figure 4.20. Global fitting analysis of **6b** in chloroform. (a) The spectra associated with the two principle components determined via SVD. (b) The kinetic traces of the principle components with overlaid fits (dotted lines).

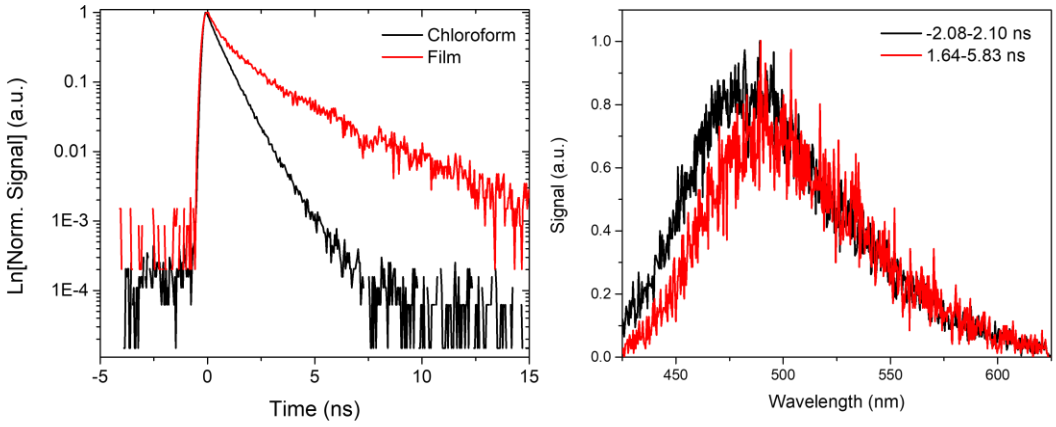

Figure 4.21. (a) Fluorescent decays of **6b** in solution (chloroform) vs. **6b** in a PMMA film showing an increased long-component lifetime in the solid-state film sample. In solution, $\tau_1 = 461\ ps$ with a relative amplitude of 55%; and $\tau_2 = 832\ ps$ with a relative amplitude of 45%. In the film, $\tau_1 = 547\ ps$ with a relative amplitude of 64%; and $\tau_2 = 2.38\ ns$ with a relative amplitude of 36%. (b) The spectra associated species of **6b** in the PMMA film at early times and later times to show that the spectrum does not change at later times; it only shows a slight redshift.

4.3.4 Computational Characterization of Cage Excited States.

The experimental absorption spectra suggest that the cage assembly supports some degree of excitonic character. To clarify how the cage structure modifies the excited electronic states, we turned to time-dependent density functional theory (TDDFT) calculations. Vertical electronic transition calculations for both **4a** and **4b** show that they possess three low-lying singlet states corresponding to the interaction of local excitations on the individual branches of the cage (**Figures 4.22** and **4.23**), with the highest excited singlet (S3) in both compounds presenting the largest oscillator strength (**Table 4.7**) but with appreciable oscillator strength remaining in the lowest states as well. This trend is

consistent with H-type exciton formation, but to confirm this, we performed additional calculations with a systematic series of approximations to isolate the effects of conformational disorder versus electronic coupling, concentrating on cage **4a**.

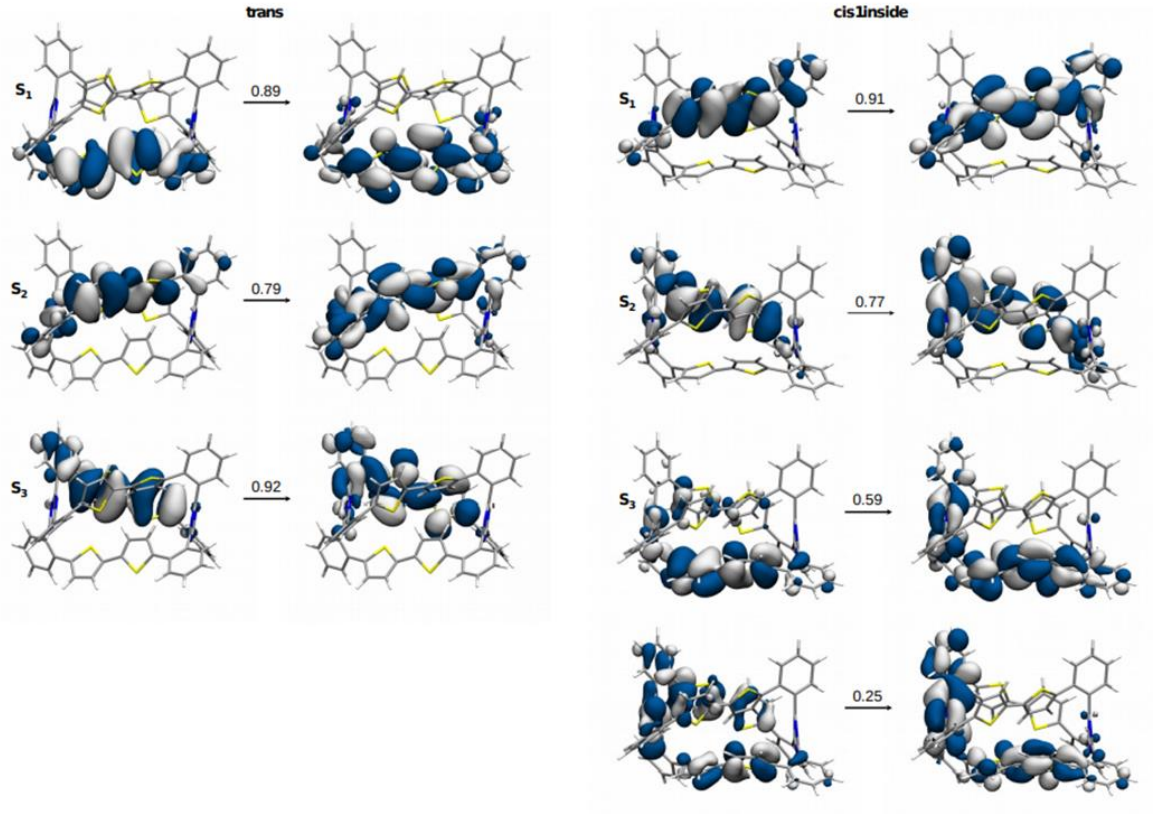

Figure 4.22. NTOs for excited states S_1-S_3 of the lowest energy conformers *trans* (left) and *cis1inside* of cage **4b**.

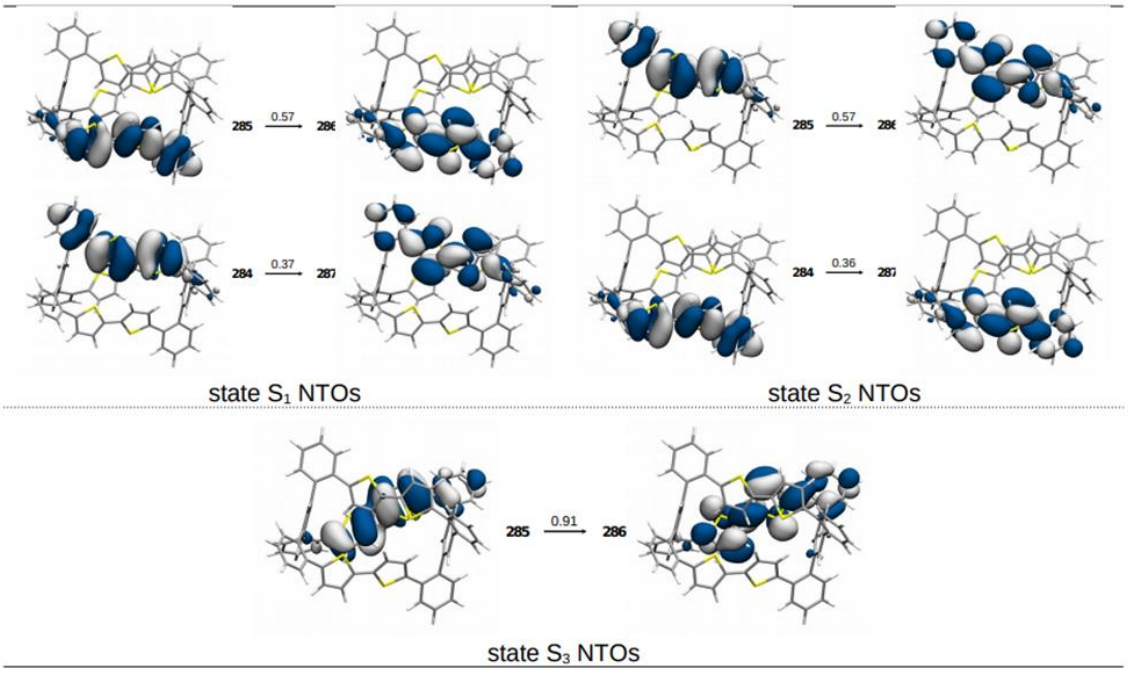

Figure 4.23. NTOs for excited state S_1, S_2, and S_3 of the lowest energy conformer of **4a**. The first three low-lying singlet states correspond to the interaction of local excitation on the individual branches of the cage.

	ΔE_1 (f_1)	ΔE_2 (f_2)	ΔE_3 (f_3)
Cage 4a			
monomers	3.60 (0.915)	3.61 (0.939)	3.92 (0.911)
point-dipole	3.48 (0.538)	3.57 (0.200)	4.09 (2.191)
multi-dipole	3.54 (0.164)	3.63 (0.970)	3.96 (1.714)
non-bonded trimer	3.63 (0.226)	3.70 (1.046)	3.97 (1.090)
cage	3.52 (0.100)	3.61 (0.840)	3.92 (1.160)
Cage 4b			
monomers	3.64 (0.884)	3.93 (0.743)	4.10 (0.765)
point-dipole	3.55 (0.294)	3.85 (0.172)	4.27 (2.097)
multi-dipole	3.62 (0.492)	3.91 (0.379)	4.14 (1.597)
non-bonded trimer	3.74 (0.672)	4.10 (0.397)	4.21 (1.274)
cage	3.60 (0.440)	3.90 (0.340)	4.12 (1.070)

Table 4.7. Excitation energies (in eV) and oscillator strengths (in parenthesis) for the three lowest excited singlets computed for non-interacting capped bithiophene (monomers), through the point-dipole and multi-dipole approximation, the non-bonded trimer and the full cage for compounds **4a** and **4b**.

First, we considered three individual capped bithiophene monomers with the frozen cage geometry without any intermolecular coupling. The three computed energies of each bright S_1 state show a sizable variation due to the different monomer structures within the cage, with each excitation energy close to the S_1−S_3 energies in the complete cage. Although different monomer conformations within the cage help explain the shifts in energy, the oscillator strengths of S_1 for the three monomers are relatively unaffected within this approximation, with values in the 0.91−0.94 and 0.74−0.88 range for monomers in **4b** and **4a**, respectively. Second, we turned on electronic interactions between the subunits using several levels of approximation. The center-to-center spatial separation between bithiophene units lies in the range 5.1−5.7 Å, similar to the size of the chromophore itself. The close proximity suggests that the point-dipole approximation will not be adequate, since this tends to overestimate the exciton couplings.[97,304,305] Indeed, this model overestimated the splitting by ∼0.2 eV, as shown in **Table 4.7**. The use of a multidipole model designed to include molecular size effects can accurately reproduce the cage energies and transition dipole moments from the full quantum calculation. The good agreement suggests that short-range CT interactions triggered by intermonomer orbital overlap play a minor role (at most) in the main absorption band of cages **4a** and **4b**. To confirm this, we analyzed the three lowest singlet−singlet transitions using a nonbonded trimer model obtained by removing the benzene and triazine (top and bottom) capping rings in **4a** and **4b**, respectively. Calculated excitation energies and oscillator strengths follow the same distribution as in the full cage results, in agreement with a through-space exciton coupling. The main difference is that the energies of the nonbonded trimers are

systematically blue-shifted with respect to the cages, which results from the reduction of the effective conjugated length of the system.

Using the multidipole model, we can calculate intermolecular exciton coupling constants in the range of 60−80 meV, depending on the chromophore pair. These couplings are larger than those deduced for polythiophene, which range from 5 to 30 meV depending on the preparation method.[306] The larger coupling may result partly from the short bithiophene segments used in the cage,[307] but it is still well below the couplings observed in oligothiophene crystals, which are typically greater than 200 meV.[308–310] The calculations suggest that the cage geometry can achieve electronic couplings intermediate between a disordered polymer and tightly packed crystal, leading to novel excitonic states that have intermediate properties as well.

The calculations show that the initial absorption event creates a neutral excited state in both **4a** and **4b**, consistent with their similar absorption spectra, but after that, their paths diverge. **Table 4.7** summarizes the full quantum calculations of the low-lying neutral states of **4b**, and they are similar to those of **4a**. Unlike **4a**, however, electronic structure calculations indicate that **4b** also supports multiple low-lying singlet states with CT character. Excited state optimization of **4b** identifies low energy CT state minima with reduced gaps to the ground state and nonvanishing oscillator strengths (**Table 4.8**). All three low-lying states in this geometry (CT_1, CT_2 and CT_3) exhibit significant CT character, in which bithiophene moieties and triazine rings act as electron donor and acceptor groups, respectively (**Figure 4.24**). The CT states in cage **4a** are computed at much higher energies,

and their involvement in the decay of photoexcited cage **4a** seems energetically forbidden. This result is consistent with the experimental observation of an emissive CT state in **4b** that is reached by picosecond relaxation from the Franck−Condon geometry.

Finally, we note that the calculated oscillator strengths agree qualitatively with the trends observed experimentally. If we compare the neutral ^{1}FE states of **4a** and **6a**, we find that the computed ratio of 1.02:0.71 = 1.4 is not far from the experimental k_{rad} ratio of 0.48/0.25 = 1.9. If we compare the neutral exciton state of **4a** with the CT state of **4b**, we find the experimental k_{rad} ratio 0.25/0.08 = 3.1 is greater than the calculated ratio of oscillator strengths, 0.71:0.43 = 1.7, but consistent with the observation that the CT state retains significant oscillator strength.

Compound	**State**	E_{vert}	ΔE	**Strength**
Monomer 6a	^{1}FE	2.85	-0.68[a]	1.02
Cage 4a	^{1}FE	2.79	-0.45[a] / -1.075[b]	0.71
	^{1}CT	3.43	0.41[a] / 0.005[b]	0.01
Monomer 6b	^{1}CT	2.86	-0.55[a]	0.30
Cage 4b	$^1CT_1$	2.64	-0.22[a] / -0.78[b]	0.43
	$^1CT_2$	2.93	-0.17[a] / -0.73[b]	0.51
	$^1CT_3$	3.14	0.14[a] / -0.41[b]	0.12

Table 4.8. Vertical and relative energies (in eV) and oscillator strengths at excited state minima of monomers **6b** and **6a**, and cages **4b** and **4a**. FE: Frenkel exciton; CT: charge transfer state. [a]Computed with respect to the vertical excitation energy of S_1 at the ground state geometry. [b]Computed with respect to the vertical excitation energy of S_3 at the ground state geometry.

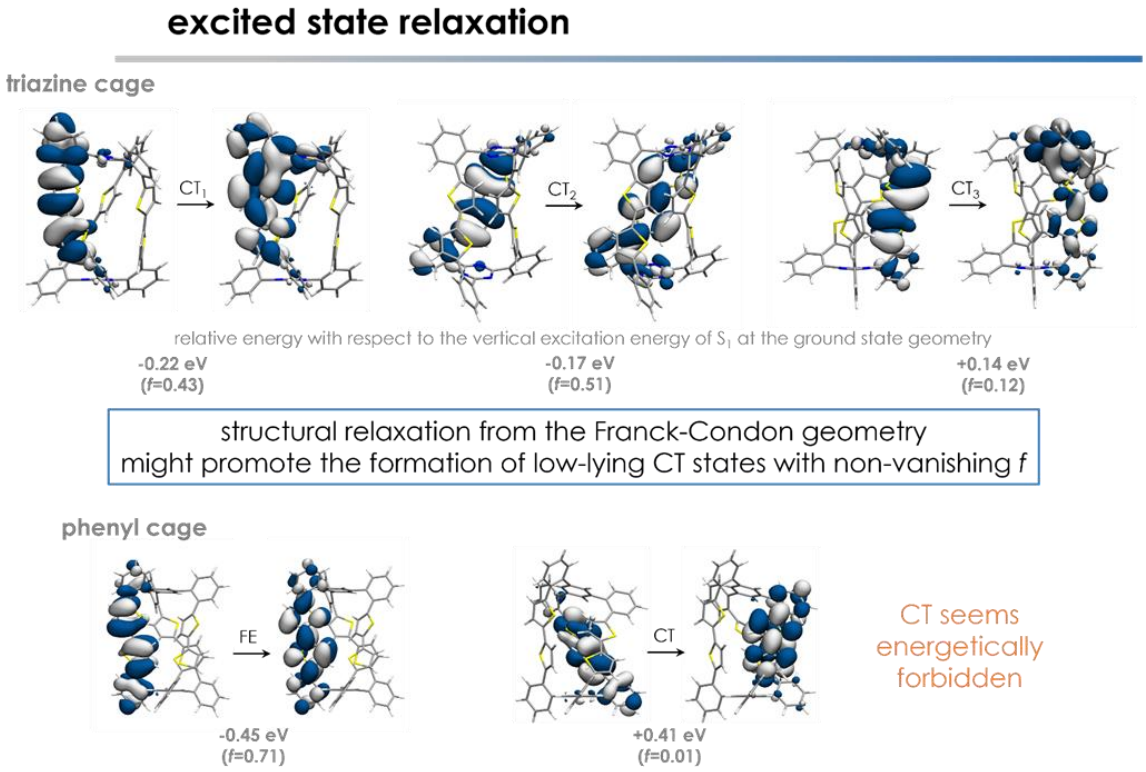

Figure 4.24. Excited state relaxation of the triazine cage (**4b**) showing CT character present in the lowest lying states and phenyl cage (**4a**) showing that CT is energetically forbidden.

4.4 Discussion

The photophysical behaviors of **4a** and **4b** are summarized in the Jablonski diagrams in **Figure 4.25**. On the basis of the experimental and computational results in the previous sections, we can draw several conclusions. First, the lowest vertical transitions in cages **4a** and **4b** reflect two main contributions: (i) conformational disorder between the three coupled moieties and (ii) through-space interchromophore Coulomb interaction. In fact, the calculations show that the blue shift in the absorbance is primarily the result of the constrained cage shifting the localized excited state and not the formation of a fully

delocalized H-type exciton. The S_3 excited states in **Figure 4.25** are more localized than calculated exciton states in phenyl-cored dendrimers,[83] possibly due to the orthogonality of the capping groups. It is remarkable that both theory and experiment show that through-space Coulombic interactions enable the S_3 state to steal considerable oscillator strength from the lower energy states, despite the fact that visually the wave functions show limited delocalization.

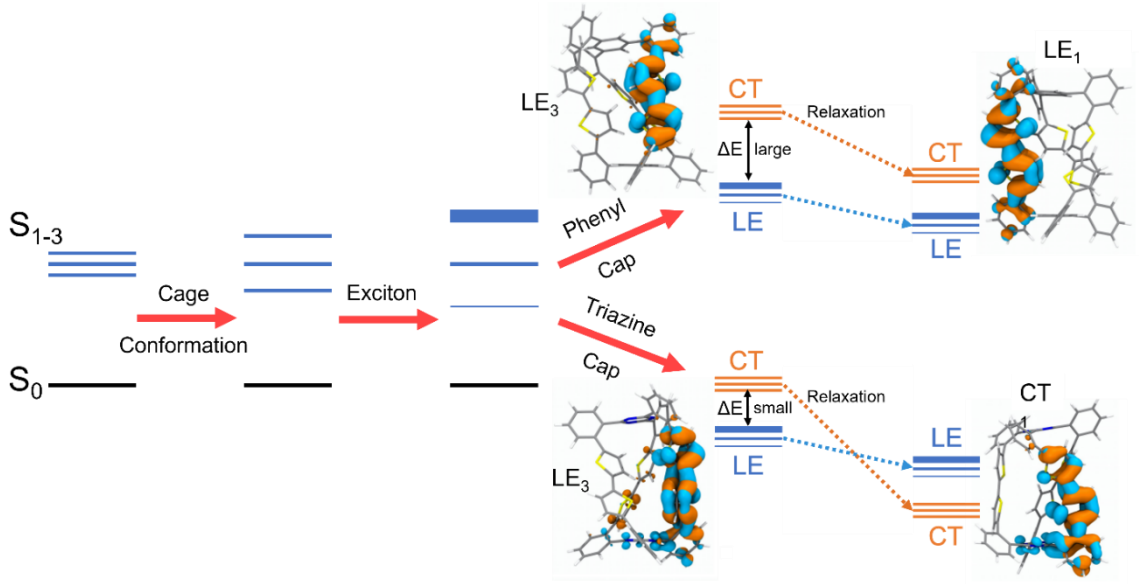

Figure 4.25. Jablonski diagram representing the singlet energy level shifting from three non-interacting capped bithiophenes to capped bithiophene cages and then the excitonic state. Then the schematic outline of the relaxation processes in the phenyl-capped cage (**4a**) is shown, along with the main (88% of the transition) electron/hole pair densities for the S3 state. The schematic outline of relaxation processes in the trazine-capped cage (**4b**) is shown, along with the main (95% of the transition) showing the electron/hole pair densities (blue/orange) for the lowest CT state.

This illustrates how subtle through-space chromophore−chromophore interactions can affect the electronic properties of the cage even with orthogonal phenylene caps that prevent through-bond orbital interactions. Modifying the chromophore "walls" by using moieties with different TDM strengths or orientations could modify the strength of the intermolecular coupling and allow the construction of more delocalized Frenkel exciton states with different properties, e.g., enhanced radiative rates (superradiance).

While the initial excited state is determined by the chromophore wall geometry, its subsequent fate can be controlled by the linker properties. For the inert capping group of **4a**, the ISC rate appears to be largely unaffected by exciton state formation, which acts mainly to reduce the competing radiative rate. For cage **4b**, the initially excited state is similar to that of **4a** but rapidly relaxes into a CT state, a fraction of which survives for 4.3 ns. The use of the triazine cap introduces a conformationally restricted CT state that can largely avoid the rapid ISC and internal conversion that quench the fluorescence of monomer **6a**, enhancing the fluorescence quantum yield of **4b** relative to **4a**. **4b**'s CT state has significant electron−hole overlap, as can be seen from **Figure 4.25**, leading to a singlet−triplet energy gap greater than 1.0 eV (**Table 4.9**). This large gap prevents facile intersystem crossing, as observed in thermally activated delayed fluorescence emitters that have a greater degree of charge separation. The ability of thiophene CT states to avoid ISC has been observed in previous work,[282] but the origin of this ability has yet to be satisfactorily explained.

molecule	ΔE	f
4b[a]	1.18	0.49
4CzIPN[b]	0.13	0.07
DABNA-1[c]	0.15	0.31

[a] TDA-DFT, ωB97XD/6-31+G(d).
[b] TDA-DFT, LC-ωPBE/6-311+g(d,p) and with ε = 3.
[c] From [Nat. Commun. 10 (2019) 597].

Table 4.9. Singlet-triplet energy gap (D*E* in eV) and oscillator strength (*f*) for the lowest CT state of **4b**, 4CzIPN and DABNA-1. These results indicate that the CT state in **4b** has an intermediate CT character with a sizeable hole/electron overlap resulting in large singlet-triplet gap (exchange interaction) and strong oscillator strength. The CT state in **4b** has a donor-acceptor long-range excitation character, like in 4CzIPN, but the spatial electron/hole separation in **4b** is much weaker than in 4CzIPN, as manifested by the smaller gap and oscillator strength in the latter. The CT character in DABNA-1 is rather different, which has been characterized as a short-range CT transition, with small singlet triplet gap but large oscillator strength.

The overall picture that emerges is that different elements of the cage structure can be used to control different time periods of the assembly photophysics. The initial excited state structure is largely determined by the geometry of the chromophore walls and the detailed chemical structure of the caps has little impact on the structure of this state. But the subsequent relaxation of this excitonic state, from picoseconds onward, depends strongly on the nature of the capping group. A noninteracting cap simply allows the chromophore's intrinsic relaxation to proceed (e.g., ISC), but a different cap structure can open up new pathways (e.g., CT) that can outcompete the intrinsic processes. In this way, the cage approach could enable the use of different wall/cap module combinations to rationally design the photophysical behavior of molecular chromophore assemblies.

4.5 Conclusions

The newly developed cage-type architecture enables the construction of multichromophoric molecules with tunable linkers. Although the cage framework still has some flexibility even with its additional bonding constraints, it provides the opportunity to examine assemblies of bithiophene chromophores in two limits: inert linkers that support through-space interchromophore interactions and active linkers that modify the electronic states. The first type of linker is demonstrated by the phenyl cap which enables H-type Frenkel exciton formation. This excitonic state still undergoes facile ISC, but the weak TDM of the low-lying emitting state suppresses the fluorescence output by a factor of 2. The use of a triazine cap introduces low-lying CT states that can avoid ISC and enhance the fluorescence yield. Both capping groups lead to low-lying neutral excitonic states with weaker oscillator strengths, but the triazine linker provides a new CT relaxation pathway that can avoid ISC and generate a higher overall fluorescence quantum yield. While many workers have shown how covalently linking chromophores can produce new excited states, this paper shows how chemical tuning can precisely control the nature of those states, even for the same geometrical arrangement. These results provide a new route toward structurally well-defined multichromophoric assemblies whose excited states can be rationally designed using the tools of organic synthesis and computational chemistry.

Chapter 5: Nanosecond Laser-Induced Liquid-Gas Transition for Light-to-Mechanical Energy Conversion

5.1 Introduction

Gas expansion has long been harnessed to generate mechanical work in heat engines, thanks to the large volume changes that can be achieved. The development of soft robotics has motivated research into nontraditional actuation mechanisms that rely on this phenomenon.[115,117,118,121,311–318] A common strategy to create a large volume expansion involves heating a high density working fluid to cause a liquid→gas phase transition. In most cases, the heat required to vaporize the working fluid is supplied by a resistive heater embedded in the actuator structure.[119,120,313] An alternative strategy is to surround the liquid with an absorbing medium that can convert light into heat.[319] The photothermal strategy avoids electrical contacts and allows the actuator to be controlled remotely.

One challenge for the liquid→gas actuation strategy is to selectively deposit the heat into the working fluid while minimizing heat loss to the surroundings. Heat that diffuses into the surrounding actuator structure cannot raise the temperature of the working fluid and contribute to the work output, which lowers the overall efficiency. This had led to the use of pulsed heating, even down to the microsecond timescale, to try to minimize thermal losses.[116,158–160] There are now many examples of electrically pulsed liquid→gas actuators, but the reported efficiencies remain low, typically on the order of 0.1%.[116,320–322]

The efficient transduction of laser light into mechanical energy has also been the subject of interest for the shock wave and laser propulsion communities. Workers in the shock-wave field have developed the laser flyer concept in which a solid organic layer is sandwiched between a massive transparent substrate (usually glass) and a thin (<100 μm) metal layer (usually composed of aluminum (Al)).[162,163,165,166,170–172,174,175] The impact of a high energy nanosecond laser pulse causes rapid heating of the metal film and explosive decomposition of the organic layer, launching the metal film away from the substrate at high velocities. The conversion of laser energy into plate kinetic energy can reach efficiencies as high as 50%.[164,168,169] Laser flyers are not candidates for actuator applications because the impact of the laser pulse destroys the solid-state device and the thin metal film cannot be reused. However, the high light-to-mechanical energy conversion efficiencies reported in this literature motivated us to examine whether nanosecond impulsive laser heating could be applied to a liquid→gas transition that is more amenable for use in actuators. A preliminary examination of the performance characteristics should indicate whether this direction is worth pursuing.

In this paper, we investigate how laser-induced impulsive heating, adapted from the laser flyer literature, can be applied to liquid→gas actuation. We design a simple laser flyer apparatus in which a variable volume of liquid can be confined next to a metal plate. When a high-energy nanosecond laser pulse impacts the plate, explosive vaporization of the liquid beneath it propels it upward. The initial velocity of the plate, and thus its kinetic energy, is measured under a variety of conditions, including liquid volume, laser wavelength, pulse energy, and the chemical composition of the working fluid. A simple

model is proposed to explain the observed dependence of the velocity on the liquid heat of vaporization. We find that the impulsive laser heating is confined to a relatively small volume adjacent to the metal plate, even when a large total volume of liquid is used, and that this expanding volume can propel the metal plate with energy conversion efficiencies that approach 2%. Although some surface modification of the metal is observed due to liquid decomposition at high temperatures, there was no measurable decrease in the energy conversion even after 200 cycles. Our results suggest that nanosecond pulsed laser heating for liquid→gas actuation may be worth studying as a new light-based way to supply mechanical energy to robotic devices.

5.2 Results and Discussion

After testing a variety of metals using H_2O as the working fluid (**Figure 5.1**), we found that Al plates exhibited the greatest laser-induced motion. The high responsiveness of Al when exposed to high power laser pulses is consistent with its high susceptibility to ablation in air and water.[323,324] The simple design of the liquid→gas flyer shown in **Figure 5.2** resulted in a reproducible impulse to the Al plate as long as the metal cylinder was glued to the underlying plexiglass. **Figure 5.3** shows a sequence of images for a typical experiment. The impact of the laser pulse launches the Al plate vertically, accompanied by a splash of the liquid. For a 450 mJ laser pulse and D=1.0 mm, video analysis of 5 different samples yielded an average initial velocity v_i =3.5 ±0.2 m/s, giving a 5% variance.

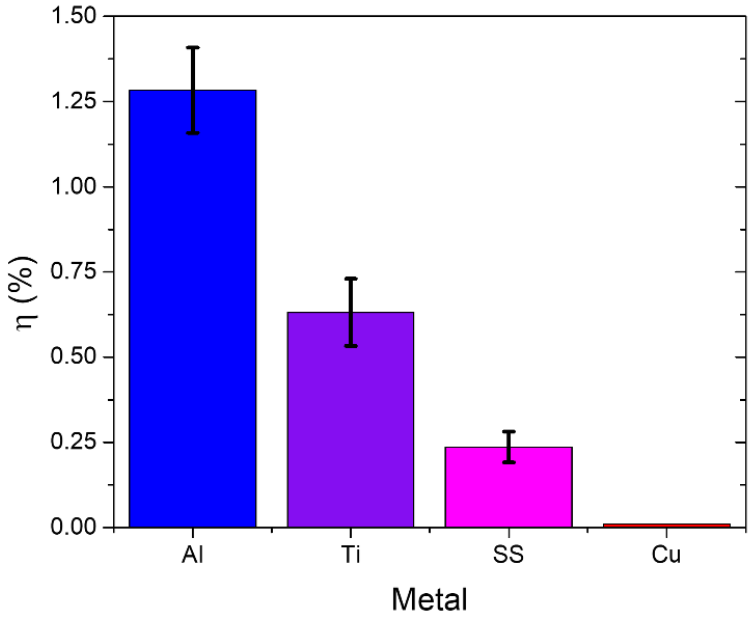

Figure 5.1. The efficiencies of different metals aluminum (Al), titanium (Ti), stainless steel (SS), and copper (Cu) of the same length and widths are compared. The metal plate thickness is varied to make the masses of the samples equivalent, except Ti with half the mass of the other metals (mass is used in efficiency calculation to account for this). Each metal was tested with a spacer of D=1 mm filled with H_2O.

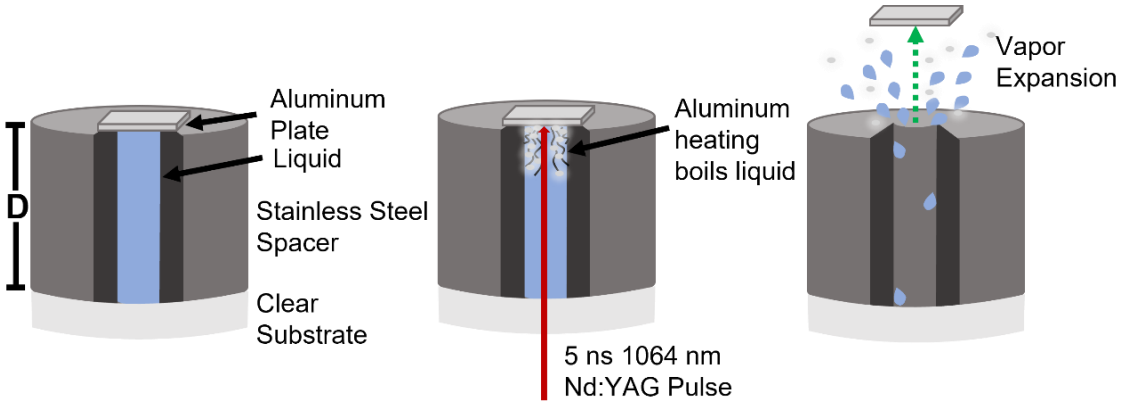

Figure 5.2. Schematic of metal plate laser propulsion experiment. Liquid fills a 9 mm diameter hole in a cylinder with depth D and the metal rectangular plate is placed on top of this hole. A 1064 nm, 5 ns pulse is directed through the clear substrate to hit the bottom of the metal plate. The metal transfers thermal energy to the liquid, which undergoes explosive vaporization, propelling the plate upward.

Although confinement of the liquid was necessary to obtain the large and consistent v_i values for all D values, motion could still be observed when the Al plate was suspended above unconfined liquid. We compared the performance of this system to two different set-ups in which the Al plate was in contact with 1 mm of water above the transparent PMMA substrate.

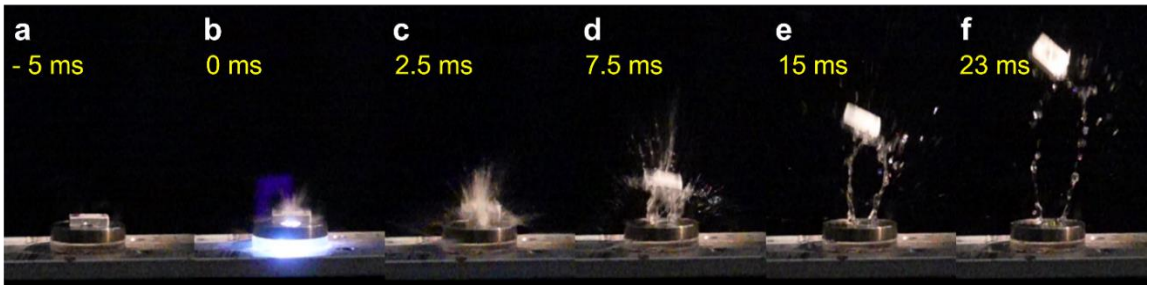

Figure 5.3. Sequence of images after a single 1064 nm, 0.5 J laser pulse hits an Al plate on top of a cylinder with D=2 mm. The images show (a) 5 ms before the laser pulse is fired; (b) the impact of the laser pulse at time zero; (c) 2.5 ms after the laser pulse when the plate flies off the cylinder with liquid splashing out; and (d)-(f) from 15 to 23 ms after time 0, the plate increases in height while the water droplets disperse.

If the metal surface was not glued to the substrate, the average v_i=2.5 m/s was lower and there was greater variability in v_i, with a standard deviation of 20%. If no cylinder was used and the Al plate was suspended above an unconfined layer of water, the laser-induced vaporization could still launch the plate, but again with a lower v_i=2.8 ±0.3 m/s (**Figure 5.4**). Sealing the metal cylinder to the underlying transparent substrate leads to a significant improvement in v_i and reproducibility. However, we were surprised that the enhancement was not larger. Its relatively small effect on v_i probably reflects that most of the propulsion is due to vaporization of a thin interfacial layer that does not feel the confinement on the timescale of the experiment.

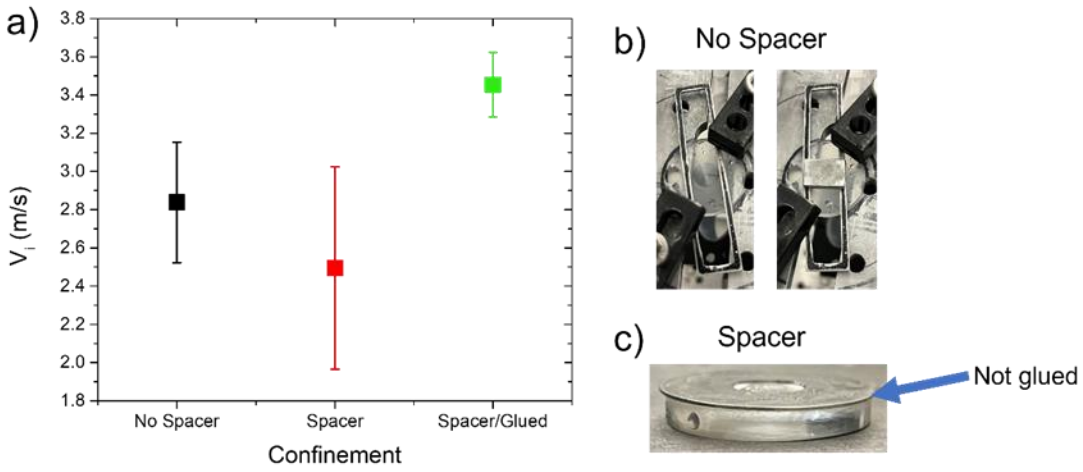

Figure 5.4. The role of the system confinement is quantified (a) by comparing the v_i with and without a spacer to show increased v_i and lower error for the spacer that is glued to the plexiglass. No spacer means that the aluminum plate was held 1 mm off the plexiglass with a rectangular mold, as seen in (b) Spacer means that the normal 1 mm spacer was used, but it was not glued to the plexiglass, as seen in (c) Spacer/glued means that the spacer was glued to the plexiglass to create a tight seal. For all data, a spacer with D=1 mm is filled with water (H_2O).

If most of the propulsion is due to interfacial vaporization, then we do not expect the total volume of the fluid cylinder to have a dramatic effect on v_i. To examine the role of the total liquid volume, we systematically varied D, the depth of the cylinder, while keeping other variables constant. Two working fluids, H_2O and pentane, were tested.

As seen in **Figure 5.5**, for H_2O the largest v_i occurs at D=1.0 mm, while for pentane there is no dependence on D until after 1.0 mm. Interestingly, as D increases up to 20.0 mm, v_i only decreases by about a factor of 2 for both liquids.

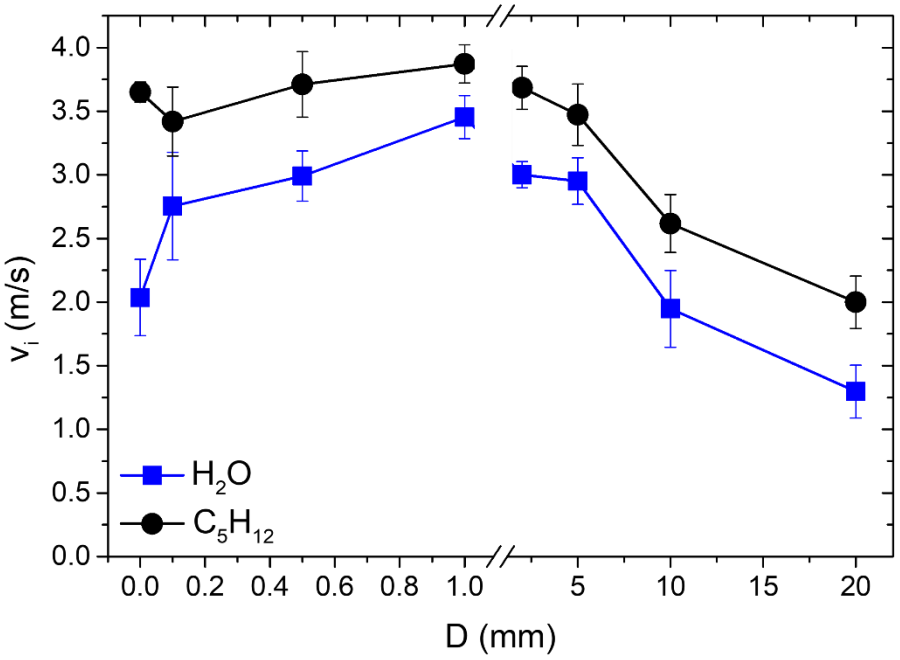

Figure 5.5. The initial velocity (v_i) is plotted as a function of cylinder depth D = 0-20 mm. Data for water (H_2O) and pentane (C_5H_{12}) are shown.

Since liquids typically have a low compressibility, most of the gas expansion will be directed at the Al plate. For larger D values, the cylinder confinement provided slightly greater v_i values, but even for D=20 mm, the plate was launched with a v_i of 0.7 ±0.2 m/s, about half the value observed for a fully confined H_2O fluid with D=20 mm. In those experiments, the liquid volume was large enough that a large bubble could be observed to expand and ripple through the water as the Al plate was launched.

In addition to vaporization, laser heating can also initiate chemical changes. For protic solvents like water, methanol, and ethylene glycol, the Al plate exhibited a whitish

discoloration after laser impact that is likely due to surface oxidation. In alkane liquids, a black soot-like film developed on the Al surface (**Figure 5.6**). Interestingly, neither surface change had a measurable effect on v_i after up to 200 cycles (**Figure 5.7**).

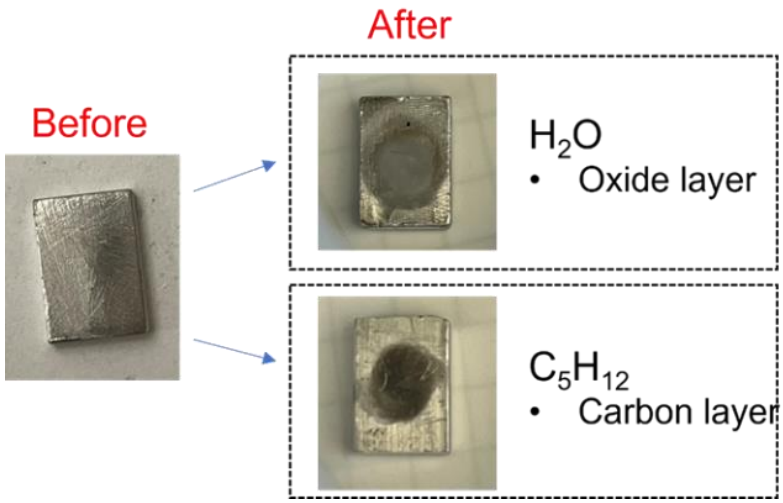

Figure 5.6. An image of the aluminum plate before laser impact (left) is shown to compare to the surface after laser impact (right). When water (H_2O) was filled in the spacer upon laser irradiation, a white layer is left on the surface, most likely representative of an oxide layer. When n-pentane (C_5H_{12}) was filled in the spacer upon laser irradiation, a black layer is left on the surface, representative of carbon decomposition.

The plexiglass substrate, on the other hand, did sustain damage, typically after 5-10 cycles when D=1.0 mm. This change usually consisted of cloudiness within the substrate, surface abrasion, and hairline cracks (**Figure 5.8**). We confirmed that this damage did not occur when the cylinder was empty. For larger D values, up to 20 mm, damage to the plexiglass plate was still observed after >20 laser shots, but it degraded in a different manner than for the D=1.0 mm samples. For larger D values, the plexiglass would slowly lose transmission and turn dark, rather than crack, which we ascribed to laser excitation of internal defects in the plastic.

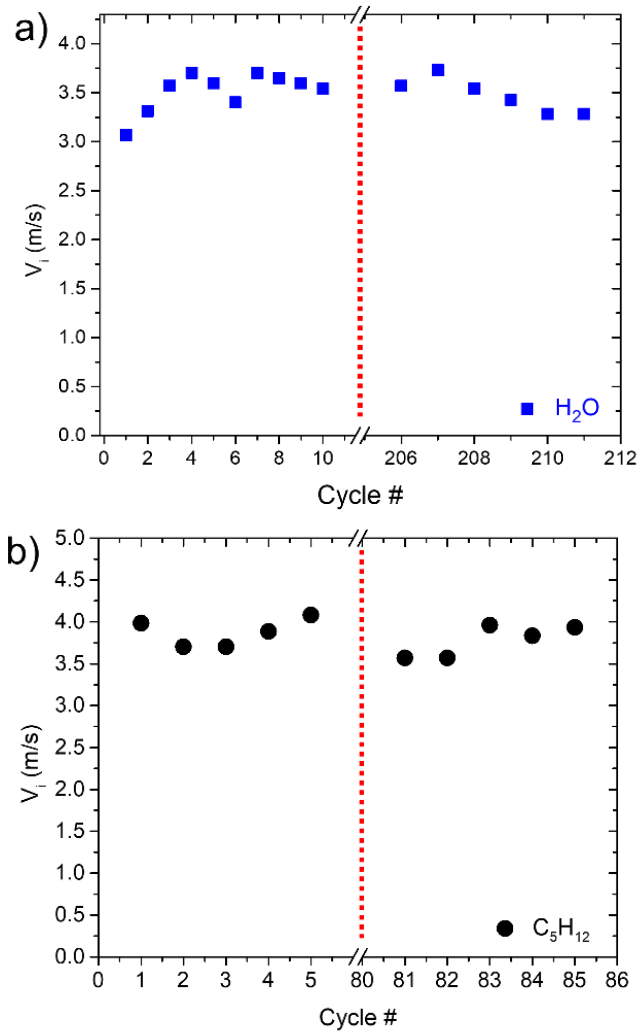

Figure 5.7. a) A 0.941 g Al plate was shot with a single pulse over 200 times with water (H_2O) filled in the spacer showing v_i reproducibility within ≈15%. b) The same 0.941 g Al plate was shot with a single pulse over 80 times with n-pentane (C_5H_{12}) filled in the spacer showing v_i reproducibility within ≈10%.

Figure 5.8. The system is currently limited by PMMA substrate that is ablated (a), internally damaged (b), or cracked (c) after 5-20 pulses depending on piece of plexiglass and spacer height.

We tested two different laser wavelengths, 1064 nm and 532 nm, for D=1.0 mm and H_2O as the working fluid. 532 nm has a smaller penetration depth into Al, which leads to enhanced effectiveness for ablation and nanoparticle generation.[241,325–328] We expected that 532 nm would result in a larger v_i due to enhanced fluid heating, but we observed the opposite trend. For a fixed pulse energy of 0.20 J, a 1064 nm pulse yielded v_i=1.2±0.1 m/s, while a 532 nm pulse yielded v_i=0.7 ±0.1 m/s. We did not investigate this wavelength dependence in more detail but it is suggestive that processes beyond simple Al absorption may play a significant role in heating the liquid. It is possible that 532 nm produces a different distribution of ionizing versus heating outcomes that result in less rapid heating of the liquid adjacent to the Al. Alternatively, it is possible that vaporization during the pulse changes the sample optical properties, causing the incoming 532 nm light to be scattered more than 1064 nm light. A more detailed study of the vaporization dynamics would be required to understand the origin of this wavelength dependence.

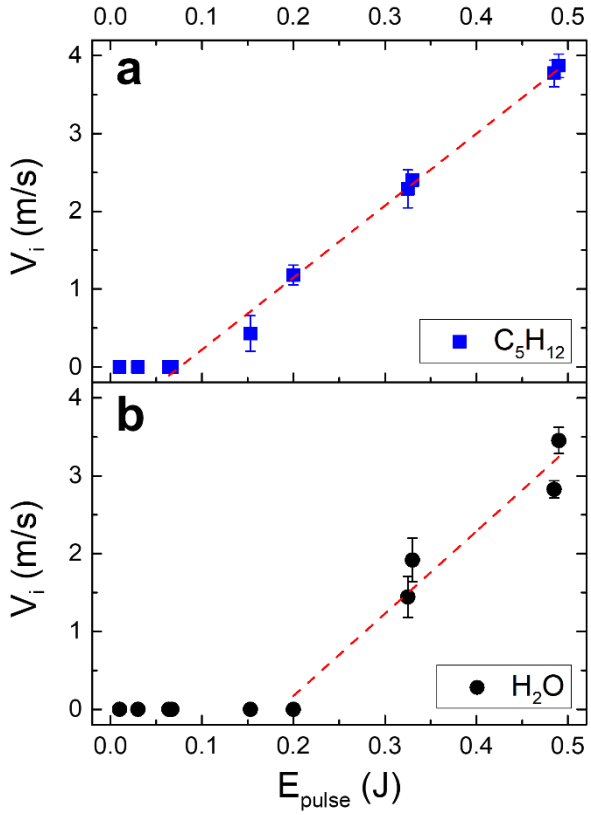

Figure 5.9. The initial velocity v_i is plotted against the laser pulse energy E_{pulse} for (a) water (H_2O) and (b) pentane (C_5H_{12}). The energy threshold where movement starts to occur is 0.2 J for H_2O and 0.07 J for C_5H_{12}, after which vi increases linearly with E_{pulse}.

Varying the 1064 nm pulse energy revealed a pronounced energy threshold for generating vertical motion. **Figure 5.9** shows how v_i depends on pulse energy for two liquids, pentane and H_2O. In both liquids there is no detectable motion until the energy thresholds of 0.07 J for pentane and 0.20 J for H_2O are reached. After this threshold, v_i increases roughly linearly with E_{pulse}. The dependence of v_i on liquid in **Figure 5.9** was general. In **Figure 5.10** we show v_i values measured for different liquids using a 1064 nm pulse with E_{pulse}=0.45 J. There are two interesting aspects of **Figure 5.10**.

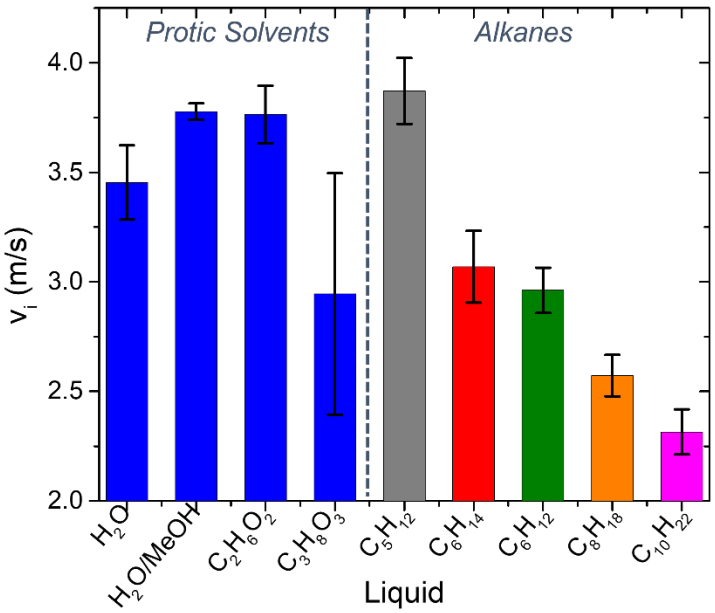

Figure 5.10. v_i values for protic solvents (blue) and a variety of alkanes are shown. Each value represents an average of at least 10 experiments with a 0.45 J, 1064 nm laser pulse and D=1.0 mm. The alkanes are shown in different colors to highlight the trend in decreasing v_i with increased chain length. The protic solvents shown are water (H_2O), a 90% water + 10% methanol mixture (H_2O/MeOH), ethylene glycol ($C_2H_6O_2$), and glycerol ($C_3H_8O_3$). The alkanes are shown in order of increasing chain length, n-Pentane (C_5H_{12}), n-Hexane (C_6H_{14}), cyclohexane (C_6H_{12}), n-Octane (C_8H_{18}), and n-Decane ($C_{10}H_{22}$).

First, the protic solvents (H_2O, methanol, ethylene glycol and glycerol) all show comparable v_i values, even though the glycerol data has a large standard deviation that may reflect the difficulty of preparing a filled cylinder with this highly viscous liquid. This suggests that these liquids give rise to explosive boiling through a comparable mechanism that is relatively insensitive to properties like viscosity, boiling point, enthalpy of vaporization, and heat capacity (**Table 5.1** and **Figure 5.11**).

	Viscosity (μ)	Boiling Point (T_b)	Enthalpy of Vaporization (ΔH_{vap})	Heat Capacity (c_p^l) (@298 K)
	mPa·s	K	kJ/mol	J/mol·K
H_2O/MeOH	1.317[329]	366[330]	37.43[329]	64.5[331]
H_2O	1.002[332]	373[333]	37.6[333]	75.4[334]
$C_2H_6O_2$	20.16[335]	471[333]	65.0[333]	149.8[336]
$C_3H_8O_3$	863.0[337]	550[333]	91.7[338]	218.9[338]

Table 5.1. Physical constants of protic solvents, an aqueous mixture of water:methanol 90:10% (H_2O/MeOH), water (H_2O), ethylene glycol ($C_2H_6O_2$), and glycerol ($C_3H_8O_3$), used to plot against their respective initial velocities (v_i) in Figure 5.11.

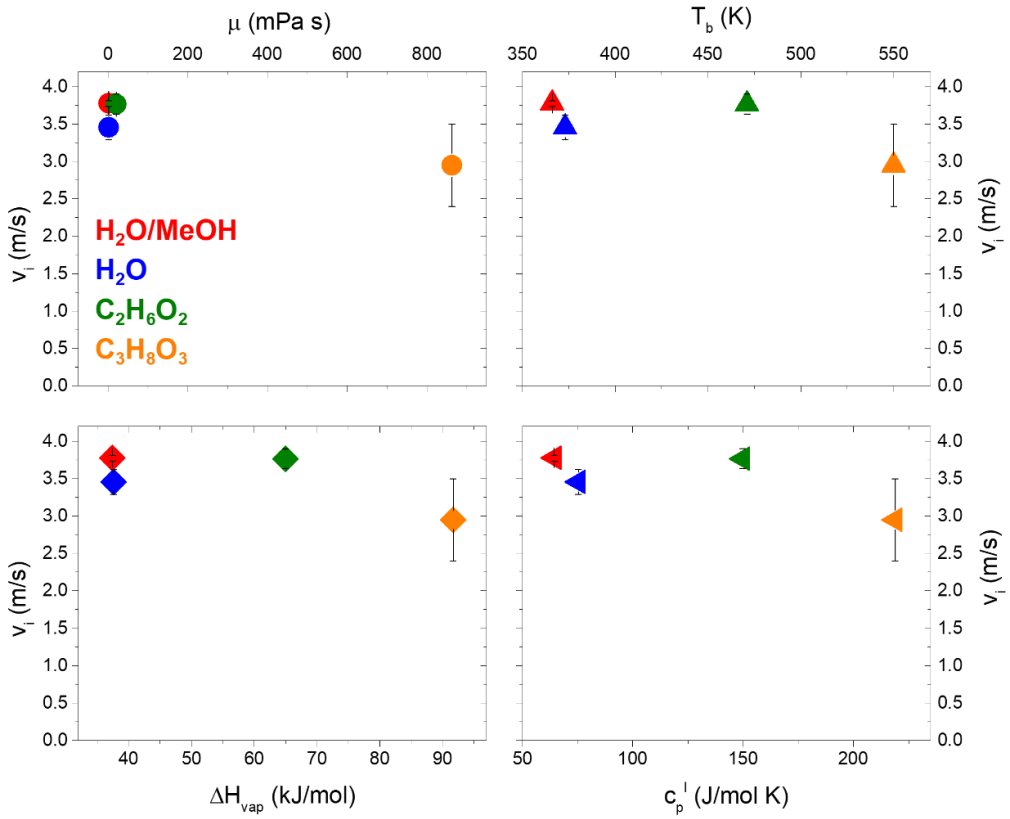

Figure 5.11. The protic solvents, an aqueous mixture of water:methanol 90:10% (H_2O/MeOH, red), water (H_2O, blue), ethylene glycol ($C_2H_6O_2$, green), and glycerol ($C_3H_8O_3$, orange), are plotted against their respective physical constants, viscosity (μ), boiling point (T_b), enthalpy of vaporization (ΔH_{vap}), and heat capacity (c_p^l). This highlights that there is no trend in initial velocity (v_i) on any property of the solvent. The physical constants used in the graph are tabulated in Table 5.1.

All these liquids provide a high density of oxygen atoms, and previous work has shown that these atoms can undergo exothermic reactions with the metal surface to release extra heat.[324] The Al surface is oxidized after using these solvents, as judged by changes in color and reflectivity consistent with the formation of excess Al_2O_3. The alkane liquids, on the other hand, exhibit a clear trend with size, with a factor of 2 decrease in v_i as we go from n-pentane to n-decane. In the absence of oxygen, there is no obvious candidate for an exothermic reaction with Al. The high temperatures achieved do lead to some decomposition of the liquid, as evidenced by the accumulation of black soot on the Al surface, but this coating had no discernible effect on v_i. We conclude that the trend with increasing liquid molecular weight must be the result of differences in physical properties, rather than differences in chemical reactivity.

In order to explain the observed trend in v_i with alkane molecular weight, we develop a simple physical model. From the data in **Figure 5.9**, it is clear that some energy threshold must be achieved to initiate multiphoton absorption and rapid heating of the Al. We consider dynamics after this threshold is reached, when some fraction f of the incoming 1064 nm laser pulse energy is channeled to the liquid contained in a volume V_0 adjacent to the metal plate. This energy heats the liquid from its initial temperature T_i (=298 K) to some final temperature T_f. Given a molar heat capacity C_V, a liquid molar density ρ, and a heat of vaporization ΔH_{vap}, we have

$$f E_{pulse} = \rho V_0 c_v (T_f - T_i) + \rho V_0 \Delta H_{vap} \quad (4)$$

Equation 2 can be rearranged to obtain an expression for T_f.

$$T_f = \frac{1}{\rho V_0 c_v}\left[fE_{pulse} + \rho V_0 c_v T_i - \rho V_0 \Delta H_{vap}\right] \quad (5)$$

We assume that the gas contained in V_0 and heated to T_f can be treated as an ideal gas that undergoes an adiabatic expansion from V_0 at a rate c_{gas}, so the time dependent volume V(t) is given by

$$V(t) = V_0(1 + c_{gas}t^3) \quad (6)$$

Under these conditions, the time-dependent pressure is given by

$$P(t) = \frac{P_0 V_0^\gamma}{V(t)^\gamma} = \frac{nRT_f}{V_0}\frac{V_0^\gamma}{V(t)^\gamma} = \frac{\rho RT_f}{\left(1+c_{gas}t^3\right)^\gamma} \quad (7)$$

where $\gamma = \frac{c_P}{c_v}$ is the usual coefficient for an adiabatic ideal gas expansion. The momentum impulse given by the bubble to the metal plate with mass=m is

$$mv_i \propto \int P(t)dt = \rho RT_f \int \frac{dt}{\left(1+c_{gas}t^3\right)^\gamma} \quad (8)$$

If we further assume that the bubble expansion velocity c_{gas} is the same for all the alkanes, we find

$$v_i \propto \frac{\rho T_f}{m} = \frac{1}{m}\left(\frac{fE_{pulse}}{V_0 c_v} + \rho\left(T_i - \frac{\Delta H_{vap}}{c_v}\right)\right) \quad (9)$$

Note that this model predicts that v_i does not explicitly depend on the liquid boiling point because superheating bypasses this temperature. However, the ΔH_{vap} term depends on the same intermolecular interactions that determine the boiling point, so there is expected to be a correlation with this quantity (**Figure 5.12**). Equation (9) predicts a linear dependence on E_{pulse}, as observed in **Figure 5.9**, providing the first indication that this model is consistent with the data.

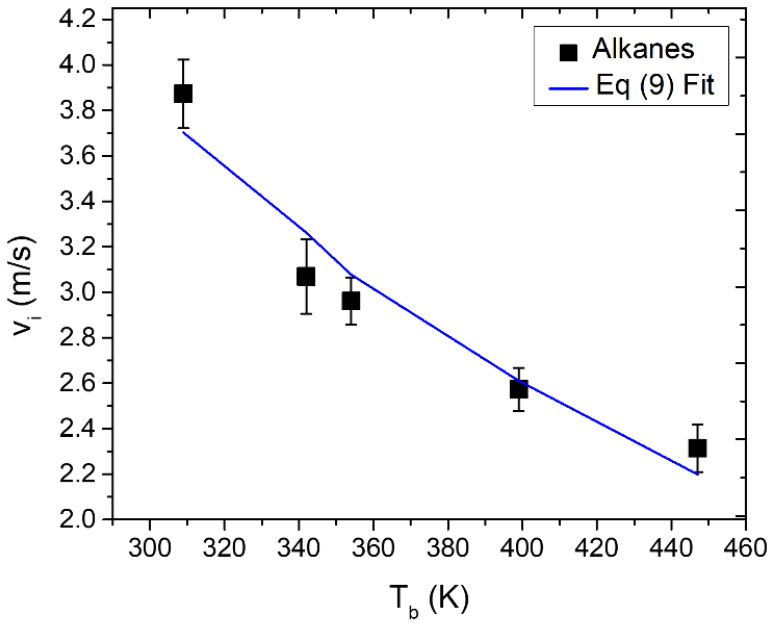

Figure 5.12. v_i values for alkane solvents (black squares from left to right: C_5H_{12}, C_6H_{14}, C_6H_{12}, C_8H_{18}, $C_{10}H_{22}$) are plotted against their respective enthalpy of vaporizations (T_b) The fit is generated from Equation (9), where the parameters for each alkane are given in Table 1. The fvolume of liquid (V_0) was varied to fit the data, resulting in the best fit at V_0=3.4 μL. E_{pulse}= 0.45 J, and the fraction of energy (*f*) was fixed at 1.

However, the model also predicts that v_i should exhibit an m^{-1} dependence. We varied the mass by a factor of 3 and a log-log plot yielded a $m^{-0.6}$ dependence (**Figure 5.13**). It is possible that this mass range is simply not large enough to provide an accurate picture of the mass dependence, but it is also possible that this is a sign that the model is too simplistic. Equation (9) can be scaled by an arbitrary factor to match the alkane v_i data, and the relative role of the E_{pulse} term can be adjusting either *f* or V_0, the volume of the liquid that is superheated. With *f*=1.0, we obtain a good fit to the alkane v_i data by setting V_0=3.4 μL and using the solvent parameters given in **Table 5.2**.

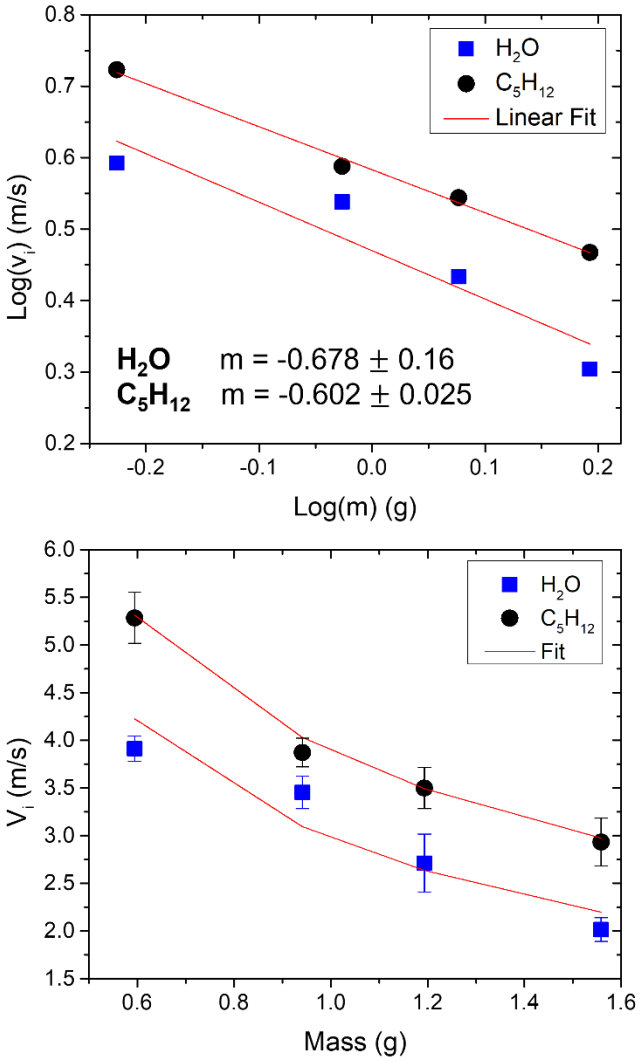

Figure 5.13. The mass of the aluminum (Al) plate was varied from 0.6 g to 1.6 g by changing the height of the plate but keeping the length and width constant. The initial velocity (v_i) was then analyzed for each plate using water (H_2O) and pentane (C_5H_{12}) in a spacer of D=1 mm. (Top) The log of the mass was plotted against the log of the corresponding v_i. A linear fit was done to find the slope of the line which gave a $m^{-0.6}$ dependence with V_i. (Bottom) The mass is plotted against its corresponding v_i with the $m^{-0.6}$ fit determined from the log-log plot. This shows the general trend in increasing mass results in a lower initial velocity.

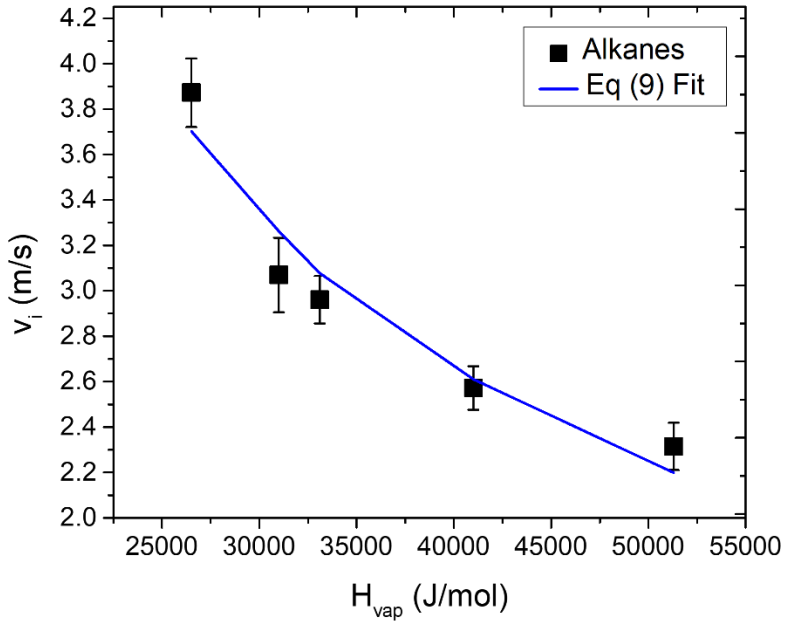

Figure 5.14. v_i values for alkane solvents (black squares from left to right: C_5H_{12}, C_6H_{14}, C_6H_{12}, C_8H_{18}, $C_{10}H_{22}$) are plotted against their respective enthalpy of vaporizations (ΔH_{vap}) The fit is generated from Equation (9), where the parameters for each alkane are given in Table 1. The fvolume of liquid (V_0) was varied to fit the data, resulting in the best fit at V_0=3.4 μL. E_{pulse}= 0.45 J, and the fraction of energy (*f*) was fixed at 1.

This calculated solvent dependence is overlaid with the v_i data in Figure 6. However, this value of V_0 is clearly an overestimate, since 0.45 J is not sufficient to vaporize this volume of pentane given its ΔH_{vap}=26500 J/mol and density ρ=8.73 mol/L. The volume of liquid is probably at least 7× smaller in order to attain a T_f value on the order of 700 K, which is the threshold for alkane carbonization,[339–341] which is observed experimentally. If V_0=0.34 μL, this corresponds to vaporizing liquid to a depth of 5.3 μm, emphasizing the interfacial nature of this phenomenon.

	ρ ($\cdot 10^{-3}$)	c_v^l	ΔH_{vap}	T_i	f	E_{in}	V_0 ($\cdot 10^{-3}$)	T_f
	mol/mL	J/mol K	J/mol	K		J	mL	K
C_5H_{12}	8.73[342]	168.6[343]	26500[333]	298	1	0.445	3.41	229.5
C_6H_{14}	7.66[342]	197.7[344]	31000[333]	298	1	0.445	3.41	227.4
C_6H_{12}	9.27[342]	156.0[345]	33100[333]	298	1	0.445	3.41	176.1
C_8H_{18}	6.13[342]	255.7[346]	41000[333]	298	1	0.445	3.41	220.9
$C_{10}H_{22}$	5.13[342]	315.5[345]	51300[333]	298	1	0.445	3.41	216.0

Table 5.2. The numerical values for each alkane solvent used to generate equation (9) fit to overlay the experimental data in Figure 5.14. The physical constants include molar densities (ρ), isochoric liquid heat capacities (c_v^l), enthalpy of vaporizations (ΔH_{vap}). The initial temperature (T_i), pulse energy (E_{in}), and fraction of pulse energy (f) are all fixed. The volume of liquid vaporized (V_0) was varied to find the best fit with the experimental v_i of each alkane upon overlaying fit line with data. The final temperature (T_f) was calculated using equation (5) to show that the V_0 is largely overestimated from our model. Note: The liquid heat capacities are the same at constant pressure and volume due to the incompressibility of a liquid. The change in volume during heating is negligible.[347]

Even though the model in Equations (4)-(9) can provide a qualitative description for the observed v_i behavior, it is not adequate to provide a quantitative description of the phenomenon. This is not too surprising, given that this model assumes a fixed heated volume V_0, C_V and ΔH_{vap} parameters that are independent of temperature, and ideal gas behavior even at very high (liquid) densities. None of these assumptions is expected to be valid under the conditions of rapid laser heating. Nevertheless, the model does capture the essential behavior within the alkane class of working fluids. It also provides guidance for the choice of working fluid: higher v_i values can be obtained by using high density liquids that can be driven to high T_f values via low C_V and ΔH_{vap} values.

Finally, we turn to the efficiency of the photon-to-kinetic energy transfer, defined as

$$\eta = \frac{\frac{1}{2}mv_i^2}{E_{pulse}} \tag{10}$$

Figure 5.15 plots the efficiencies at E_{pulse}=0.45 J for the alkane solvents and H_2O.

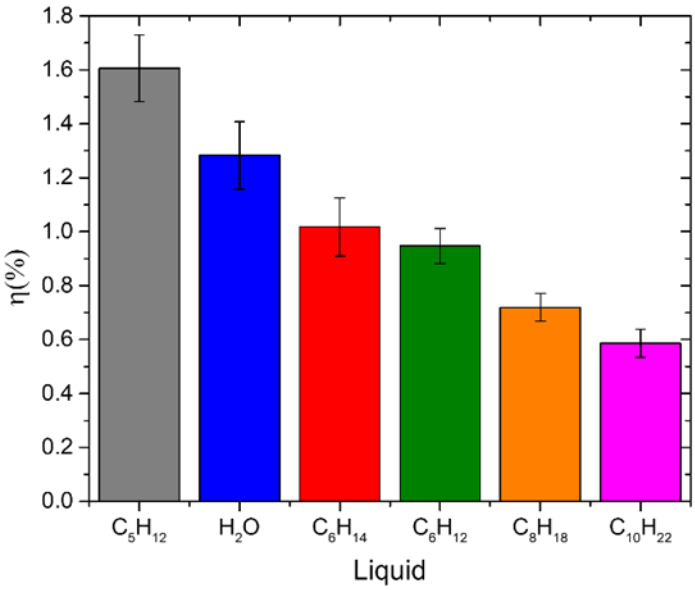

Figure 5.15. The efficiencies (η) of the solvents are compared showing a decrease as alkane chain length increases. H_2O is also shown to compare its efficiency to the alkanes. All samples have a spacer of D=1 mm and are hit with a 0.45 J single pulse.

The η values measured in this work approach 2% and are significantly greater than those reported for resistively heated liquid→gas actuators. We believe that these higher efficiency values result from the much higher temperatures that can be attained through nanosecond laser heating. It has been shown shown that the efficiency of a pulsed laser heat engine, based only on gas expansion, scales with T_f, the final temperature of the heated

gas.[161] Although our system is based on a different liquid→gas expansion, we expect the same physical reasoning to hold.

One advantage of using the metal plate to heat the liquid is that it provides a robust absorbing surface whose performance does not degrade. We found that molecular absorbers, like gold nanoparticles dissolved in the working fluid, tended to rapidly bleach when exposed to high power laser pulses. A second advantage of the metal absorbing surface is that it localizes the heating to a small volume at the interface, even when the total volume of the working fluid is much larger. This localization facilitates the generation of very high temperatures. Of course, in the systems studied here, the high temperature comes at the cost of chemical degradation of the working fluid. Eventually, the working fluid would have to be replaced, which limits the useful lifetime of the actuator. One solution would be to use a chemically inert working fluid, for example liquid xenon, to avoid this problem.

There are some practical challenges to be addressed before a actuator based on nanosecond laser induced liquid→gas expansions could be built. The chemical degradation of the working fluid and transparent substrate have already been described. The design of the actuator presents another challenge. For our experiments, the metal plate was not attached to the working fluid container to facilitate the kinetic energy measurements. To make a practical actuator, a movable top plate would have to be attached to a closed system. Most liquid→gas actuators accomplish this by encapsulating the fluid in an elastic polymer membrane, but the high temperatures achieved by the pulsed laser heating would likely decompose the polymer. A metal bellows design is probably more

appropriate for an actuator based on explosive vaporization, as demonstrated previously for a heated gas actuator.[119,120] A second consideration is that the duty cycle of an actuator based on this principle will be limited by the cooling and condensation of the gas back into liquid form. Since the gas generated in our structures escaped into the surrounding atmosphere, we could not measure this condensation time. The construction of a closed system would bring the added benefit that tis time could also be measured, since condensation would be accompanied by a large volume decrease which could be easily detected.

5.3 Conclusion

This paper applies concepts from the laser flyer field to the area of liquid→gas actuation. We show that explosive boiling induced by nanosecond laser heating of a metal surface can transform light into kinetic energy with efficiencies greater than 1%. A study of how this phenomenon depends on parameters like laser pulse energy, fluid volume, and the chemical structure of the liquid provides information that can be used to optimize actuation based on this type of phase transition. Our simple theoretical analysis suggests that increasing the density of the liquid, decreasing its ΔH_{vap}, and improving heat transfer from the metal to the liquid are all important for improving the energy transfer efficiency. If stable liquids and closed-cycle actuator designs can be found, it is possible that pulsed laser heating may lead to liquid→gas expansion actuators with higher efficiencies and shorter response times.

Chapter 6: Conclusions and Future Outlook

In this dissertation, new strategies for the molecular organization of functional materials have been discovered and enhanced. New systems beyond molecular crystals were examined experimentally and theoretically to provide new avenues for design based on light-driven properties.

First, a systematic study in the development of a reliable way to produce cold molecules led to a generalized method that will be used in the future production of cold polar diatomic molecules. This research focused on mixtures of aluminum and chloride salts but can be applied to other alkali halides of interest. This study is the first of its kind and provides interesting results that contradict what chemical intuition suggests. First, although $AlCl_3$ does produce the largest amount of AlCl after pulsed laser ablation, its hygroscopic nature makes it an unreliable precursor for AlCl production, sometimes giving no yield at all. Second, using pulsed laser ablation to generate AlCl from a mixture of Al : XCl_n, does not depend on any energetics of the precursors, such as bond dissociation energy. The high-energy laser used to ablate the solid can completely dissociate the species into its atomic substituents. So having a robust solid sample that is insensitive to the environment and relatively nonhazardous, like KCl, is more beneficial. Third, in analyzing the AlCl formation, a simple model can quantitatively describe Al + Cl encounters in the gas plume to form AlCl dependent on precursor composition, mixing ratio, and AlCl

recondensation. Most importantly, a high Cl atom density of the XCl_n source was linearly correlated to the production of AlCl.

This work has proven that pulsed laser ablation of Al : XCln provides a reliable way to produce AlCl, without the need for high temperature ovens. This result can be generalizable for the production of other heteronuclear diatomics. Future studies should focus on using a high density of halogen atoms; for example, flowing chlorine gas into a chamber with ablated aluminum atoms. Furthermore, the methods discovered here will lead to quicker formation of the first AlCl optical lattice. Once in an optical lattice, high-resolution gas phase spectroscopy will be done on the lattice as it is tuned with external fields to unlock new fundamental physical theories. While the current status of the project is far from this ultimate goal, this work provided the first steps toward the groundwork of this project.

Due to the long timeline of the AlCl project, I shifted focus to organizing molecules in the condensed phase through covalent bonding. Our collaborators developed a bithiophene trimer that was attached in a cage geometry by aromatic caps. This type of construction limits the flexibility of the molecular orientation leading to less conformational freedom. The novelty of this structure is that it resembles solid-state crystalline structures in terms of its rigidity, unlike the typical floppy bithiophene dendrimers that are studied. This is a huge leap in the progress towards efficient energy harvesting, in linking desired properties to molecular structure. This framework allows for the tuning of properties by changing the molecular capping group holding together the three bithiophenes.

This system was examined in two limits, (1) inert covalent linkers that promote through-space interchromophore interactions, and (2) active covalent linkers that change the electronic states of the chromophores. First, a phenyl capping unit holding together the cage geometry showed the formation of H-type Frenkel excitons that undergo ISC, like normal bithiophene assemblies. By switching the capping unit to an active triazine, a new CT state dominates the electronic properties by outcompeting ISC and increasing the fluorescence output. Not only was the CT state dominant in this molecular organization, but the fact that it gave a long-lived fluorescence output was a surprising benefit. This answered the major question of how assemblies of bithiophenes can be tuned based on molecular structure and chemical components and thus will lead to the future developments of multichromophoric molecules with tunable linkers.

Although there has been much research on examining new excited states through the synthesis of different covalently linked chromophores; this work shows that the same geometry can be precisely tuned by only synthetically changing the linking group. Future studies will now be able to rationally design an assembly of chromophores based on the desired excited state properties and introduce them in a controlled way.

For electronic states, high molecular order is desired. But for mechanical applications, disordered phases like liquids and gases may be more useful. This work provided a proof of concept for a new impulsive laser-powered actuator. A nanosecond laser pulse was used to propel a 1-gram aluminum plate vertically almost 1 meter through the air. By inserting a liquid layer adjacent to the metal, the metal was used as a heat source for explosive boiling of the liquid. The characteristic volume expansion upon gas formation

was optimized with different variables like liquid, pulse energy, volume of liquid, and confinement of liquid. Remarkably, energy conversion from light to kinetic energy efficiencies approached 2%. Furthermore, experiment backed by theoretical analysis showed that decreasing the ΔH_{vap} of the liquid increased the efficiency of the metal propulsion.

This work provides a basis for laser-powered actuators with higher light-to-kinetic energy conversion efficiencies. By using a pulsed laser, the rate of heating occurs fast enough to compete with thermal diffusion. Therefore, less energy is lost through heat diffusion to the surroundings. In theory, the efficiency of the system is correlated to the temperature gradient of the working fluid before and after impulsively heating.[161] This work showed that a pulsed laser is an effective way to increase the temperature change quickly by using an aluminum heat source. This research paves a path towards improved performance with the use of higher energy lasers and a lower ΔH_{vap} liquid.

The development of this system into a real actuator does present challenges, in which an ideal liquid would not decompose upon laser irradiation. Second, the optically clear substrate that the laser pulse enters the system through would need to be more robust than the PMMA used in this work. If these challenges were overcome, this design could lead to improved performance of liquid→gas expansion actuators.

References

(1) Ratner, M. A.; Reed, M. A. Molecular Electronics. In *Encyclopedia of Physical Science and Technology*; Meyers, R. A., Ed.; Academic Press, 2001; pp 123–139.

(2) Radhakrishnan, T. P. Molecules to Materials. *Resonance* **1998**, *3*, 30–42. https://doi.org/10.1007/bf02841419.

(3) Wei, M.; Gao, Y.; Li, X.; Serpe, M. J. Stimuli-Responsive Polymers and Their Applications. *Polym. Chem.* **2017**, *8* (1), 127–143. https://doi.org/10.1039/c6py01585a.

(4) Bohn, J. L.; Rey, A. M.; Ye, J. Cold Molecules: Progress in Quantum Engineering of Chemistry and Quantum Matter. *Science (80-.).* **2017**, *357* (6355), 1002–1010. https://doi.org/10.1126/science.aam6299.

(5) de Leon, N. P.; Itoh, K. M.; Kim, D.; Mehta, K. K.; Northup, T. E.; Paik, H.; Palmer, B. S.; Samarth, N.; Sangtawesin, S.; Steuerman, D. W. Materials Challenges and Opportunities for Quantum Computing Hardware. *Science (80-.).* **2021**, *372* (253), 1–19. https://doi.org/10.1126/science.abb2823.

(6) Liu, H.; Low, G. H.; Steiger, D. S.; Häner, T.; Reiher, M.; Troyer, M. Prospects of Quantum Computing for Molecular Sciences. *Mater. Theory* **2022**, *6* (11), 1–17. https://doi.org/10.1186/s41313-021-00039-z.

(7) Liu, X.; Hersam, M. C. 2D Materials for Quantum Information Science. *Nat. Rev. Mater.* **2019**, *4* (10), 669–684. https://doi.org/10.1038/s41578-019-0136-x.

(8) Friedrich, B.; Doyle, J. M. Why Are Cold Molecules so Hot? *ChemPhysChem* **2009**, *10* (4), 604–623. https://doi.org/10.1002/cphc.200800577.

(9) Schnell, M.; Meijer, G. Cold Molecules: Preparation, Applications, and Challenges. *Angew. Chemie - Int. Ed.* **2009**, *48* (33), 6010–6031. https://doi.org/10.1002/anie.200805503.

(10) Kondo, M. Photomechanical Materials Driven by Photoisomerization or Photodimerization. *Polym. J.* **2020**, *52* (9), 1027–1034. https://doi.org/10.1038/s41428-020-0367-0.

(11) Guiton, B. S.; Stefik, M.; Augustyn, V.; Banerjee, S.; Bardeen, C. J.; Bartlett, B. M.; Li, J.; López-Mejías, V.; Macgillivray, L. R.; Morris, A.; Rodriguez, E. E.; Samia, A. C. S.; Sun, H.; Sutter, P.; Talham, D. R. Frontiers in Hybrid and Interfacial Materials Chemistry Research. *MRS Bull.* **2020**, *45* (11), 951–964. https://doi.org/10.1557/mrs.2020.271.

(12) Irie, M.; Fukaminato, T.; Matsuda, K.; Kobatake, S. Photochromism of Diarylethene Molecules and Crystals: Memories, Switches, and Actuators. *Chem. Rev.* **2014**, *114* (24), 12174–12277. https://doi.org/10.1021/cr500249p.

(13) Naumov, P.; Chizhik, S.; Panda, M. K.; Nath, N. K.; Boldyreva, E. Mechanically Responsive Molecular Crystals. *Chem. Rev.* **2015**, *115* (22), 12440–12490. https://doi.org/10.1021/acs.chemrev.5b00398.

(14) Dong, L.; Zhao, Y. Photothermally Driven Liquid Crystal Polymer Actuators. *Mater. Chem. Front.* **2018**, *2* (11), 1932–1943. https://doi.org/10.1039/c8qm00363g.

(15) Chen, Y.; Yang, J.; Zhang, X.; Feng, Y.; Zeng, H.; Wang, L.; Feng, W. Light-Driven Bimorph Soft Actuators: Design, Fabrication, and Properties. *Mater. Horizons* **2021**, *8* (3), 728–757. https://doi.org/10.1039/d0mh01406k.

(16) Hains, A. W.; Liang, Z.; Woodhouse, M. A.; Gregg, B. A. Molecular Semiconductors in Organic Photovoltaic Cells. *Chem. Rev.* **2010**, *110* (11), 6689–6735. https://doi.org/10.1021/cr9002984.

(17) Menke, S. M.; Holmes, R. J. Exciton Diffusion in Organic Photovoltaic Cells. *Energy Environ. Sci.* **2014**, *7* (2), 499–512. https://doi.org/10.1039/c3ee42444h.

(18) Rubner, R. Photoreactive Polymers for Electronics. *Adv. Mater.* **1990**, *2* (10), 452–457. https://doi.org/10.1002/adma.19900021003.

(19) Yu, J.; Zheng, Y.; Huang, J. Towards High Performance Organic Photovoltaic Cells: A Review of Recent Development in Organic Photovoltaics. *Polymers (Basel).* **2014**, *6* (9), 2473–2509. https://doi.org/10.3390/polym6092473.

(20) Chen, S.; Deng, L.; Xie, J.; Peng, L.; Xie, L.; Fan, Q.; Huang, W. Recent Developments in Top-Emitting Organic Light-Emitting Diodes. *Adv. Mater.* **2010**, *22* (46), 5227–5239. https://doi.org/10.1002/adma.201001167.

(21) Geffroy, B.; le Roy, P.; Prat, C. Organic Light-Emitting Diode (OLED) Technology: Materials, Devices and Display Technologies. *Polym. Int.* **2006**, *55* (6), 572–582. https://doi.org/10.1002/pi.1974.

(22) Song, J.; Lee, H.; Jeong, E. G.; Choi, K. C.; Yoo, S. Organic Light-Emitting Diodes: Pushing Toward the Limits and Beyond. *Adv. Mater.* **2020**, *32* (35), 1–17. https://doi.org/10.1002/adma.201907539.

(23) Yook, K. S.; Lee, J. Y. Organic Materials for Deep Blue Phosphorescent Organic Light-Emitting Diodes. *Adv. Mater.* **2012**, *24*, 3169–3190. https://doi.org/10.1002/adma.201200627.

(24) Alahakoon, S. B.; Thompson, C. M.; Occhialini, G.; Smaldone, R. A. Design Principles for Covalent Organic Frameworks in Energy Storage Applications. *ChemSusChem* **2017**, *10* (10), 2116–2129. https://doi.org/10.1002/cssc.201700120.

(25) Fallahi, A.; Guldentops, G.; Tao, M.; Granados-Focil, S.; Van Dessel, S. Review on Solid-Solid Phase Change Materials for Thermal Energy Storage: Molecular Structure and Thermal Properties. *Appl. Therm. Eng.* **2017**, *127*, 1427–1441.

https://doi.org/10.1016/j.applthermaleng.2017.08.161.

(26) Liu, C.; Li, F.; Lai-Peng, M.; Cheng, H. M. Advanced Materials for Energy Storage. *Adv. Mater.* **2010**, *22* (8), 28–62. https://doi.org/10.1002/adma.200903328.

(27) Schon, T. B.; McAllister, B. T.; Li, P. F.; Seferos, D. S. The Rise of Organic Electrode Materials for Energy Storage. *Chem. Soc. Rev.* **2016**, *45* (22), 6345–6404. https://doi.org/10.1039/c6cs00173d.

(28) Umair, M. M.; Zhang, Y.; Iqbal, K.; Zhang, S.; Tang, B. Novel Strategies and Supporting Materials Applied to Shape-Stabilize Organic Phase Change Materials for Thermal Energy Storage–A Review. *Appl. Energy* **2019**, *235*, 846–873. https://doi.org/10.1016/j.apenergy.2018.11.017.

(29) Zhou, Y.; Wu, S.; Ma, Y.; Zhang, H.; Zeng, X.; Wu, F.; Liu, F.; Ryu, J. E.; Guo, Z. Recent Advances in Organic/Composite Phase Change Materials for Energy Storage. *ES Energy Environ.* **2020**, *9*, 28–40. https://doi.org/10.30919/esee8c150.

(30) Lundblad, N. Designer Atom Arrays for Quantum Computing. *Nature* **2018**, *561* (7721), 43–44. https://doi.org/10.1038/d41586-018-06107-8.

(31) Yu, P.; Cheuk, L. W.; Kozyryev, I.; Doyle, J. M. A Scalable Quantum Computing Platform Using Symmetric-Top Molecules. *New J. Phys.* **2019**, *21* (9). https://doi.org/10.1088/1367-2630/ab428d.

(32) Maxwell, J. C. II. Illustrations of the Dynamical Theory of Gases . *London, Edinburgh, Dublin Philos. Mag. J. Sci.* **1860**, *20* (130), 21–37. https://doi.org/10.1080/14786446008642902.

(33) Hansch, T. W.; Schawlow, A. L. Cooling of Gases by Laser Radiation. *Opt. Commun.* **1975**, *13* (I), 68–69. https://doi.org/10.1016/0030-4018(75)90159-5.

(34) Ashkin, A. Trapping of Atoms by Resonance Radiation Pressure. *Phys. Rev. Lett.* **1978**, *40* (12), 729–732. https://doi.org/10.1103/PhysRevLett.40.729.

(35) Condon, E. A Theory of Intensity Distribution in Band Systems. *Phys. Rev.* **1926**, *28* (6), 1182–1201. https://doi.org/10.1103/PhysRev.28.1182.

(36) Davis, K. B.; Mewes, M. O.; Andrews, M. R.; van Druten, N. J.; Durfee, D. S.; Kurn, D. M.; Ketterle, W. Bose-Einstein Condensation in a Gas of Sodium Atoms. *Phys. Rev. Lett.* **1995**, *75* (22), 3969–3974. https://doi.org/10.1103/PhysRevLett.75.3969.

(37) Anderson, M. H.; Ensher, J. R.; Matthews, M. R.; Wieman, C. E.; Cornell, A. E. Observation of Bose-Einstein Condensation in a Dilute Atomic Vapor. *Science (80-.).* **1995**, *269* (5221), 198–201. https://doi.org/10.1126/science.269.5221.198.

(38) Zhang, Z.; Chen, L.; Yao, K. X.; Chin, C. Transition from an Atomic to a

Molecular Bose–Einstein Condensate. *Nature* **2021**, *592* (7856), 708–711. https://doi.org/10.1038/s41586-021-03443-0.

(39) Krems, R. V. Cold Controlled Chemistry. *Phys. Chem. Chem. Phys.* **2008**, *10* (28), 4079–4092. https://doi.org/10.1039/b802322k.

(40) Carr, L. D.; DeMille, D.; Krems, R. V.; Ye, J. Cold and Ultracold Molecules: Science, Technology and Applications. *New J. Phys.* **2009**, *11*, 1–87. https://doi.org/10.1088/1367-2630/11/5/055049.

(41) Moses, S. A.; Covey, J. P.; Miecnikowski, M. T.; Yan, B.; Gadway, B.; Ye, J.; Jin, D. S. Creation of a Low-Entropy Quantum Gas of Polar Molecules in an Optical Lattice. *Science (80-.).* **2015**, *350* (6261), 659–662. https://doi.org/10.1126/science.aac6400.

(42) Prodan, J. V.; Phillips, W. D.; Metcalf, H. Laser Production of a Very Slow Monoenergetic Atomic Beam. *Phys. Rev. Lett.* **1982**, *49* (16), 1149–1153. https://doi.org/10.1103/PhysRevLett.49.1149.

(43) Chu, S.; Hollberg, L.; Bjorkholm, J. E.; Cable, A.; Ashkin, A. Three-Dimensional Viscous Confinement and Cooling of Atoms by Resonance Radiation Pressure. *Phys. Rev. Lett.* **1985**, *55* (1), 48–51. https://doi.org/10.1103/PhysRevLett.55.48.

(44) Aspect, A.; Arimondo, E.; Kaiser, R.; Vansteenkiste, N.; Cohen-Tannoudji, C. Laser Cooling Below the One-Photon Recoil Energy by Velocity-Selective Coherent Population Trapping. *Phys. Rev. Lett.* **1989**, *61* (7), 826–829. https://doi.org/10.1103/PhysRevLett.62.2487.

(45) Lett, P. D.; Helmerson, K.; Phillips, W. D.; Ratliff, L. P.; Rolston, S. L.; Wagshul, M. E. Spectroscopy of Na2 by Photoassociation of Laser-Cooled Na. *Phys. Rev. Lett.* **1993**, *71* (14), 2200–2203. https://doi.org/10.1103/PhysRevLett.71.2200.

(46) Miller, J. D.; Cline, R. A.; Heinzen, J. Photoassociation Spectrum of Ultracold Rb Atoms. *Phys. Rev. Lett.* **1993**, *71* (14), 2204–2207. https://doi.org/10.1103/PhysRevLett.71.2204.

(47) Anderegg, L.; Augenbraun, B. L.; Chae, E.; Hemmerling, B.; Hutzler, N. R.; Ravi, A.; Collopy, A.; Ye, J.; Ketterle, W.; Doyle, J. M. Radio Frequency Magneto-Optical Trapping of CaF with High Density. *Phys. Rev. Lett.* **2017**, *119* (10), 1–5. https://doi.org/10.1103/PhysRevLett.119.103201.

(48) Truppe, S.; Williams, H. J.; Hambach, M.; Caldwell, L.; Fitch, N. J.; Hinds, E. A.; Sauer, B. E.; Tarbutt, M. R. Molecules Cooled below the Doppler Limit. *Nat. Phys.* **2017**, *13* (12), 1173–1176. https://doi.org/10.1038/nphys4241.

(49) Williams, H. J.; Truppe, S.; Hambach, M.; Caldwell, L.; Fitch, N. J.; Hinds, E. A.; Sauer, B. E.; Tarbutt, M. R. Characteristics of a Magneto-Optical Trap of Molecules. *New J. Phys.* **2017**, *19* (113035), 1–19. https://doi.org/10.1088/1367-

2630/aa8e52.

(50) Collopy, A. L.; Ding, S.; Wu, Y.; Finneran, I. A.; Anderegg, L.; Augenbraun, B. L.; Doyle, J. M.; Ye, J. 3D Magneto-Optical Trap of Yttrium Monoxide. *Phys. Rev. Lett.* **2018**, *121* (213201), 1–5. https://doi.org/10.1103/PhysRevLett.121.213201.

(51) Di Rosa, M. D. Laser-Cooling Molecules: Concept, Candidates, and Supporting Hyperfine-Resolved Measurements of Rotational Lines in the A-X(0,0) Band of CaH. *Eur. Phys. J. D* **2004**, *31* (2), 395–402. https://doi.org/10.1140/epjd/e2004-00167-2.

(52) Yang, R.; Tang, B.; Gao, T. Ab Initio Study on the Electronic States and Laser Cooling of AlCl and AlBr. *Chinese Phys. B* **2016**, *25* (043101), 1–6. https://doi.org/10.1088/1674-1056/25/4/043101.

(53) Wan, M.; Yuan, D.; Jin, C.; Wang, F.; Yang, Y.; Yu, Y.; Shao, J. Laser Cooling of the AlCl Molecule with a Three-Electronic-Level Theoretical Model. *J. Chem. Phys.* **2016**, *145* (024309), 1–7. https://doi.org/10.1063/1.4955498.

(54) Ren, X. Y.; Xiao, Z. Y.; Liu, Y.; Yan, B. Configuration Interaction Study on Low-Lying States of AlCl Molecule. *Chinese Phys. B* **2021**, *30* (5), 1–8. https://doi.org/10.1088/1674-1056/abd46a.

(55) Langhoff, S. R.; Bauschlicher, C. W.; Taylor, P. R. Theoretical Studies of AlF, AlCl, and AlBr. *J. Chem. Phys.* **1988**, *88* (9), 5715–5725. https://doi.org/10.1063/1.454531.

(56) Bhaduri, B. N.; Fowler, A. Band Spectrum of Aluminum Chloride (AlCl). *Proc. Roy. Soc.* **1934**, *145* (8), 335–336. https://doi.org/10.1038/133496a0.

(57) Sharma, D. Two New Band Systems of the AlCl Molecule. *Am. Astron. Soc.* **1950**, *113*, 210–218. https://doi.org/10.1086/145389.

(58) Tsunoda, K. I.; Fujiwara, K.; Fuwa, K. Determination of Chlorine and Bromine by Molecular Absorption of Aluminum Monohalides at High Temperature. *Anal. Chem.* **1978**, *50* (7), 861–865. https://doi.org/10.1021/ac50029a011.

(59) Ram, R. S.; Rai, S. B.; Upadhya, K. N.; Rai, D. K. The A1Π-X1Σ+, A3Π-X1Σ+ and B3Σ+-A3Π Systems of AlCl. *Phys. Scr.* **1982**, *26*, 383–397. https://doi.org/10.1088/0031-8949/26/5/007.

(60) Mahieu, E.; Dubois, I.; Bredohl, H. The A1Π-X1Σ+ Transition of AlCl. *J. Mol. Spectrosc.* **1989**, *134* (2), 317–328. https://doi.org/10.1016/0022-2852(89)90319-6.

(61) Mahieu, E.; Dubois, I.; Bredohl, H. The Triplet States of AlCl. *J. Mol. Spectrosc.* **1989**, *138* (1), 264–271. https://doi.org/10.1016/0022-2852(89)90116-1.

(62) Futerko, P. M.; Fontijn, A. Experimental and Transition-State Theory Studies of

the Gas-Phase Reactions of AlCl with N2O, CO2, and SO2. *J. Phys. Chem.* **1993**, *97*, 7222–7227. https://doi.org/10.1021/j100130a016.

(63) Saksena, M. D.; Dixit, V. S.; Singh, M. Rotational Analysis of the 0-0 Band of the a 3Π-X1Σ+ Transition of AlCl. *J. Mol. Spectrosc.* **1998**, *187* (1), 1–5. https://doi.org/10.1006/jmsp.1997.7442.

(64) Hutzler, N. R.; Lu, H. I.; Doyle, J. M. The Buffer Gas Beam: An Intense, Cold, and Slow Source for Atoms and Molecules. *Chem. Rev.* **2012**, *112* (9), 4803–4827. https://doi.org/10.1021/cr200362u.

(65) Daniel, J. R.; Wang, C.; Rodriguez, K.; Hemmerling, B.; Lewis, T. N.; Bardeen, C.; Teplukhin, A.; Kendrick, B. K. Spectroscopy on the A Π 1 ←x ς + 1 Transition of Buffer-Gas-Cooled AlCl. *Phys. Rev. A* **2021**, *104* (1), 1–13. https://doi.org/10.1103/PhysRevA.104.012801.

(66) Kousksou, T.; Bruel, P.; Jamil, A.; El Rhafiki, T.; Zeraouli, Y. Energy Storage: Applications and Challenges. *Sol. Energy Mater. Sol. Cells* **2014**, *120* (PART A), 59–80. https://doi.org/10.1016/j.solmat.2013.08.015.

(67) Energy, D. of. Top 6 Things You Didn't Know About Solar Energy. *energy.gov*. 2016. https://www.energy.gov/articles/top-6-things-you-didnt-know-about-solar-energy.

(68) Zhang, L.; Colella, N. S.; Cherniawski, B. P.; Mannsfeld, S. C. B.; Briseno, A. L. Oligothiophene Semiconductors: Synthesis, Characterization, and Applications for Organic Devices. *ACS Appl. Mater. Interfaces* **2014**, *6* (8), 5327–5343. https://doi.org/10.1021/am4060468.

(69) Brédas, J. L.; Beljonne, D.; Coropceanu, V.; Cornil, J. Charge-Transfer and Energy-Transfer Processes in π-Conjugated Oligomers and Polymers: A Molecular Picture. *Chem. Rev.* **2004**, *104* (11), 4971–5003. https://doi.org/10.1021/cr040084k.

(70) Frenkel, J. On the Transformation of Light into Heat in Solids. I. *Phys. Rev.* **1931**, *37* (1), 17–44. https://doi.org/10.1103/PhysRev.37.17.

(71) Hestand, N. J.; Spano, F. C. Expanded Theory of H- and J-Molecular Aggregates: The Effects of Vibronic Coupling and Intermolecular Charge Transfer. *Chem. Rev.* **2018**, *118* (15), 7069–7163. https://doi.org/10.1021/acs.chemrev.7b00581.

(72) Hutchison, G. R.; Ratner, M. A.; Marks, T. J. Intermolecular Charge Transfer between Heterocyclic Oligomers. Effects of Heteroatom and Molecular Packing on Hopping Transport in Organic Semiconductors. *J. Am. Chem. Soc.* **2005**, *127* (48), 16866–16881. https://doi.org/10.1021/ja0533996.

(73) Sarma, M.; Wong, K. T. Exciplex: An Intermolecular Charge-Transfer Approach for TADF. *ACS Appl. Mater. Interfaces* **2018**, *10* (23), 19279–19304.

https://doi.org/10.1021/acsami.7b18318.

(74) Margulies, E. A.; Miller, C. E.; Wu, Y.; Ma, L.; Schatz, G. C.; Young, R. M.; Wasielewski, M. R. Enabling Singlet Fission by Controlling Intramolecular Charge Transfer in π-Stacked Covalent Terrylenediimide Dimers. *Nat. Chem.* **2016**, *8* (12), 1120–1125. https://doi.org/10.1038/nchem.2589.

(75) Rupert, B. L.; Mitchell, W. J.; Ferguson, A. J.; Köse, M. E.; Rance, W. L.; Rumbles, G.; Ginley, D. S.; Shaheen, S. E.; Kopidakis, N. Low-Bandgap Thiophene Dendrimers for Improved Light Harvesting. *J. Mater. Chem.* **2009**, *19* (30), 5311–5324. https://doi.org/10.1039/b903427g.

(76) Johnson, J. C.; Akdag, A.; Zamadar, M.; Chen, X.; Schwerin, A. F.; Paci, I.; Smith, M. B.; Havlas, Z.; Miller, J. R.; Ratner, M. A.; Nozik, A. J.; Michl, J. Toward Designed Singlet Fission: Solution Photophysics of Two Indirectly Coupled Covalent Dimers of 1,3-Diphenylisobenzofuran. *J. Phys. Chem. B* **2013**, *117* (16), 4680–4695. https://doi.org/10.1021/jp310979q.

(77) Whited, M. T.; Patel, N. M.; Roberts, S. T.; Allen, K.; Djurovich, P. I.; Bradforth, S. E.; Thompson, M. E. Symmetry-Breaking Intramolecular Charge Transfer in the Excited State of Meso-Linked BODIPY Dyads. *Chem. Commun.* **2012**, *48* (2), 284–286. https://doi.org/10.1039/c1cc12260f.

(78) Pandolfi, F.; Rocco, D.; Mattiello, L. Synthesis and Characterization of New D-π-A and A-π-D-π-A Type Oligothiophene Derivatives. *Org. Biomol. Chem.* **2019**, *17* (11), 3018–3025. https://doi.org/10.1039/c8ob03077d.

(79) Lewis, T.; Tonnelé, C.; Shuler, W.; Kasun, Z.; Sato, H.; Berges, A.; Rodriguez, J.; Krische, M.; Casanova, D.; Bardeen, C. Chemical Tuning of Exciton versus Charge-Transfer Excited States in Conformationally Restricted Arylene Cages. *J. Am. Chem. Soc.* **2021**, *143* (44), 18548–18558. https://doi.org/10.1021/jacs.1c08176.

(80) B. Nielsen, C.; Angerhofer, A.; A. Abboud, K.; R. Reynolds, J. Discrete Photopatternable π-Conjugated Oligomers for Electrochromic Devices. *J. Am. Chem. Soc.* **2008**, *130* (30), 9734–9746. https://doi.org/10.1021/ja7112273.

(81) Fischer, M. K. R.; Kaiser, T. E.; Würthner, F.; Bäuerle, P. Dendritic Oligothiophene-Perylene Bisimide Hybrids: Synthesis, Optical and Electrochemical Properties. *J. Mater. Chem.* **2009**, *19* (8), 1129–1141. https://doi.org/10.1039/b817158k.

(82) Mishra, A.; Ma, C. Q.; Janssen, R. A. J.; Bäuerle, P. Shape-Persistent Oligothienylene-Ethynylene-Based Dendrimers: Synthesis, Spectroscopy and Electrochemical Characterization. *Chem. - A Eur. J.* **2009**, *15* (48), 13521–13534. https://doi.org/10.1002/chem.200901242.

(83) E. Köse, M.; J. Mitchell, W.; Kopidakis, N.; H. Chang, C.; E. Shaheen, S.; Kim,

K.; Rumbles, G. Theoretical Studies on Conjugated Phenyl-Cored Thiophene Dendrimers for Photovoltaic Applications. *J. Am. Chem. Soc.* **2007**, *129* (46), 14257–14270. https://doi.org/10.1021/ja073455y.

(84) Lukevics, E.; Arsenyan, P.; Belyakov, S.; Popelis, J.; Pudova, O. Cycloaddition Reactions of Nitrile Oxides to 2,4-Silyl- and Germyl-Substituted Thiophene-1,1-Dioxides. *Organometallics* **2001**, *20* (12), 2487–2491. https://doi.org/10.1021/om0100885.

(85) Teran, N. B.; He, G. S.; Baev, A.; Shi, Y.; Swihart, M. T.; Prasad, P. N.; Marks, T. J.; Reynolds, J. R. Twisted Thiophene-Based Chromophores with Enhanced Intramolecular Charge Transfer for Cooperative Amplification of Third-Order Optical Nonlinearity. *J. Am. Chem. Soc.* **2016**, *138* (22), 6975–6984. https://doi.org/10.1021/jacs.5b12457.

(86) Rance, W. L.; Rupert, B. L.; Mitchell, W. J.; Köse, M. E.; Ginley, D. S.; Shaheen, S. E.; Rumbles, G.; Kopidakis, N. Conjugated Thiophene Dendrimer with an Electron-Withdrawing Core and Electron-Rich Dendrons: How the Molecular Structure Affects the Morphology and Performance of Dendrimer:Fullerene Photovoltaic Devices. *J. Phys. Chem. C* **2010**, *114* (50), 22269–22276. https://doi.org/10.1021/jp106850f.

(87) De Melo, J. S.; Burrows, H. D.; Svensson, M.; Andersson, M. R.; Monkman, A. P. Photophysics of Thiophene Based Polymers in Solution: The Role of Nonradiative Decay Processes. *J. Chem. Phys.* **2003**, *118* (3), 1550–1556. https://doi.org/10.1063/1.1528604.

(88) Zhou, Z. hua; Yamamoto, T. Research on Carbon-Carbon Coupling Reactions of Haloaromatic Compounds Mediated by Zerovalent Nickel Complexes. Preparation of Cyclic Oligomers of Thiophene and Benzene and Stable Anthrylnickel(II) Complexes. *J. Organomet. Chem.* **1991**, *414* (1), 119–127. https://doi.org/10.1016/0022-328X(91)83247-2.

(89) Petrella, A.; Cremer, J.; De Cola, L.; Bäuerle, P.; M. Williams, R. Charge Transfer Processes in Conjugated Triarylamine−Oligothiophene−Perylenemonoimide Dendrimers. *J. Phys. Chem. A* **2005**, *109* (51), 11687–11695. https://doi.org/10.1021/jp0510995.

(90) Miyake, Y.; Wu, M.; Jalilur Rahman, M.; Kuwatani, Y.; Iyoda, M. Efficient Construction of Biaryls and Macrocyclic Cyclophanes via Electron-Transfer Oxidation of Lipshutz Cuprates. *J. Org. Chem.* **2006**, *71* (16), 6110–6117. https://doi.org/10.1021/jo0608063.

(91) Lu, X.; Fan, S.; Wu, J.; Jia, X.; Wang, Z. S.; Zhou, G. Controlling the Charge Transfer in D-A-D Chromophores Based on Pyrazine Derivatives. *J. Org. Chem.* **2014**, *79* (14), 6480–6489. https://doi.org/10.1021/jo500856k.

(92) Kulhánek, J.; Bureš, F.; Pytela, O.; Mikysek, T.; Ludvík, J. Imidazole as a

Donor/Acceptor Unit in Charge-Transfer Chromophores with Extended π-Linkers. *Chem. - An Asian J.* **2011**, *6* (6), 1604–1612. https://doi.org/10.1002/asia.201100097.

(93) Aboubakr, H.; Praveen, C.; Malytskyi, V.; Sawadogo, R.; Sotiropoulos, J. M.; Belec, L.; Brisset, H.; Raimundo, J. M. D/A Cruciform Bithiophene Chromophores as Potential Molecular Scaffolds for Optoelectronic Applications. *Tetrahedron* **2016**, *72* (10), 1381–1386. https://doi.org/10.1016/j.tet.2016.01.038.

(94) Tsuge, A.; Hara, T.; Moriguchi, T.; Yamaji, M. Preparation, Structure, and Spectral Properties of Cyclophanes Consisting of Oligothiophene Units. *Chem. Lett.* **2008**, *37* (8), 870–871. https://doi.org/10.1246/cl.2008.870.

(95) S. Becker, R.; Seixas de Melo, J.; L. Maçanita, A.; Elisei, F. Comprehensive Evaluation of the Absorption, Photophysical, Energy Transfer, Structural, and Theoretical Properties of α-Oligothiophenes with One to Seven Rings. *J. Phys. Chem.* **1996**, *100* (48), 18683–18695. https://doi.org/10.1021/jp960852e.

(96) Zhang, J.; Fischer, M. K. R.; Bäuerle, P.; Goodson, T. Energy Migration in Dendritic Oligothiophene-Perylene Bisimides. *J. Phys. Chem. B* **2013**, *117* (16), 4204–4215. https://doi.org/10.1021/jp302772y.

(97) F. Wong, K.; Bagchi, B.; J. Rossky, P. Distance and Orientation Dependence of Excitation Transfer Rates in Conjugated Systems: Beyond the Förster Theory. *J. Phys. Chem. A* **2004**, *108* (27), 5752–5763. https://doi.org/10.1021/jp037724s.

(98) Duan, T.; Chen, Q.; Hu, D.; Lv, J.; Yu, D.; Li, G.; Lu, S. Oligothiophene-Based Photovoltaic Materials for Organic Solar Cells: Rise, Plateau, and Revival. *Trends Chem.* **2022**, *4* (9), 773–791. https://doi.org/10.1016/j.trechm.2022.06.007.

(99) Sato, H.; A. Bender, J.; T. Roberts, S.; J. Krische, M. Helical Rod-like Phenylene Cages via Ruthenium Catalyzed Diol-Diene Benzannulation: A Cord of Three Strands. *J. Am. Chem. Soc.* **2018**, *140* (7), 2455–2459. https://doi.org/10.1021/jacs.8b00131.

(100) Zhang, Y.; Wang, Z.; Ng, M.-K.; J. Rothberg, L. Conformational Reorganization and Solvation Dynamics of Dendritic Oligothiophenes. *J. Phys. Chem. B* **2007**, *111* (46), 13211–13216. https://doi.org/10.1021/jp077564a.

(101) Beljonne, D.; Cornil, J.; H. Friend, R.; A. J. Janssen, R.; L. Brédas, J. Influence of Chain Length and Derivatization on the Lowest Singlet and Triplet States and Intersystem Crossing in Oligothiophenes. *J. Am. Chem. Soc.* **1996**, *118* (27), 6453–6461. https://doi.org/10.1021/ja9531135.

(102) Rossi, R.; Ciofalo, M.; Carpita, A.; Ponterini, G. Singlet-Triplet Intersystem Crossing in 2,2′:5′,2″-Terthiophene and Some of Its Derivatives. *J. Photochem. Photobiol. A Chem.* **1993**, *70* (1), 59–67. https://doi.org/10.1016/1010-6030(93)80009-X.

(103) White, T. J. *Photomechanical Materials, Composites, and Systems*, 1st ed.; Wiley: Hoboken, New Jersey, 2017.

(104) Kuroki, L.; Takami, S.; Yoza, K.; Morimoto, M.; Irie, M. Photoinduced Shape Changes of Diarylethene Single Crystals: Correlation between Shape Changes and Molecular Packing. *Photochem. Photobiol. Sci.* **2010**, *9* (2), 221–225. https://doi.org/10.1039/b9pp00093c.

(105) Morimoto, M.; Irie, M. A Diarylethene Cocrystal That Converts Light into Mechanical Work. *J. Am. Chem. Soc.* **2010**, *132* (40), 14172–14178. https://doi.org/10.1021/ja105356w.

(106) Tong, F.; Kitagawa, D.; Dong, X.; Kobatake, S.; Bardeen, C. J. Photomechanical Motion of Diarylethene Molecular Crystal Nanowires. *Nanoscale* **2018**, *10* (7), 3393–3398. https://doi.org/10.1039/c7nr09571f.

(107) Dong, X.; Tong, F.; Hanson, K. M.; Al-Kaysi, R. O.; Kitagawa, D.; Kobatake, S.; Bardeen, C. J. Hybrid Organic-Inorganic Photon-Powered Actuators Based on Aligned Diarylethene Nanocrystals. *Chem. Mater.* **2019**, *31* (3), 1016–1022. https://doi.org/10.1021/acs.chemmater.8b04568.

(108) Kim, T.; Zhu, L.; Al-Kaysi, R. O.; Bardeen, C. J. Organic Photomechanical Materials. *ChemPhysChem* **2014**, *15* (3), 400–414. https://doi.org/10.1002/cphc.201300906.

(109) Kitagawa, D.; Tsujioka, H.; Tong, F.; Dong, X.; Bardeen, C. J.; Kobatake, S. Control of Photomechanical Crystal Twisting by Illumination Direction. *J. Am. Chem. Soc.* **2018**, *140* (12), 4208–4212. https://doi.org/10.1021/jacs.7b13605.

(110) Dong, X.; Guo, T.; Kitagawa, D.; Kobatake, S.; Palffy-Muhoray, P.; Bardeen, C. J. Effects of Template and Molecular Nanostructure on the Performance of Organic–Inorganic Photomechanical Actuator Membranes. *Adv. Funct. Mater.* **2020**, *30* (2), 1–9. https://doi.org/10.1002/adfm.201902396.

(111) Long, F.; Cheng, Y.; Ren, Y.; Wang, J.; Li, Z.; Sun, A.; Xu, G. Latest Advances in Development of Smart Phase Change Material for Soft Actuators. *Adv. Eng. Mater.* **2022**, *24* (3), 1–16. https://doi.org/10.1002/adem.202100863.

(112) Ogden, S.; Klintberg, L.; Thornell, G.; Hjort, K.; Bodén, R. Review on Miniaturized Paraffin Phase Change Actuators, Valves, and Pumps. *Microfluid. Nanofluidics* **2014**, *17* (1), 53–71. https://doi.org/10.1007/s10404-013-1289-3.

(113) Wilhelm, E.; Richter, C.; Rapp, B. E. Phase Change Materials in Microactuators: Basics, Applications and Perspectives. *Sensors Actuators, A Phys.* **2018**, *271*, 303–347. https://doi.org/10.1016/j.sna.2018.01.043.

(114) Jin, Y. J.; Kim, B. S. Il; Lee, W. E.; Lee, C. L.; Kim, H.; Song, K. H.; Jang, S. Y.; Kwak, G. Phase-Change Hybrids for Thermo-Responsive Sensors and Actuators.

NPG Asia Mater. **2014**, *6* (10), 1–8. https://doi.org/10.1038/am.2014.94.

(115) Han, J.; Jiang, W.; Niu, D.; Li, Y.; Zhang, Y.; Lei, B.; Liu, H.; Shi, Y.; Chen, B.; Yin, L.; Liu, X.; Peng, D.; Lu, B. Untethered Soft Actuators by Liquid–Vapor Phase Transition: Remote and Programmable Actuation. *Adv. Intell. Syst.* **2019**, *1* (1900109), 1–11. https://doi.org/10.1002/aisy.201900109.

(116) Whalen, S. A.; Bahr, D. F.; Richards, C. D.; Richards, R. F. Characterization of a Liquid-Vapor Phase-Change Actuator. *Proc. IMECE2005* **2005**, 751–761. https://doi.org/10.1115/IMECE2005-82564.

(117) Li, X.; Duan, H.; Lv, P.; Yi, X. Soft Actuators Based on Liquid-Vapor Phase Change Composites. *Soft Robot.* **2021**, *8* (3), 251–261. https://doi.org/10.1089/soro.2020.0018.

(118) Noguchi, T.; Tsumori, F. Soft Actuator with Large Volumetric Change Using Vapor-Liquid Phase Transition. *Jpn. J. Appl. Phys.* **2020**, *59* (SIIL08), 751–761. https://doi.org/10.35848/1347-4065/ab85ae.

(119) Matsuoka, H.; Suzumori, K.; Kanda, T. Development of a Gas/Liquid Phase Change Actuator for High Temperatures. *ROBOMECH J.* **2016**, *3* (1), 1–7. https://doi.org/10.1186/s40648-016-0041-7.

(120) Matsuoka, H.; Suzumori, K. Gas/Liquid Phase Change Actuator for Use in Extreme Temperature Environments. *Int. J. Autom. Technol.* **2014**, *8* (2), 140–146. https://doi.org/10.20965/ijat.2014.p0140.

(121) Wang, M.; Zhou, L.; Deng, W.; Hou, Y.; He, W.; Yu, L.; Sun, H.; Ren, L.; Hou, X. Ultrafast Response and Programmable Locomotion of Liquid/Vapor/Light-Driven Soft Multifunctional Actuators. *ACS Nano* **2022**, *16* (2), 2672–2681. https://doi.org/10.1021/acsnano.1c09477.

(122) Li, J.; Zhang, R.; Mou, L.; Jung de Andrade, M.; Hu, X.; Yu, K.; Sun, J.; Jia, T.; Dou, Y.; Chen, H.; Fang, S.; Qian, D.; Liu, Z. Photothermal Bimorph Actuators with In-Built Cooler for Light Mills, Frequency Switches, and Soft Robots. *Adv. Funct. Mater.* **2019**, *29* (1808995), 1–11. https://doi.org/10.1002/adfm.201808995.

(123) Pastine, S. J.; Okawa, D.; Zettl, A.; Fréchet, J. M. J. Chemicals on Demand with Phototriggerable Microcapsules. *J. Am. Chem. Soc.* **2009**, *131* (38), 13586–13587. https://doi.org/10.1021/ja905378v.

(124) Zhang, X.; Pint, C. L.; Lee, M. H.; Schubert, B. E.; Jamshidi, A.; Takei, K.; Ko, H.; Gillies, A.; Bardhan, R.; Urban, J. J.; Wu, M.; Fearing, R.; Javey, A. Optically- and Thermally-Responsive Programmable Materials Based on Carbon Nanotube-Hydrogel Polymer Composites. *Nano Lett.* **2011**, *11* (8), 3239–3244. https://doi.org/10.1021/nl201503e.

(125) Kohlmeyer, R. R.; Chen, J. Wavelength-Selective, IR Light-Driven Hinges Based

on Liquid Crystalline Elastomer Composites. *Angew. Chemie - Int. Ed.* **2013**, *52* (35), 9234–9237. https://doi.org/10.1002/anie.201210232.

(126) Lu, H.; Yao, Y.; Huang, W. M.; Leng, J.; Hui, D. Significantly Improving Infrared Light-Induced Shape Recovery Behavior of Shape Memory Polymeric Nanocomposite via a Synergistic Effect of Carbon Nanotube and Boron Nitride. *Compos. Part B Eng.* **2014**, *62*, 256–261. https://doi.org/10.1016/j.compositesb.2014.03.007.

(127) Torras, N.; Zinoviev, K. E.; Camargo, C. J.; Campo, E. M.; Campanella, H.; Esteve, J.; Marshall, J. E.; Terentjev, E. M.; Omastová, M.; Krupa, I.; Teplický, P.; Mamojka, B.; Bruns, P.; Roeder, B.; Vallribera, M.; Malet, R.; Zuffanelli, S.; Soler, V.; Roig, J.; Walker, N.; Wenn, D.; Vossen, F.; Crompvoets, F. M. H. Tactile Device Based on Opto-Mechanical Actuation of Liquid Crystal Elastomers. *Sensors Actuators, A Phys.* **2014**, *208*, 104–112. https://doi.org/10.1016/j.sna.2014.01.012.

(128) Ji, M.; Jiang, N.; Chang, J.; Sun, J. Near-Infrared Light-Driven, Highly Efficient Bilayer Actuators Based on Polydopamine-Modified Reduced Graphene Oxide. *Adv. Funct. Mater.* **2014**, *24* (34), 5412–5419. https://doi.org/10.1002/adfm.201401011.

(129) Tai, Y.; Lubineau, G.; Yang, Z. Light-Activated Rapid-Response Polyvinylidene-Fluoride-Based Flexible Films. *Adv. Mater.* **2016**, *28* (23), 4665–4670. https://doi.org/10.1002/adma.201600211.

(130) Deng, J.; Li, J.; Chen, P.; Fang, X.; Sun, X.; Jiang, Y.; Weng, W.; Wang, B.; Peng, H. Tunable Photothermal Actuators Based on a Pre-Programmed Aligned Nanostructure. *J. Am. Chem. Soc.* **2016**, *138* (1), 225–230. https://doi.org/10.1021/jacs.5b10131.

(131) Zhao, Z.; Wang, H.; Shang, L.; Yu, Y.; Fu, F.; Zhao, Y.; Gu, Z. Bioinspired Heterogeneous Structural Color Stripes from Capillaries. *Adv. Mater.* **2017**, *29* (1704569), 1–8. https://doi.org/10.1002/adma.201704569.

(132) Tang, Z.; Gao, Z.; Jia, S.; Wang, F.; Wang, Y. Graphene-Based Polymer Bilayers with Superior Light-Driven Properties for Remote Construction of 3D Structures. *Adv. Sci.* **2017**, *4* (1600437), 1–10. https://doi.org/10.1002/advs.201600437.

(133) Li, J.; Mou, L.; Zhang, R.; Sun, J.; Wang, R.; An, B.; Chen, H.; Inoue, K.; Ovalle-Robles, R.; Liu, Z. Multi-Responsive and Multi-Motion Bimorph Actuator Based on Super-Aligned Carbon Nanotube Sheets. *Carbon N. Y.* **2019**, *148*, 487–495. https://doi.org/10.1016/j.carbon.2019.04.014.

(134) Chen, L.; Weng, M.; Zhou, P.; Zhang, L.; Huang, Z.; Zhang, W. Multi-Responsive Actuators Based on a Graphene Oxide Composite: Intelligent Robot and Bioinspired Applications. *Nanoscale* **2017**, *9* (28), 9825–9833. https://doi.org/10.1039/c7nr01913k.

(135) Meng, J.; Mu, J.; Hou, C.; Zhang, Q.; Li, Y.; Wang, H. A Flexible Metallic Actuator Using Reduced Graphene Oxide as a Multifunctional Component. *Nanoscale* **2017**, *9* (35), 12963–12968. https://doi.org/10.1039/c7nr03028b.

(136) Wang, F.; Li, Q.; Park, J. O.; Zheng, S.; Choi, E. Ultralow Voltage High-Performance Bioartificial Muscles Based on Ionically Crosslinked Polypyrrole-Coated Functional Carboxylated Bacterial Cellulose for Soft Robots. *Adv. Funct. Mater.* **2021**, *31* (2007749), 1–10. https://doi.org/10.1002/adfm.202007749.

(137) Xing, S. ting; Wang, P. ping; Liu, S. qi; Xu, Y. hang; Zheng, R. min; Deng, Z. fu; Peng, Z. fei; Li, J. yun; Wu, Y. yi; Liu, L. A Shape-Memory Soft Actuator Integrated with Reversible Electric/Moisture Actuating and Strain Sensing. *Compos. Sci. Technol.* **2020**, *193* (108133), 1–9. https://doi.org/10.1016/j.compscitech.2020.108133.

(138) Stuhl, B. K.; Sawyer, B. C.; Wang, D.; Ye, J. Magneto-Optical Trap for Polar Molecules. *Phys. Rev. Lett.* **2008**, *101* (24), 1–4. https://doi.org/10.1103/PhysRevLett.101.243002.

(139) Zhou, P.; Chen, L.; Yao, L.; Weng, M.; Zhang, W. Humidity- and Light-Driven Actuators Based on Carbon Nanotube-Coated Paper and Polymer Composite. *Nanoscale* **2018**, *10* (18), 8422–8427. https://doi.org/10.1039/c7nr09580e.

(140) Xu, G.; Zhang, M.; Zhou, Q.; Chen, H.; Gao, T.; Li, C.; Shi, G. A Small Graphene Oxide Sheet/Polyvinylidene Fluoride Bilayer Actuator with Large and Rapid Responses to Multiple Stimuli. *Nanoscale* **2017**, *9* (44), 17465–17470. https://doi.org/10.1039/c7nr07116g.

(141) Ma, H.; Hou, J.; Wang, X.; Zhang, J.; Yuan, Z.; Xiao, L.; Wei, Y.; Fan, S.; Jiang, K.; Liu, K. Flexible, All-Inorganic Actuators Based on Vanadium Dioxide and Carbon Nanotube Bimorphs. *Nano Lett.* **2017**, *17* (1), 421–428. https://doi.org/10.1021/acs.nanolett.6b04393.

(142) Wang, E.; Desai, M. S.; Lee, S. W. Light-Controlled Graphene-Elastin Composite Hydrogel Actuators. *Nano Lett.* **2013**, *13* (6), 2826–2830. https://doi.org/10.1021/nl401088b.

(143) Hu, Y.; Wu, G.; Lan, T.; Zhao, J.; Liu, Y.; Chen, W. A Graphene-Based Bimorph Structure for Design of High Performance Photoactuators. *Adv. Mater.* **2015**, *27* (47), 7867–7873. https://doi.org/10.1002/adma.201502777.

(144) Mu, J.; Hou, C.; Wang, H.; Li, Y.; Zhang, Q.; Zhu, M. Origami-Inspired Active Graphene-Based Paper for Programmable Instant Self-Folding Walking Devices. *Sci. Adv.* **2015**, *1* (10), 1–9. https://doi.org/10.1126/sciadv.1500533.

(145) Jiang, W.; Niu, D.; Liu, H.; Wang, C.; Zhao, T.; Yin, L.; Shi, Y.; Chen, B.; Ding, Y.; Lu, B. Photoresponsive Soft-Robotic Platform: Biomimetic Fabrication and Remote Actuation. *Adv. Funct. Mater.* **2014**, *24* (48), 7598–7604.

https://doi.org/10.1002/adfm.201402070.

(146) Li, L.; Meng, J.; Hou, C.; Zhang, Q.; Li, Y.; Yu, H.; Wang, H. Dual-Mechanism and Multimotion Soft Actuators Based on Commercial Plastic Film. *ACS Appl. Mater. Interfaces* **2018**, *10* (17), 15122–15128. https://doi.org/10.1021/acsami.8b00396.

(147) Wu, G.; Wu, X.; Xu, Y.; Cheng, H.; Meng, J.; Yu, Q.; Shi, X.; Zhang, K.; Chen, W.; Chen, S. High-Performance Hierarchical Black-Phosphorous-Based Soft Electrochemical Actuators in Bioinspired Applications. *Adv. Mater.* **2019**, *31* (1806492), 1–11. https://doi.org/10.1002/adma.201806492.

(148) Kuang, Y.; Chen, C.; Cheng, J.; Pastel, G.; Li, T.; Song, J.; Jiang, F.; Li, Y.; Zhang, Y.; Jang, S. H.; Chen, G.; Li, T.; Hu, L. Selectively Aligned Cellulose Nanofibers towards High-Performance Soft Actuators. *Extrem. Mech. Lett.* **2019**, *29* (100463), 1–8. https://doi.org/10.1016/j.eml.2019.100463.

(149) Feng, Y.; Qin, M.; Guo, H.; Yoshino, K.; Feng, W. Infrared-Actuated Recovery of Polyurethane Filled by Reduced Graphene Oxide/Carbon Nanotube Hybrids with High Energy Density. *ACS Appl. Mater. Interfaces* **2013**, *5* (21), 10882–10888. https://doi.org/10.1021/am403071k.

(150) Yu, L.; Wang, Q.; Sun, J.; Li, C.; Zou, C.; He, Z.; Wang, Z.; Zhou, L.; Zhang, L.; Yang, H. Multi-Shape-Memory Effects in a Wavelength-Selective Multicomposite. *J. Mater. Chem. A* **2015**, *3* (26), 13953–13961. https://doi.org/10.1039/c5ta01894c.

(151) Han, D. D.; Zhang, Y. L.; Liu, Y.; Liu, Y. Q.; Jiang, H. B.; Han, B.; Fu, X. Y.; Ding, H.; Xu, H. L.; Sun, H. B. Bioinspired Graphene Actuators Prepared by Unilateral UV Irradiation of Graphene Oxide Papers. *Adv. Funct. Mater.* **2015**, *25* (28), 4548–4557. https://doi.org/10.1002/adfm.201501511.

(152) Han, D. D.; Zhang, Y. L.; Jiang, H. B.; Xia, H.; Feng, J.; Chen, Q. D.; Xu, H. L.; Sun, H. B. Moisture-Responsive Graphene Paper Prepared by Self-Controlled Photoreduction. *Adv. Mater.* **2015**, *27* (2), 332–338. https://doi.org/10.1002/adma.201403587.

(153) Xiong, L.; Jin, H.; Lu, Y.; Li, X.; Ai, X.; Yang, H.; Huang, L. A Solvent Molecule Driven Pure PEDOT:PSS Actuator. *Macromol. Mater. Eng.* **2020**, *305* (8), 1–8. https://doi.org/10.1002/mame.202000327.

(154) Wang, W.; Xiang, C.; Zhu, Q.; Zhong, W.; Li, M.; Yan, K.; Wang, D. Multistimulus Responsive Actuator with GO and Carbon Nanotube/PDMS Bilayer Structure for Flexible and Smart Devices. *ACS Appl. Mater. Interfaces* **2018**, *10* (32), 27215–27223. https://doi.org/10.1021/acsami.8b08554.

(155) Chen, M.; Frueh, J.; Wang, D.; Lin, X.; Xie, H.; He, Q. Polybenzoxazole Nanofiber-Reinforced Moisture-Responsive Soft Actuators. *Sci. Rep.* **2017**, *7* (1),

1–10. https://doi.org/10.1038/s41598-017-00870-w.

(156) Xiang, C.; Wang, W.; Zhu, Q.; Xue, D.; Zhao, X.; Li, M.; Wang, D. Flexible and Super-Sensitive Moisture-Responsive Actuators by Dispersing Graphene Oxide into Three-Dimensional Structures of Nanofibers and Silver Nanowires. *ACS Appl. Mater. Interfaces* **2020**, *12* (2), 3245–3253. https://doi.org/10.1021/acsami.9b20365.

(157) Wang, X.; Jiao, N.; Tung, S.; Liu, L. Photoresponsive Graphene Composite Bilayer Actuator for Soft Robots. *ACS Appl. Mater. Interfaces* **2019**, *11* (33), 30290–30299. https://doi.org/10.1021/acsami.9b09491.

(158) Bardaweel, H. K.; Anderson, M. J.; Weiss, L. W.; Richards, R. F.; Richards, C. D. Characterization and Modeling of the Dynamic Behavior of a Liquid-Vapor Phase Change Actuator. *Sensors Actuators, A Phys.* **2009**, *149* (2), 284–291. https://doi.org/10.1016/j.sna.2008.11.020.

(159) Zhao, Z.; Glod, S.; Poulikakos, D. Pressure and Power Generation During Explosive Vaporization on a Thin-Film Microheater. *Int. J. Heat Mass Transf.* **2000**, *43* (2), 281–296. https://doi.org/10.1016/S0017-9310(99)00129-5.

(160) Chen, S. C.; Culpepper, M. L. Design of Contoured Thermomechanical Actuators and Pulsing Actuation to Enhance Dynamic Performance. *J. Microelectromechanical Syst.* **2012**, *21* (2), 340–349. https://doi.org/10.1109/JMEMS.2011.2175365.

(161) Okamura, H. On the Efficiency of Heat Engines by Pulsed Laser. *Proc. SPIE Int. Symp. Optomechatronic Technol.* **2008**, *7266* (726609), 1–7. https://doi.org/10.1117/12.807414.

(162) Curtis, A. D.; Banishev, A. A.; Shaw, W. L.; Dlott, D. D. Laser-Driven Flyer Plates for Shock Compression Science: Launch and Target Impact Probed by Photon Doppler Velocimetry. *Rev. Sci. Instrum.* **2014**, *85* (043908), 1–12. https://doi.org/10.1063/1.4871361.

(163) Dlott, D. D. Laser Pulses into Bullets: Tabletop Shock Experiments. *Phys. Chem. Chem. Phys.* **2022**, 10653–10666. https://doi.org/10.1039/d2cp00418f.

(164) Wang, L.; Ai, M.; Zhang, W.; Jiang, H.; Wang, Y.; Qin, W.; Zhang, L.; Ji, X.; Li, Y.; Tang, D. MgAl Hydride Films for Enhanced Energy Conversion Efficiency of a Laser-Driven Flyer. *Adv. Eng. Mater.* **2021**, *23* (2000745), 1–6. https://doi.org/10.1002/adem.202000745.

(165) Paisley, D. L.; Luo, S. N.; Greenfield, S. R.; Koskelo, A. C. Laser-Launched Flyer Plate and Confined Laser Ablation for Shock Wave Loading: Validation and Applications. *Rev. Sci. Instrum.* **2008**, *79* (023902), 1–8. https://doi.org/10.1063/1.2839399.

(166) Tanaka, K. A.; Hara, M.; Ozaki, N.; Sasatani, Y.; Anisimov, S. I.; Kondo, K. I.; Nakano, M.; Nishihara, K.; Takenaka, H.; Yoshida, M.; Mima, K. Multi-Layered Flyer Accelerated by Laser Induced Shock Waves. *Phys. Plasmas* **2000**, *7* (2), 676–680. https://doi.org/10.1063/1.873851.

(167) Lawrence, R. J.; Trott, W. M. Theoretical Analysis of a Pulsed-Laser-Driven Hypervelocity Flyer Launcher. *Int. J. Impact Eng.* **1993**, *14* (1–4), 439–449. https://doi.org/10.1016/0734-743X(93)90041-5.

(168) Gao, Y.; Wang, L.; Qin, W.; Lyu, G.; Huang, J.; Tang, D. Optimization of the Composition of Al-Mg Alloy Films for Laser-Driven Flyer. *Opt. Laser Technol.* **2022**, *149* (107881), 1–7. https://doi.org/10.1016/j.optlastec.2022.107881.

(169) Wang, L.; Yan, Y.; Ji, X.; Zhang, W.; Jiang, H.; Qin, W.; Wang, Y.; Tang, D. Improving the Energy Conversion Efficiency of a Laser-Driven Flyer by an In Situ-Fabricated Nano-Absorption Layer. *Nanoscale Res. Lett.* **2020**, *15* (125), 1–8. https://doi.org/10.1186/s11671-020-03346-5.

(170) Yu, H.; Fedotov, V.; Baek, W.; Yoh, J. J. Towards Controlled Flyer Acceleration by a Laser-Driven Mini Flyer. *Appl. Phys. A Mater. Sci. Process.* **2014**, *115* (3), 971–978. https://doi.org/10.1007/s00339-013-7916-8.

(171) Swift, D. C.; Niemczura, J. G.; Paisley, D. L.; Johnson, R. P.; Luo, S. N.; Tierney IV, T. E. Laser-Launched Flyer Plates for Shock Physics Experiments. *Rev. Sci. Instrum.* **2005**, *76* (093907), 1–9. https://doi.org/10.1063/1.2052593.

(172) Guo, W.; Wu, L.; He, N.; Chen, S.; Zhang, W.; Shen, R.; Ye, Y. Efficiency Relationship between Initiation of HNS-IV and Nanosecond Pulsed Laser-Driven Flyer Plates of Layered Structure. *Laser Part. Beams* **2018**, *36* (1), 29–40. https://doi.org/10.1017/S0263034617000854.

(173) Brierley, H. R.; Williamson, D. M.; Vine, T. A. Improving Laser-Driven Flyer Efficiency with High Absorptance Layers. *AIP Conf. Proc.* **2012**, *1426* (315), 315–318. https://doi.org/10.1063/1.3686282.

(174) Banishev, A. A.; Shaw, W. L.; Bassett, W. P.; Dlott, D. D. High-Speed Laser-Launched Flyer Impacts Studied with Ultrafast Photography and Velocimetry. *J. Dyn. Behav. Mater.* **2016**, *2* (2), 194–206. https://doi.org/10.1007/s40870-016-0058-2.

(175) Brown, K. E.; Shaw, W. L.; Zheng, X.; Dlott, D. D. Simplified Laser-Driven Flyer Plates for Shock Compression Science. *Rev. Sci. Instrum.* **2012**, *83* (103901), 1–13. https://doi.org/10.1063/1.4754717.

(176) Lewis, T. N.; Wang, C.; Daniel, J. R.; Dhital, M.; Bardeen, C. J.; Hemmerling, B. Optimizing Pulsed-Laser Ablation Production of AlCl Molecules for Laser Cooling. *Phys. Chem. Chem. Phys.* **2021**, *23*, 22785–22793. https://doi.org/10.1039/d1cp03515k.

(177) Scientific, H. *Recording Fluorescence Quantum Yields*. https://static.horiba.com/fileadmin/Horiba/Application/Materials/Material_Research/Quantum_Dots/quantumyieldstrad.pdf (accessed 2022-10-17).

(178) Systems, U. *Surface Xplorer Data Analysis Software*. https://ultrafastsystems.com/surface-xplorer-data-analysis-software/ (accessed 2021-06-09).

(179) Wineland, D. J.; Drullinger, R. E.; Walls, F. L. Radiation-Pressure Cooling of Bound Resonant Absorbers. *Phys. Rev. Lett.* **1978**, *40* (25), 1639–1642. https://doi.org/10.1103/PhysRevLett.40.1639.

(180) Phillips, W. D. Laser Cooling and Trapping of Neutral Atoms. *Rev. Mod. Phys.* **1998**, *70* (3), 721–741. https://doi.org/10.1103/revmodphys.70.721.

(181) Cohen-Tannoudji, C. N. Manipulating Atoms with Photons. *Rev. Mod. Phys.* **1998**, *70* (3), 707–719. https://doi.org/0034-6861/98/70(3)/707(13).

(182) Chu, S. The Manipulation of Neutral Particles. *Rev. Mod. Phys.* **1998**, *70* (3), 685–706. https://doi.org/10.1103/revmodphys.70.685.

(183) Eschner, J.; Morigi, G.; Schmidt-Kaler, F.; Blatt, R. Laser Cooling of Trapped Ions. *J. Opt. Soc. Am. B* **2003**, *20* (5), 1003–1015. https://doi.org/10.1364/josab.20.001003.

(184) Greiner, M.; Mandel, O.; Esslinger, T.; Haensch, T. W.; Bloch, I. Quantum Phase Transition from a Superfluid to a Mott Insulator in a Gas of Ultracold Atoms. *Nature* **2002**, *415*, 39–44. https://doi.org/10.1002/chin.200214016.

(185) Uzan, J. P. The Fundamental Constants and Their Variation: Observational and Theoretical Status. *Rev. Mod. Phys.* **2003**, *75* (2), 403–455. https://doi.org/10.1103/RevModPhys.75.403.

(186) Baker, C. J.; Bertsche, W.; Capra, A.; Carruth, C.; Cesar, C. L.; Charlton, M.; Christensen, A.; Collister, R.; Mathad, A. C.; Eriksson, S.; Evans, A.; Evetts, N.; Fajans, J.; Friesen, T.; Fujiwara, M. C.; Gill, D. R.; Grandemange, P.; Granum, P.; Hangst, J. S.; Hardy, W. N.; Hayden, M. E.; Hodgkinson, D.; Hunter, E.; Isaac, C. A.; Johnson, M. A.; Jones, J. M.; Jones, S. A.; Jonsell, S.; Khramov, A.; Knapp, P.; Kurchaninov, L.; Madsen, N.; Maxwell, D.; McKenna, J. T. K.; Menary, S.; Michan, J. M.; Momose, T.; Mullan, P. S.; Munich, J. J.; Olchanski, K.; Olin, A.; Peszka, J.; Powell, A.; Pusa, P.; Rasmussen, C.; Robicheaux, F.; Sacramento, R. L.; Sameed, M.; Sarid, E.; Silveira, D. M.; Starko, D. M.; So, C.; Stutter, G.; Tharp, T. D.; Thibeault, A.; Thompson, R. I.; van der Werf, D. P.; Wurtele, J. S. Laser Cooling of Antihydrogen Atoms. *Nature* **2021**, *592* (7852), 35–42. https://doi.org/10.1038/s41586-021-03289-6.

(187) Ludlow, A. D.; Boyd, M. M.; Ye, J.; Peik, E.; Schmidt, P. O. Optical Atomic Clocks. *Rev. Mod. Phys.* **2015**, *87* (2), 637–701.

https://doi.org/10.1103/RevModPhys.87.637.

(188) Ni, K. K.; Ospelkaus, S.; Wang, D.; Quéméner, G.; Neyenhuis, B.; De Miranda, M. H. G.; Bohn, J. L.; Ye, J.; Jin, D. S. Dipolar Collisions of Polar Molecules in the Quantum Regime. *Nature* **2010**, *464* (7293), 1324–1328. https://doi.org/10.1038/nature08953.

(189) Ospelkaus, S. Quantum-State Controlled Chemical Reactions of Ultracold KRb Molecules. *Science (80-.).* **2012**, *853* (2010), 853–858. https://doi.org/10.48550/arXiv.0912.3854.

(190) Ye, X.; Guo, M.; González-Martínez, M. L.; Quéméner, G.; Wang, D. Collisions of Ultracold 23Na87Rb Molecules with Controlled Chemical Reactivities. *Sci. Adv.* **2018**, *4* (1), 1–7. https://doi.org/10.1126/sciadv.aaq0083.

(191) Tscherbul, T. V.; Kłos, J. Magnetic Tuning of Ultracold Barrierless Chemical Reactions. *Phys. Rev. Res.* **2020**, *2* (1), 1–9. https://doi.org/10.1103/PhysRevResearch.2.013117.

(192) Liu, Y.; Ni, K. K. Bimolecular Chemistry in the Ultracold Regime. *Annu. Rev. Phys. Chem.* **2022**, *73*, 73–96. https://doi.org/10.1146/annurev-physchem-090419-043244.

(193) Micheli, A.; Brennen, G. K.; Zoller, P. A Toolbox for Lattice-Spin Models with Polar Molecules. *Nat. Phys.* **2006**, *2* (5), 341–347. https://doi.org/10.1038/nphys287.

(194) Andreev, V.; Ang, D. G.; DeMille, D.; Doyle, J. M.; Gabrielse, G.; Haefner, J.; Hutzler, N. R.; Lasner, Z.; Meisenhelder, C.; O'Leary, B. R.; Panda, C. D.; West, A. D.; West, E. P.; Wu, X. Improved Limit on the Electric Dipole Moment of the Electron. *Nature* **2018**, *562* (7727), 355–360. https://doi.org/10.1038/s41586-018-0599-8.

(195) Cairncross, W. B.; Gresh, D. N.; Grau, M.; Cossel, K. C.; Roussy, T. S.; Ni, Y.; Zhou, Y.; Ye, J.; Cornell, E. A. Precision Measurement of the Electron's Electric Dipole Moment Using Trapped Molecular Ions. *Phys. Rev. Lett.* **2017**, *119* (15), 1–5. https://doi.org/10.1103/PhysRevLett.119.153001.

(196) Jansen, P.; Bethlem, H. L.; Ubachs, W. Perspective: Tipping the Scales: Search for Drifting Constants from Molecular Spectra. *J. Chem. Phys.* **2014**, *140* (010901), 1–13. https://doi.org/10.1063/1.4853735.

(197) Daprà, M.; Niu, M. L.; Salumbides, E. J.; Murphy, M. T.; Ubachs, W. Constraint on a Cosmological Variation in the Proton-To-Electron Mass Ratio From Electronic Co Absorption. *Astrophys. J.* **2016**, *826* (192), 1–19. https://doi.org/10.3847/0004-637x/826/2/192.

(198) Kobayashi, J.; Ogino, A.; Inouye, S. Measurement of the Variation of Electron-to-

Proton Mass Ratio Using Ultracold Molecules Produced from Laser-Cooled Atoms. *Nat. Commun.* **2019**, *10* (1), 1–5. https://doi.org/10.1038/s41467-019-11761-1.

(199) Kozyryev, I.; Hutzler, N. R. Precision Measurement of Time-Reversal Symmetry Violation with Laser-Cooled Polyatomic Molecules. *Phys. Rev. Lett.* **2017**, *119* (13), 1–6. https://doi.org/10.1103/PhysRevLett.119.133002.

(200) Hudson, J. J.; Kara, D. M.; Smallman, I. J.; Sauer, B. E.; Tarbutt, M. R.; Hinds, E. A. Improved Measurement of the Shape of the Electron. *Nature* **2011**, *473* (7348), 493–496. https://doi.org/10.1038/nature10104.

(201) Kozyryev, I.; Lasner, Z.; Doyle, J. M. Enhanced Sensitivity to Ultralight Bosonic Dark Matter in the Spectra of the Linear Radical SrOH. *Phys. Rev. A* **2021**, *103* (043313), 1–14. https://doi.org/10.1103/PhysRevA.103.043313.

(202) Kondov, S. S.; Lee, C. H.; Leung, K. H.; Liedl, C.; Majewska, I.; Moszynski, R.; Zelevinsky, T. Molecular Lattice Clock with Long Vibrational Coherence. *Nat. Phys.* **2019**, *15* (11), 1118–1122. https://doi.org/10.1038/s41567-019-0632-3.

(203) Demille, D.; Sainis, S.; Sage, J.; Bergeman, T.; Kotochigova, S.; Tiesinga, E. Enhanced Sensitivity to Variation of Me/Mp in Molecular Pectra. *Phys. Rev. Lett.* **2008**, *100* (4), 1–4. https://doi.org/10.1103/PhysRevLett.100.043202.

(204) Chin, C.; Flambaum, V. V.; Kozlov, M. G. Ultracold Molecules: New Probes on the Variation of Fundamental Constants. *New J. Phys.* **2009**, *11* (055048), 1–14. https://doi.org/10.1088/1367-2630/11/5/055048.

(205) Kajita, M. Sensitive Measurement of Mp/Me Variance Using Vibrational Transition Frequencies of Cold Molecules. *New J. Phys.* **2009**, *11* (055010), 1–19. https://doi.org/10.1088/1367-2630/11/5/055010.

(206) Beloy, K.; Borschevsky, A.; Schwerdtfeger, P.; Flambaum, V. V. Enhanced Sensitivity to the Time Variation of the Fine-Structure Constant and Mp/Me in Diatomic Molecules: A Closer Examination of Silicon Monobromide. *Phys. Rev. A - At. Mol. Opt. Phys.* **2010**, *82* (2), 1–7. https://doi.org/10.1103/PhysRevA.82.022106.

(207) DeMille, D. Quantum Computation with Trapped Polar Molecules. *Phys. Rev. Lett.* **2002**, *88* (6), 1–4. https://doi.org/10.1103/PhysRevLett.88.067901.

(208) Yelin, S. F.; Kirby, K.; Côté, R. Schemes for Robust Quantum Computation with Polar Molecules. *Phys. Rev. A* **2006**, *74* (5), 2–5. https://doi.org/10.1103/physreva.74.050301.

(209) Barry, J. F.; McCarron, D. J.; Norrgard, E. B.; Steinecker, M. H.; Demille, D. Magneto-Optical Trapping of a Diatomic Molecule. *Nature* **2014**, *512* (7514), 286–289. https://doi.org/10.1038/nature13634.

(210) Iwata, G. Z.; McNally, R. L.; Zelevinsky, T. High-Resolution Optical Spectroscopy with a Buffer-Gas-Cooled Beam of BaH Molecules. *Phys. Rev. A* **2017**, *96* (2), 1–7. https://doi.org/10.1103/PhysRevA.96.022509.

(211) Baum, L.; Vilas, N. B.; Hallas, C.; Augenbraun, B. L.; Raval, S.; Mitra, D.; Doyle, J. M. 1D Magneto-Optical Trap of Polyatomic Molecules. *Phys. Rev. Lett.* **2020**, *124* (133201), 1–6. https://doi.org/10.1103/PhysRevLett.124.133201.

(212) Augenbraun, B. L.; Frenett, A.; Sawaoka, H.; Hallas, C.; Vilas, N. B.; Nasir, A.; Lasner, Z. D.; Doyle, J. M. Zeeman-Sisyphus Deceleration of Molecular Beams. *Phys. Rev. Lett.* **2021**, *127* (263002), 1–7. https://doi.org/10.1103/PhysRevLett.127.263002.

(213) Lim, J.; Almond, J. R.; Trigatzis, M. A.; Devlin, J. A.; Fitch, N. J.; Sauer, B. E.; Tarbutt, M. R.; Hinds, E. A. Laser Cooled YbF Molecules for Measuring the Electron's Electric Dipole Moment. *Phys. Rev. Lett.* **2018**, *120* (123201), 1–6. https://doi.org/10.1103/PhysRevLett.120.123201.

(214) Mitra, D.; Vilas, N. B.; Hallas, C.; Anderegg, L.; Augenbraun, B. L.; Baum, L.; Miller, C.; Raval, S.; Doyle, J. M. Direct Laser Cooling of a Symmetric Top Molecule. *Science (80-.).* **2020**, *369* (6509), 1366–1369. https://doi.org/10.1126/SCIENCE.ABC5357.

(215) Augenbraun, B. L.; Lasner, Z. D.; Frenett, A.; Sawaoka, H.; Miller, C.; Steimle, T. C.; Doyle, J. M. Laser-Cooled Polyatomic Molecules for Improved Electron Electric Dipole Moment Searches. *New J. Phys.* **2020**, *22* (022003), 1–8. https://doi.org/10.1088/1367-2630/ab687b.

(216) Kozyryev, I.; Baum, L.; Matsuda, K.; Augenbraun, B. L.; Anderegg, L.; Sedlack, A. P.; Doyle, J. M. Sisyphus Laser Cooling of a Polyatomic Molecule. *Phys. Rev. Lett.* **2017**, *118* (17), 1–6. https://doi.org/10.1103/PhysRevLett.118.173201.

(217) Truppe, S.; Marx, S.; Kray, S.; Doppelbauer, M.; Hofsäss, S.; Schewe, H. C.; Walter, N.; Pérez-Riós, J.; Sartakov, B. G.; Meijer, G. Spectroscopic Characterization of Aluminum Monofluoride with Relevance to Laser Cooling and Trapping. *Phys. Rev. A* **2019**, *100* (5), 1–24. https://doi.org/10.1103/PhysRevA.100.052513.

(218) Doppelbauer, M.; Walter, N.; Hofsäss, S.; Marx, S.; Schewe, H. C.; Kray, S.; Pérez-Ríos, J.; Sartakov, B. G.; Truppe, S.; Meijer, G. Characterisation of the State and Its Interaction with the State in Aluminium Monofluoride. *Mol. Phys.* **2021**, *119* (1–2), 0–16. https://doi.org/10.1080/00268976.2020.1810351.

(219) Chen, T.; Bu, W.; Yan, B. Radiative Deflection of a BaF Molecular Beam via Optical Cycling. *Phys. Rev. A* **2017**, *96* (5), 1–6. https://doi.org/10.1103/PhysRevA.96.053401.

(220) Albrecht, R.; Scharwaechter, M.; Sixt, T.; Hofer, L.; Langen, T. Buffer-Gas

Cooling, High-Resolution Spectroscopy, and Optical Cycling of Barium Monofluoride Molecules. *Phys. Rev. A* **2020**, *101* (1), 1–11. https://doi.org/10.1103/PhysRevA.101.013413.

(221) Bahns, J. T.; Stwalley, W. C.; Gould, P. L. Laser Cooling of Molecules: A Sequential Scheme for Rotation, Translation, and Vibration. *J. Chem. Phys.* **1996**, *104* (24), 9689–9697. https://doi.org/10.1063/1.471731.

(222) Xu, L.; Yin, Y.; Wei, B.; Xia, Y.; Yin, J. Calculation of Vibrational Branching Ratios and Hyperfine Structure of 24Mg19 F and Its Suitability for Laser Cooling and Magneto-Optical Trapping. *Phys. Rev. A* **2016**, *93* (1), 1–10. https://doi.org/10.1103/PhysRevA.93.013408.

(223) Isaev, T. A.; Hoekstra, S.; Berger, R. Laser-Cooled RaF as a Promising Candidate to Measure Molecular Parity Violation. *Phys. Rev. A - At. Mol. Opt. Phys.* **2010**, *82* (5), 1–5. https://doi.org/10.1103/PhysRevA.82.052521.

(224) Norrgard, E. B.; Edwards, E. R.; McCarron, D. J.; Steinecker, M. H.; DeMille, D.; Alam, S. S.; Peck, S. K.; Wadia, N. S.; Hunter, L. R. Hyperfine Structure of the B 3 Π1 State and Predictions of Optical Cycling Behavior in the X→B Transition of TlF. *Phys. Rev. A* **2017**, *95* (6), 1–12. https://doi.org/10.1103/PhysRevA.95.062506.

(225) Schnaubelt, J. C.; Shaw, J. C.; McCarron, D. J. Cold CH Radicals for Laser Cooling and Trapping. **2021**.

(226) Rogowski, D. F.; Marshall, P.; Fontijn, A. High-Temperature Fast-Flow Reactor Kinetics Studies of the Reactions of Al with Cl2, Al with HCl, and AlCl with Cl2 over Wide Temperature Ranges. *J. Phys. Chem.* **1989**, *93* (3), 1118–1123. https://doi.org/10.1021/j100340a019.

(227) Himmel, H. J. Characterization of Oligomers of AlCl: Al-Cl versus Al-Al Bonding. *Eur. J. Inorg. Chem.* **2005**, No. 10, 1886–1894. https://doi.org/10.1002/ejic.200401016.

(228) Lide, D. R. High-Temperature Microwave Spectroscopy: AlF and AlCl. *J. Chem. Phys.* **1965**, *42* (3), 1013–1018. https://doi.org/10.1063/1.1696035.

(229) Hedderich, H. G.; Dulick, M.; Bernath, P. F. High Resolution Emission Spectroscopy of AlCl at 20 μ. *J. Chem. Phys.* **1993**, *99* (11), 8363–8370. https://doi.org/10.1063/1.465611.

(230) Dearden, D. V.; Johnson, R. D.; Hudgens, J. W. Aluminum Monochloride Excited States Observed by Resonance-Enhanced Multiphoton Ionization Spectroscopy. *J. Chem. Phys.* **1993**, *99* (10), 7521–7528. https://doi.org/10.1063/1.465682.

(231) Wyse, F. C.; Gordy, W. Millimeter Wave Rotational Spectra of AlCl, AlBr, and AlI. *J. Chem. Phys.* **1972**, *56* (5), 2130–2136. https://doi.org/10.1063/1.1677509.

(232) Rumble, J. R. *CRC Handbook of Chemistry and Physics*, 101st ed.; 2021.

(233) Numata, M.; Sugiura, M.; Fuwa, A. Standard Gibbs Energies of Formation for AlCl(GO and AlCl2(g) Species at Temperatures from 600 to 1300 K. *Mater. Trans. JIM* **1993**, *34* (6), 511–516.

(234) Russell, A. S.; Martin, K. E.; Norman Cochran, C. Equilibrium and Rate of Aluminum Monochloride Formation from Aluminum Chloride and Aluminum. *J. Am. Chem. Soc.* **1951**, *73* (4), 1466–1469. https://doi.org/10.1021/ja01148a018.

(235) Kikuchi, T.; Kurosawa, T.; Yagihashi, T. Equilibrium of the 2Al(l)+AlCl3(g)=3AlCl(g) Reaction in the Subhalide Process of Aluminium (Study of Extractive Metallurgy of Aluminium (1)). *Trans. Japan Inst. Met.* **1964**, *5* (2), 122–126. https://doi.org/10.2320/matertrans1960.5.122.

(236) Rao, D. B.; Dadape, V. V. Reaction of AlCl(g) with MgO(c) and the Heat of Formation of MgAl2O4(C). *J. Phys. Chem.* **1967**, *71* (3), 537–540.

(237) Tacke, M.; Schnockel, H. Metastable AlCl as a Solid and in Solution. *Inorg. Chem.* **1989**, *28*, 2896–2898.

(238) Takahashi, Y.; Shlivko, D.; Woolls, G.; Hutzler, N. R. Simulation of Cryogenic Buffer Gas Beams. *Phys. Rev. Res.* **2021**, *3* (023018), 1–11. https://doi.org/10.1103/PhysRevResearch.3.023018.

(239) Kirshenbaum, A. D.; Cahill, J. A.; McGonigal, P. J.; Grosse, A. V. The Density of Liquid NaCl and KCl and an Estimate of Their Critical Constants Together with Those of the Other Alkali Halides. *J. Inorg. Nucl. Chem.* **1962**, *24* (10), 1287–1296. https://doi.org/10.1016/0022-1902(62)80205-X.

(240) Russo, R. E.; Mao, X.; Gonzalez, J. J.; Zorba, V.; Yoo, J. Laser Ablation in Analytical Chemistry. *Anal. Chem.* **2013**, *85* (13), 6162–6177. https://doi.org/10.1021/ac4005327.

(241) Stafe, M.; Vlädoiu, I.; Negutu, C.; Popescu, I. M. Experimental Investigation of the Nanosecond Laser Ablation Rate of Aluminium. *Rom. Reports Phys.* **2008**, *60* (3), 789–796.

(242) Gragossian, A.; Tavassoli, S. H.; Shokri, B. Laser Ablation of Aluminum from Normal Evaporation to Phase Explosion. *J. Appl. Phys.* **2009**, *105* (103304), 1–7. https://doi.org/10.1063/1.3131689.

(243) Zhang, D.; Willitsch, S. Cold Ion Chemistry. *RSC Theor. Comput. Chem. Ser.* **2017**, 496–536.

(244) Cabalin, L. M.; Laserna, J. J. Experimental Determination of Laser Induced Breakdown Thresholds of Metals under Nanosecond Q-Switched Laser Operation. *Spectrochim. acta, Part B At. Spectrosc.* **1998**, *53* (5), 723–730. https://doi.org/10.1016/S0584-8547(98)00107-4.

(245) Stan, C.; Cristescu, C. P.; Alexandroaei, D. Chaos and Hyperchaos in a Symmetrical Discharge Plasma: Experiment and Modelling. *UPB Sci. Bull. Ser. A Appl. Math. Phys.* **2008**, *70* (4), 25–30.

(246) Haglund, R. F.; Affatigato, M.; Arps, J. H.; Tang, K.; Niehof, A.; Heiland, W. Ultraviolet Laser Abltation of Halides and Oxides. *Nucl. Inst. Methods Phys. Res. B* **1992**, *65*, 206–211.

(247) Thomas Dickinson, J. The Role of Defects in the Laser Ablation of Wide Bandgap Materials. *Nucl. Inst. Methods Phys. Res. B* **1994**, *91* (1–4), 634–638. https://doi.org/10.1016/0168-583X(94)96300-2.

(248) Nishikawa, H.; Kanai, M.; Szabo, G. Mechanism for Excimer-Laser Ablation in Alkaline-Earth Metals. *Phys. Rev. B - Condens. Matter Mater. Phys.* **2000**, *61* (2), 967–973. https://doi.org/10.1103/PhysRevB.61.967.

(249) Fernández-Lima, F. A.; Ponciano, C. R.; Da Silveira, E. F. UV Laser-Induced Desorption Mechanism Analyzed through Two-Layer Alkali Halide Samples. *J. Mass Spectrom.* **2008**, *43* (5), 587–593. https://doi.org/10.1002/jms.1350.

(250) Redeker, F. A.; Beckers, H.; Riedel, S. Matrix-Isolation and Comparative Far-IR Investigation of Free Linear [Cl3]- and a Series of Alkali Trichlorides. *Chem. Commun.* **2017**, *53* (96), 12958–12961. https://doi.org/10.1039/c7cc08290h.

(251) Aggarwal, P.; Bethlem, H. L.; Boeschoten, A.; Borschevsky, A.; Esajas, K.; Hao, Y.; Hoekstra, S.; Jungmann, K.; Marshall, V. R.; Meijknecht, T. B.; Mooij, M. C.; Timmermans, R. G. E.; Touwen, A.; Ubachs, W.; Willmann, L.; Yin, Y.; Zapara, A. A Supersonic Laser Ablation Beam Source with Narrow Velocity Spreads. *Rev. Sci. Instrum.* **2021**, *92* (033202), 1–7. https://doi.org/10.1063/5.0035568.

(252) Hensel, K. D.; Styger, C.; Jäger, W.; Merer, A. J.; Gerry, M. C. L. Microwave Spectra of Metal Chlorides Produced Using Laser Ablation. *J. Chem. Phys.* **1993**, *99* (5), 3320–3328. https://doi.org/10.1063/1.465141.

(253) Pope, M.; Swenberg, C. E. Electronic Processes in Organic Crystals and Polymers. *Oxford Univ. Press Demand* **1999**, *56*.

(254) Gust, D.; A. Moore, T.; L. Moore, A. Mimicking Photosynthetic Solar Energy Transduction. *Acc. Chem. Res.* **2000**, *34* (1), 40–48. https://doi.org/10.1021/ar9801301.

(255) K. L.Yeow and, E.; P. Ghiggino, K.; N. H. Reek, J.; J. Crossley, M.; W. Bosman, A.; P. H. J. Schenning, A.; W. Meijer, E. The Dynamics of Electronic Energy Transfer in Novel Multiporphyrin Functionalized Dendrimers: A Time-Resolved Fluorescence Anisotropy Study. *J. Phys. Chem. B* **2000**, *104* (12), 2596–2606. https://doi.org/10.1021/jp993116u.

(256) Jiang, D. L.; Aida, T. Photoisomerization in Dendrimers by Harvesting of Low-

Energy Photons. *Nature* **1997**, *388* (6641), 454–456. https://doi.org/10.1038/41290.

(257) Amanpour, J.; Hu, G.; J. Alexy, E.; Kumar Mandal, A.; Suk Kang, H.; M. Yuen, J.; R. Diers, J.; F. Bocian, D.; S. Lindsey, J.; Holten, D. Tuning the Electronic Structure and Properties of Perylene–Porphyrin–Perylene Panchromatic Absorbers. *J. Phys. Chem. A* **2016**, *120* (38), 7434–7450. https://doi.org/10.1021/acs.jpca.6b06857.

(258) N. Bartynski, A.; Gruber, M.; Das, S.; Rangan, S.; Mollinger, S.; Trinh, C.; E. Bradforth, S.; Vandewal, K.; Salleo, A.; A. Bartynski, R.; Bruetting, W.; E. Thompson, M. Symmetry-Breaking Charge Transfer in a Zinc Chlorodipyrrin Acceptor for High Open Circuit Voltage Organic Photovoltaics. *J. Am. Chem. Soc.* **2015**, *137* (16), 5397–5405. https://doi.org/10.1021/jacs.5b00146.

(259) Métivier, R.; Kulzer, F.; Weil, T.; Müllen, K.; Basché, T. Energy Transfer Rates and Pathways of Single Donor Chromophores in a Multichromophoric Dendrimer Built around a Central Acceptor Core. *J. Am. Chem. Soc.* **2004**, *126* (44), 14364–14365. https://doi.org/10.1021/ja047996o.

(260) Liu, D.; De Feyter, S.; Cotlet, M.; Stefan, A.; Wiesler, U.-M.; Herrmann, A.; Grebel-Koehler, D.; Qu, J.; Müllen, K.; C. De Schryver, F. Fluorescence and Intramolecular Energy Transfer in Polyphenylene Dendrimers. *Macromolecules* **2003**, *36* (16), 5918–5925. https://doi.org/10.1021/ma0344801.

(261) Hsiao, J.-S.; P. Krueger, B.; W. Wagner, R.; E. Johnson, T.; K. Delaney, J.; C. Mauzerall, D.; R. Fleming, G.; S. Lindsey, J.; F. Bocian, D.; J. Donohoe, R. Soluble Synthetic Multiporphyrin Arrays. 2. Photodynamics of Energy-Transfer Processes. *J. Am. Chem. Soc.* **1996**, *118* (45), 11181–11193. https://doi.org/10.1021/ja961612f.

(262) Hindin, E.; A. Forties, R.; S. Loewe, R.; Ambroise, A.; Kirmaier, C.; F. Bocian, D.; S. Lindsey, J.; Holten, D.; S. Knox, R. Excited-State Energy Flow in Covalently Linked Multiporphyrin Arrays: The Essential Contribution of Energy Transfer between Nonadjacent Chromophores. *J. Phys. Chem. B* **2004**, *108* (34), 12821–12832. https://doi.org/10.1021/jp047803j.

(263) R. Justin Thomas, K.; L. Thompson, A.; V. Sivakumar, A.; J. Bardeen, C.; Thayumanavan, S. Energy and Electron Transfer in Bifunctional Non-Conjugated Dendrimers. *J. Am. Chem. Soc.* **2004**, *127* (1), 373–383. https://doi.org/10.1021/ja044778m.

(264) S. Melinger, J.; Pan, Y.; D. Kleiman, V.; Peng, Z.; L. Davis, B.; McMorrow, D.; Lu, M. Optical and Photophysical Properties of Light-Harvesting Phenylacetylene Monodendrons Based on Unsymmetrical Branching. *J. Am. Chem. Soc.* **2002**, *124* (40), 12002–12012. https://doi.org/10.1021/ja020380j.

(265) M. Müller, A.; S. Avlasevich, Y.; W. Schoeller, W.; Müllen, K.; J. Bardeen, C.

Exciton Fission and Fusion in Bis(Tetracene) Molecules with Different Covalent Linker Structures. *J. Am. Chem. Soc.* **2007**, *129* (46), 14240–14250. https://doi.org/10.1021/ja073173y.

(266) Korovina, N. V.; Joy, J.; Feng, X.; Feltenberger, C.; I. Krylov, A.; E. Bradforth, S.; E. Thompson, M. Linker-Dependent Singlet Fission in Tetracene Dimers. *J. Am. Chem. Soc.* **2018**, *140* (32), 10179–10190. https://doi.org/10.1021/jacs.8b04401.

(267) N. Sanders, S.; Kumarasamy, E.; B. Pun, A.; Tuan Trinh, M.; Choi, B.; Xia, J.; J. Taffet, E.; Z. Low, J.; R. Miller, J.; Roy, X.; Zhu, X.-Y.; L. Steigerwald, M.; Y. Sfeir, M.; M. Campos, L. Quantitative Intramolecular Singlet Fission in Bipentacenes. *J. Am. Chem. Soc.* **2015**, *137* (28), 8965–8972. https://doi.org/10.1021/jacs.5b04986.

(268) Pun, A. B.; Asadpoordarvish, A.; Kumarasamy, E.; Tayebjee, M. J. Y.; Niesner, D.; McCamey, D. R.; Sanders, S. N.; Campos, L. M.; Sfeir, M. Y. Ultra-Fast Intramolecular Singlet Fission to Persistent Multiexcitons by Molecular Design. *Nat. Chem.* **2019**, *11* (9), 821–828. https://doi.org/10.1038/s41557-019-0297-7.

(269) Akdag, A.; Wahab, A.; Beran, P.; Rulíšek, L.; Dron, P. I.; Ludvík, J.; Michl, J. Covalent Dimers of 1,3-Diphenylisobenzofuran for Singlet Fission: Synthesis and Electrochemistry. *J. Org. Chem.* **2015**, *80* (1), 80–89. https://doi.org/10.1021/jo502004r.

(270) Basel, B. S.; Zirzlmeier, J.; Hetzer, C.; Phelan, B. T.; Krzyaniak, M. D.; Reddy, S. R.; Coto, P. B.; Horwitz, N. E.; Young, R. M.; White, F. J.; Hampel, F.; Clark, T.; Thoss, M.; Tykwinski, R. R.; Wasielewski, M. R.; Guldi, D. M. Unified Model for Singlet Fission within a Non-Conjugated Covalent Pentacene Dimer. *Nat. Commun.* **2017**, *8* (May), 1–8. https://doi.org/10.1038/ncomms15171.

(271) Serin, J. M.; Brousmiche, D. W.; Fréchet, J. M. J. Cascade Energy Transfer in a Conformationally Mobile Multichromophoric Dendrimer. *Chem. Commun.* **2002**, *2* (22), 2605–2607. https://doi.org/10.1039/b207905d.

(272) Ahn, T.-S.; Nantalaksakul, A.; R. Dasari, R.; O. Al-Kaysi, R.; M. Müller, A.; Thayumanavan, S.; J. Bardeen, C. Energy and Charge Transfer Dynamics in Fully Decorated Benzyl Ether Dendrimers and Their Disubstituted Analogues. *J. Phys. Chem. B* **2006**, *110* (48), 24331–24339. https://doi.org/10.1021/jp0649706.

(273) Harvey, P. D.; Brégier, F.; Aly, S. M.; Szmytkowski, J.; Paige, M. F.; Steer, R. P. Dendron to Central Core S1-S1 and S 2-Sn (N>1) Energy Transfers in Artificial Special Pairs Containing Dendrimers with Limited Numbers of Conformations. *Chem. - A Eur. J.* **2013**, *19* (13), 4352–4368. https://doi.org/10.1002/chem.201203033.

(274) Ondarse-Alvarez, D.; Kömürlü, S.; Roitberg, A. E.; Pierdominici-Sottile, G.; Tretiak, S.; Fernandez-Alberti, S.; Kleiman, V. D. Ultrafast Electronic Energy Relaxation in a Conjugated Dendrimer Leading to Inter-Branch Energy

Redistribution. *Phys. Chem. Chem. Phys.* **2016**, *18* (36), 25080–25089. https://doi.org/10.1039/c6cp04448d.

(275) Pasman, P.; Rob, F.; W. Verhoeven, J. Intramolecular Charge-Transfer Absorption and Emission Resulting from through-Bond Interaction in Bichromophoric Molecules. *J. Am. Chem. Soc.* **2002**, *104* (19), 5127–5133. https://doi.org/10.1021/ja00383a023.

(276) Heitele, H.; Michel-Beyerle, M. E. Electron Transfer through Aromatic Spacers in Bridged Electron-Donor-Acceptor Molecules. *J. Am. Chem. Soc.* **1985**, *107* (26), 8286–8288.

(277) N. Paddon-Row, M. Investigating Long-Range Electron-Transfer Processes with Rigid, Covalently Linked Donor-(Norbornylogous Bridge)-Acceptor Systems. *Acc. Chem. Res.* **2002**, *27* (1), 18–25. https://doi.org/10.1021/ar00037a003.

(278) H. A. Clayton, A.; D. Scholes, G.; P. Ghiggino, K.; N. Paddon-Row, M. Through-Bond and Through-Space Coupling in Photoinduced Electron and Energy Transfer: An Ab Initio and Semiempirical Study. *J. Phys. Chem.* **1996**, *100* (26), 10912–10918. https://doi.org/10.1021/jp953532o.

(279) Davis, W. B.; Svec, W. A.; Ratner, M. A.; Wasielewski, M. R. Molecular-Wire Behaviour in p-Phenylenevinylene Oligomers. *Nat. Lett.* **1998**, *396*, 60–63.

(280) Kilså, K.; Kajanus, J.; N. Macpherson, A.; Mårtensson, J.; Albinsson, B. Bridge-Dependent Electron Transfer in Porphyrin-Based Donor−Bridge−Acceptor Systems. *J. Am. Chem. Soc.* **2001**, *123* (13), 3069–3080. https://doi.org/10.1021/ja003820k.

(281) L. Thompson, A.; Ahn, T.-S.; R. Justin Thomas, K.; Thayumanavan, S.; J. Martínez, T.; J. Bardeen, C. Using Meta Conjugation To Enhance Charge Separation versus Charge Recombination in Phenylacetylene Donor−Bridge−Acceptor Complexes. *J. Am. Chem. Soc.* **2005**, *127* (47), 16348–16349. https://doi.org/10.1021/ja054543q.

(282) Cruz, C. D.; Christensen, P. R.; Chronister, E. L.; Casanova, D.; Wolf, M. O.; Bardeen, C. J. Sulfur-Bridged Terthiophene Dimers: How Sulfur Oxidation State Controls Interchromophore Electronic Coupling. *J. Am. Chem. Soc.* **2015**, *137* (39), 12552–12564. https://doi.org/10.1021/jacs.5b05457.

(283) Cruz, C. D.; Yuan, J.; Climent, C.; Tierce, N. T.; Christensen, P. R.; Chronister, E. L.; Casanova, D.; Wolf, M. O.; Bardeen, C. J. Using Sulfur Bridge Oxidation to Control Electronic Coupling and Photochemistry in Covalent Anthracene Dimers. *Chem. Sci.* **2019**, *10* (32), 7561–7573. https://doi.org/10.1039/c8sc05598j.

(284) Kumarasamy, E.; N. Sanders, S.; J. Y. Tayebjee, M.; Asadpoordarvish, A.; J. H. Hele, T.; G. Fuemmeler, E.; B. Pun, A.; M. Yablon, L.; Z. Low, J.; W. Paley, D.; C. Dean, J.; Choi, B.; D. Scholes, G.; L. Steigerwald, M.; Ananth, N.; R.

McCamey, D.; Y. Sfeir, M.; M. Campos, L. Tuning Singlet Fission in π-Bridge-π Chromophores. *J. Am. Chem. Soc.* **2017**, *139* (36), 12488–12494. https://doi.org/10.1021/jacs.7b05204.

(285) M. Geary, L.; W. Glasspoole, B.; M. Kim, M.; J. Krische, M. Successive C–C Coupling of Dienes to Vicinally Dioxygenated Hydrocarbons: Ruthenium Catalyzed [4 + 2] Cycloaddition across the Diol, Hydroxycarbonyl, or Dione Oxidation Levels. *J. Am. Chem. Soc.* **2013**, *135* (10), 3796–3799. https://doi.org/10.1021/ja400691t.

(286) M. Geary, L.; Chen, T.-Y.; Patrick Montgomery, T.; J. Krische, M. Benzannulation via Ruthenium-Catalyzed Diol–Diene [4+2] Cycloaddition: One- and Two-Directional Syntheses of Fluoranthenes and Acenes. *J. Am. Chem. Soc.* **2014**, *136* (16), 5920–5922. https://doi.org/10.1021/ja502659t.

(287) Kasun, Z. A.; Sato, H.; Nie, J.; Mori, Y.; Bender, J. A.; Roberts, S. T.; Krische, M. J. Alternating Oligo(o,p-Phenylenes) via Ruthenium Catalyzed Diol-Diene Benzannulation: Orthogonality to Cross-Coupling Enables de Novo Nanographene and PAH Construction. *Chem. Sci.* **2018**, *9* (40), 7866–7873. https://doi.org/10.1039/c8sc03236j.

(288) Suravarapu, S. R.; Parvathaneni, S. P.; Bender, J. A.; Roberts, S. T.; Krische, M. J. Benzannulation through Ruthenium(0)-Catalyzed Transfer Hydrogenative Cycloaddition: Precision Synthesis and Photophysical Characterization of Soluble Diindenoperylenes. *Chem. - A Eur. J.* **2020**, *26* (33), 7504–7510. https://doi.org/10.1002/chem.202001731.

(289) Shuler, W. G.; Parvathaneni, S. P.; Rodriguez, J. B.; Lewis, T. N.; Berges, A. J.; Bardeen, C. J.; Krische, M. J. Synthesis and Photophysical Properties of Soluble N-Doped Rubicenes via Ruthenium-Catalyzed Transfer Hydrogenative Benzannulation. *Chem. - A Eur. J.* **2021**, *27* (15), 4898–4902. https://doi.org/10.1002/chem.202100134.

(290) Sato, H.; Blemker, M. A.; Hellinghausen, G.; Armstrong, D. W.; Nafie, J. W.; Roberts, S. T.; Krische, M. J. Triple Helical Ir(Ppy)3 Phenylene Cage Prepared by Diol-Mediated Benzannulation: Synthesis, Resolution, Absolute Stereochemistry and Photophysical Properties. *Chem. - A Eur. J.* **2019**, *25* (37), 8719–8724. https://doi.org/10.1002/chem.201902122.

(291) Wu, J.; Baumgarten, M.; Debije, M. G.; Warman, J. M.; Müllen, K. Arylamine-Substituted Hexa-Peri-Hexabenzocoronenes: Facile Synthesis and Their Potential Applications as"Coaxial" Hole-Transport Materials. *Angew. Chemie* **2004**, *116* (40), 5445–5449. https://doi.org/10.1002/ange.200460174.

(292) H. Lipshutz, B.; S. Wilhelm, R.; M. Floyd, D. Chemistry of Higher Order, Mixed Organocuprates. 1. Substitution Reactions at Unactivated Secondary Centers. *J. Am. Chem. Soc.* **2002**, *103* (25), 7672–7674. https://doi.org/10.1021/ja00415a055.

(293) Humayun Kabir, S. M.; Iyoda, M. Selectivity of Cyano-Gilman Cuprates: Synthesis of 10-Membered Ring Cyclophanes. *Chem. Commun.* **2000**, No. 23, 2329–2330. https://doi.org/10.1039/b008102g.

(294) Miyake, Y.; Wu, M.; Rahman, M. J.; Iyoda, M. Novel Electron-Transfer Oxidation of Lipshutz Cuprates with 1,4-Benzoquinones: An Efficient Homo-Coupling Reaction of Aryl Halides and Its Application to the Construction of Macrocyclic Systems. *Chem. Commun.* **2005**, No. 3, 411–413. https://doi.org/10.1039/b413842b.

(295) Iyoda, M.; Rahman, M. J.; Matsumoto, A.; Wu, M.; Kuwatani, Y.; Nakao, K.; Miyake, Y. Synthesis of Nonaphenylenes and Dodecaphenylenes Using Electron-Transfer Oxidation of Lipshutz Cuprate Intermediates. *Chem. Lett.* **2005**, *34* (11), 1474–1475. https://doi.org/10.1246/cl.2005.1474.

(296) Rahman, M. J.; Yamakawa, J.; Matsumoto, A.; Enozawa, H.; Nishinaga, T.; Kamada, K.; Iyoda, M. Synthesis of Nonaphenylenes and Dodecaphenylenes Using Electron-Transfer Oxidation of Lipshutz Cuprates and Formation of Nanostructural Materials from Hexadodecyloxynonaphenylene. *J. Org. Chem.* **2008**, *73* (14), 5542–5548. https://doi.org/10.1021/jo800787u.

(297) S. Chao, C.; H. Cheng, C.; T. Chang, C. New Method for the Preparation of Activated Nickel and Cobalt Powders and Their Application in Biaryl Synthesis. *J. Org. Chem.* **2002**, *48* (25), 4904–4907. https://doi.org/10.1021/jo00173a024.

(298) Segawa, Y.; Miyamoto, S.; Omachi, H.; Matsuura, S.; Šenel, P.; Sasamori, T.; Tokitoh, N.; Itami, K. Concise Synthesis and Crystal Structure of [12]Cycloparaphenylene. *Angew. Chemie - Int. Ed.* **2011**, *50* (14), 3244–3248. https://doi.org/10.1002/anie.201007232.

(299) Segawa, Y.; Šenel, P.; Matsuura, S.; Omachi, H.; Itami, K. [9]Cycloparaphenylene: Nickel-Mediated Synthesis and Crystal Structure. *Chem. Lett.* **2011**, *40* (4), 423–425. https://doi.org/10.1246/cl.2011.423.

(300) Janietz, D.; Bauer, M. A New Facile Synthesis of 2-Substituted 4,6-Diphenyl-1,3,5-Triazines. *Synthesis (Stuttg).* **1993**, 33–34.

(301) Xiao, J.; Liu, X. K.; Wang, X. X.; Zheng, C. J.; Li, F. Tailoring Electronic Structure of Organic Host for High-Performance Phosphorescent Organic Light-Emitting Diodes. *Org. Electron.* **2014**, *15* (11), 2763–2768. https://doi.org/10.1016/j.orgel.2014.08.006.

(302) Kasha, M.; Rawls, H. R.; El-Bayoumi, M. A. The Exciton Model In Molecular Spectroscopy. *Pure Appl. Chem.* **1965**, *11* (3–4), 371–392. https://doi.org/10.1351/pac196511030371.

(303) C. Spano, F. The Spectral Signatures of Frenkel Polarons in H- and J-Aggregates. *Acc. Chem. Res.* **2009**, *43* (3), 429–439. https://doi.org/10.1021/ar900233v.

(304) Scholes, G. D. Long-Range Resonance Energy Transfer in Molecular Systems. *Annu. Rev. Phys. Chem.* **2003**, *54* (18), 57–87. https://doi.org/10.1146/annurev.physchem.54.011002.103746.

(305) Beljonne, D.; Curutchet, C.; D. Scholes, G.; J. Silbey, R. Beyond Förster Resonance Energy Transfer in Biological and Nanoscale Systems. *J. Phys. Chem. B* **2009**, *113* (19), 6583–6599. https://doi.org/10.1021/jp900708f.

(306) Clark, J.; Silva, C.; Friend, R. H.; Spano, F. C. Role of Intermolecular Coupling in the Photophysics of Disordered Organic Semiconductors: Aggregate Emission in Regioregular Polythiophene. *Phys. Rev. Lett.* **2007**, *98* (20), 1–4. https://doi.org/10.1103/PhysRevLett.98.206406.

(307) Manas, E. S.; Spano, F. C. Absorption and Spontaneous Emission in Aggregates of Conjugated Polymers. *J. Chem. Phys.* **1998**, *109* (18), 8087–8101. https://doi.org/10.1063/1.477457.

(308) Muccini, M.; Schneider, M.; Taliani, C.; Sokolowski, M.; Umbach, E.; Beljonne, D.; Cornil, J.; Brédas, J. L. Effect of Wave-Function Delocalization on the Exciton Splitting in Organic Conjugated Materials. *Phys. Rev. B - Condens. Matter Mater. Phys.* **2000**, *62* (10), 6296–6300. https://doi.org/10.1103/PhysRevB.62.6296.

(309) Sun, H.; Zhao, Z.; Spano, F. C.; Beljonne, D.; Cornil, J.; Shuai, Z.; Brédas, J. L. Absorption and Emission in Quaterthienyl Thin Films. *Adv. Mater.* **2003**, *15* (10), 818–822. https://doi.org/10.1002/adma.200304770.

(310) Tavazzi, S.; Campione, M.; Laicini, M.; Raimondo, L.; Borghesi, A.; Spearman, P. Measured Davydov Splitting in Oligothiophene Crystals. *J. Chem. Phys.* **2006**, *124* (194710), 1–7. https://doi.org/10.1063/1.2196037.

(311) Hiraki, T.; Nakahara, K.; Narumi, K.; Niiyama, R.; Kida, N.; Takamura, N.; Okamoto, H.; Kawahara, Y. Laser Pouch Motors: Selective and Wireless Activation of Soft Actuators by Laser-Powered Liquid-to-Gas Phase Change. *IEEE Robot. Autom. Lett.* **2020**, *5* (3), 4180–4187. https://doi.org/10.1109/LRA.2020.2982864.

(312) Narumi, K.; Sato, H.; Nakahara, K.; Seong, Y. A.; Morinaga, K.; Kakehi, Y.; Niiyama, R.; Kawahara, Y. Liquid Pouch Motors: Printable Planar Actuators Driven by Liquid-to-Gas Phase Change for Shape-Changing Interfaces. *IEEE Robot. Autom. Lett.* **2020**, *5* (3), 3915–3922. https://doi.org/10.1109/LRA.2020.2983681.

(313) Lin, G.; Huang, W.; Hu, C.; Xiao, J. Design and Control Strategy of Soft Robot Based on Gas – Liquid Phase Transition Actuator. *Mathematics* **2022**, *10* (2847), 1–20. https://doi.org/10.3390/math10162847.

(314) El-atab, N.; Mishra, R. B.; Al-modaf, F.; Joharji, L.; Alsharif, A. A.; Alamoudi, H.; Diaz, M.; Qaiser, N.; Hussain, M. M. Soft Actuators for Soft Robotic

Applications : A Review. *Adv. Intell. Syst.* **2020**, *2* (10), 2000128-1-2000128–2000137. https://doi.org/10.1002/aisy.202000128.

(315) Chellattoan, R.; Yudhanto, A.; Lubineau, G. Low-Voltage-Driven Large-Amplitude Soft Actuators. *Soft Robot.* **2020**, *7* (6), 688–699. https://doi.org/10.1089/soro.2019.0150.

(316) Usui, T.; Ishizuka, H.; Hiraki, T.; Kawahara, Y.; Ikeda, S.; Oshiro, O. Fully Flexible Liquid-to-Gas Phase Change Actuators with Integrated Liquid Metal Heaters. *Jpn. J. Appl. Phys.* **2021**, *60* (SCCL11-1), 1–10. https://doi.org/10.35848/1347-4065/abec8d.

(317) Kellaris, N.; Venkata, V. G.; Smith, G. M.; Mitchell, S. K.; Keplinger, C. Peano-HASEL Actuators : Muscle-Mimetic , Electrohydraulic Transducers That Linearly Contract on Activation. *Sci. Robot.* **2018**, *3* (14), 1–10. https://doi.org/10.1126/scirobotics.aar3276.

(318) Mirvakili, S. M.; Sim, D.; Hunter, I. W.; Langer, R. Actuation of Untethered Pneumatic Artificial Muscles and Soft Robots Using Magnetically Induced Liquid-to-Gas Phase Transitions. *Sci. Robot.* **2020**, *5* (42), 1–9. https://doi.org/10.1126/scirobotics.aaz4239.

(319) Lui, B. F.; Bardeen, C. J. Using Small Molecule Absorbers to Create a Photothermal Wax Motor. *Small* **2022**, *18* (2105356), 1–7. https://doi.org/10.1002/smll.202105356.

(320) Miriyev, A.; Stack, K.; Lipson, H. Soft Material for Soft Actuators. *Nat. Commun.* **2017**, *8* (1), 1–8. https://doi.org/10.1038/s41467-017-00685-3.

(321) Huber, J. E.; Fleck, N. A.; Ashby, M. F. The Selection of Mechanical Actuators Based on Performance Indices. *Proc. R. Soc. London. Ser. A Math. Phys. Eng. Sci.* **1997**, *453*, 2185–2205. https://doi.org/10.1098/rspa.1997.0117.

(322) Jiang, L.; Yang, Y.; Chen, R.; Lu, G.; Li, R.; Li, D.; Humayun, M. S.; Shung, K. K.; Zhu, J.; Chen, Y.; Zhou, Q. Flexible Piezoelectric Ultrasonic Energy Harvester Array for Bio-Implantable Wireless Generator. *Nano Energy* **2019**, *56*, 216–224. https://doi.org/10.1016/j.nanoen.2018.11.052.

(323) Fishburn, J. M.; Mildren, R. P.; Kapitan, D.; Withford, M. J.; Brown, D. J. W.; Piper, J. A. Exploring the Explosive Ablation Regime of Metals in Nanosecond Micromachining. *High-Power Laser Ablation II* **2000**, *3885*, 453–460. https://doi.org/10.1117/12.376996.

(324) Kalus, M. R.; Barcikowski, S.; Gökce, B. How the Physicochemical Properties of the Bulk Material Affect the Ablation Crater Profile, Mass Balance, and Bubble Dynamics During Single-Pulse, Nanosecond Laser Ablation in Water. *Chem. - A Eur. J.* **2021**, *27* (19), 5978–5991. https://doi.org/10.1002/chem.202005087.

(325) Abdellatif, G.; Imam, H. A Study of the Laser Plasma Parameters at Different Laser Wavelengths. *Spectrochim. Acta-Part B At. Spectrosc.* **2002**, *57* (7), 1155–1165. https://doi.org/10.1016/S0584-8547(02)00057-5.

(326) Bogaerts, A.; Chen, Z. Effect of Laser Parameters on Laser Ablation and Laser-Induced Plasma Formation: A Numerical Modeling Investigation. *Spectrochim. Acta - Part B At. Spectrosc.* **2005**, *60*, 1280–1307. https://doi.org/10.1016/j.sab.2005.06.009.

(327) Tan, M. I. S. M. H.; Omar, A. F.; Rashid, M.; Hashim, U. VIS-NIR Spectral and Particles Distribution of Au, Ag, Cu, Al and Ni Nanoparticles Synthesized in Distilled Water Using Laser Ablation. *Results Phys.* **2019**, *14* (102497), 1–12. https://doi.org/10.1016/j.rinp.2019.102497.

(328) Singh, R.; Soni, R. K. Laser Synthesis of Aluminium Nanoparticles in Biocompatible Polymer Solutions. *Appl. Phys. A Mater. Sci. Process.* **2014**, *116* (2), 689–701. https://doi.org/10.1007/s00339-014-8487-z.

(329) González, B.; Calvar, N.; Gómez, E.; Domínguez, Á. Density, Dynamic Viscosity, and Derived Properties of Binary Mixtures of Methanol or Ethanol with Water, Ethyl Acetate, and Methyl Acetate at T = (293.15, 298.15, and 303.15) K. *J. Chem. Thermodyn.* **2007**, *39* (12), 1578–1588. https://doi.org/10.1016/j.jct.2007.05.004.

(330) Aldrich, E. W.; Querfeld, D. W. Freezing and Boiling Points of the Ternary System Ethanol-Methanol-Water. *Ind. Eng. Chem.* **1931**, *23* (6), 708–711. https://doi.org/10.1021/ie50258a029.

(331) Benson, G. C.; D'Arcy, P. J. Excess Isobaric Heat Capacities of Water-n-Alcohol Mixtures. *J. Chem. Eng. Data* **1982**, *27* (4), 439–442. https://doi.org/10.1021/je00030a021.

(332) Korson, L.; Drost-Hansen, W.; Millero, F. J. Viscosity of Water at Various Temperatures. *J. Phys. Chem.* **1969**, *73* (1), 34–39. https://doi.org/10.1021/j100721a006.

(333) NIST Chemistry WebBook. *Aver. Rep. Value Individ. Data Points SRD 69*.

(334) Chase, M. W. J. NIST-JANAF Themochemical Tables. *J. Phys. Chem. Ref. Data*, **1998**, *Monograph* (4), 1–1951.

(335) Lee, R.; Teja, A. S. Viscosities of Poly (Ethylene Glycols). *J. Chem. Eng. Data* **1990**, *35*, 385–387. https://doi.org/10.1021/je00062a003.

(336) Zaripov, Z. I. Experimental Study of the Isobaric Heat Capacity of Liquid Organic Compounds with Molecular Weights of up to 4000 a.e.M. *Tepl. Teplofiz* **1982**.

(337) Sheely, M. L. Glycerol Viscosity Tables. *Ind. Eng. Chem.* **1932**, *24* (9), 1060–1064. https://doi.org/10.1021/ie50273a022.

(338) Bastos, M.; Nilsson, S.-O.; Ribeiro Da Silva, M. D. M. C.; Ribeiro Da Silva, M. A. V.; Wadso, I. Thermodynamic Properties of Glycerol Enthalpies of Combustion and Vaporization and the Heat Capacity at 298.15 K. Enthalpies of Solution in Water at 288.15, 298.15, and 308.15 K. *J. Chem. Thermodyn.* **1988**, *20*, 1353–1359.

(339) Ravenni, G.; Sárossy, Z.; Ahrenfeldt, J.; Henriksen, U. B. Activity of Chars and Activated Carbons for Removal and Decomposition of Tar Model Compounds – A Review. *Renew. Sustain. Energy Rev.* **2018**, *94* (July), 1044–1056. https://doi.org/10.1016/j.rser.2018.07.001.

(340) Safarik, I.; Strausz, O. P. The Thermal Decomposition of Hydrocarbons. Part 1. n-Alkanes ($C \geq 5$). *Res. Chem. Intermed.* **1996**, *22* (3), 275–314. https://doi.org/10.1163/156856796X00458.

(341) Zerr, A.; Serghiou, G.; Boehler, R.; Ross, M. Decomposition of Alkanes at High Pressures and Temperatures. *High Press. Res.* **2006**, *26* (1), 23–32. https://doi.org/10.1080/08957950600608931.

(342) Rumble, J. R. *CRC Handbook of Chemistry and Physics*, 103rd ed.; Rumble, J. R., Ed.; 2022.

(343) Grigor'ev, B. A.; Rastorguev, Y. L.; Yanin, G. S. Experimental Determination of the Isobaric Specific Heat of N-Alkanes. *Iz. Vyss. Uchebn. Zaved. Neft Gaz* **1975**, *10*, 63–66.

(344) Andreoli-Ball, L.; Patterson, D.; Costas, M.; Cáceres-Alonso, M. Heat Capacity and Corresponding States in Alkan-1-Ol-n-Alkane Systems. *J. Chem. Soc. Faraday Trans. 1 Phys. Chem. Condens. Phases* **1988**, *84* (11), 3991–4012. https://doi.org/10.1039/F19888403991.

(345) Trejo, L. M.; Costas, M.; Patterson, D. Excess Heat Capacity of Organic Mixtures. *Internat. DATA Ser.* **1991**, *Selected D*.

(346) Tardajos, G.; Aicart, E.; Costas, M.; Patterson, D. Liquid Structure and Second-Order Mixing Functions for Benzene, Toluene and p-Xylene with n-Alkanes. *J. Chem. Soc. Faraday Trans. 1 Phys. Chem. Condens. Phases* **1986**, *82* (9), 2977–2987. https://doi.org/10.1039/F19868202977.

(347) DeVoe, H. *Thermodynamics and Chemistry*; Prentice Hall: Upper Saddle River, NJ, 2001.